④

AD-A196 568

AFGL-TR-88-0095

ATTENUATION AND DETECTION CAPABILITY
OF REGIONAL PHASES RECORDED AT NORESS

Thomas J. Sereno, Jr.
Steven R. Bratt

Science Applications International Corp.
10260 Campus Point Drive
San Diego, CA 92121

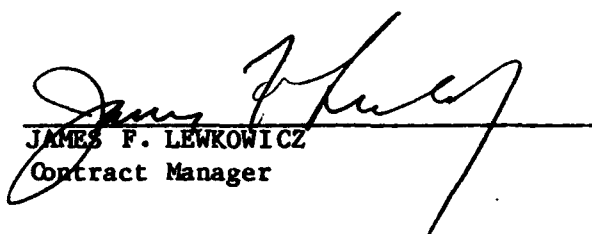25 March 1988

Semiannual Report No. 3

Approved for public release; distribution unlimited

AIR FORCE GEOPHYSICS LABORATORY
AIR FORCE SYSTEMS COMMAND
UNITED STATES AIR FORCE
HANSCOM AIR FORCE BASE, MASSACHUSETTS 01731

88

"This technical report has been reviewed and is approved for publication."

JAMES F. LEWKOWICZ
Contract Manager

HENRY A. OSSING
Chief, Solid Earth Geophysics Branch

FOR THE COMMANDER

DONALD H. ECKHARDT
Director
Earth Sciences Division

REPORT DOCUMENTATION PAGE

1a. REPORT SECURITY CLASSIFICATION	1b. RESTRICTIVE MARKINGS
Unclassified	

2a. SECURITY CLASSIFICATION AUTHORITY	3. DISTRIBUTION / AVAILABILITY OF REPORT
2b. DECLASSIFICATION / DOWNGRADING SCHEDULE	Approved for public release; distribution unlimited

4. PERFORMING ORGANIZATION REPORT NUMBER(S)	5. MONITORING ORGANIZATION REPORT NUMBER(S)
SAIC-88/1598	AFGL-TR-88-0095

6a. NAME OF PERFORMING ORGANIZATION	6b. OFFICE SYMBOL (If applicable)	7a. NAME OF MONITORING ORGANIZATION
Science Applications International Corporation		Air Force Geophysics Laboratory (LWH)

6c. ADDRESS (City, State, and ZIP Code)	7b. ADDRESS (City, State, and ZIP Code)
10260 Campus Point Drive San Diego, CA 92121	Hanscom Air Force Base, MA 01731

8a. NAME OF FUNDING / SPONSORING ORGANIZATION	8b. OFFICE SYMBOL (If applicable)	9. PROCUREMENT INSTRUMENT IDENTIFICATION NUMBER
DARPA	GSD	F19628-86-C-0051

8c. ADDRESS (City, State, and ZIP Code)	10. SOURCE OF FUNDING NUMBERS			
	PROGRAM ELEMENT NO.	PROJECT NO.	TASK NO.	WORK UNIT ACCESSION NO.
1400 Wilson Blvd. Arlington, VA 22209	62714E	6A10	DA	BB

11. TITLE (Include Security Classification)

Attenuation and Detection Capability of Regional Phases Recorded at NORESS

12. PERSONAL AUTHOR(S)

Thomas J. Sereno, Jr. and Steven R. Bratt

13a. TYPE OF REPORT	13b. TIME COVERED	14. DATE OF REPORT (Year, Month, Day)	15. PAGE COUNT
Semi-Annual #3	FROM 3/1/87 TO 8/31/87	March 25, 1988	150

16. SUPPLEMENTARY NOTATION

17. COSATI CODES			18. SUBJECT TERMS (Continue on reverse if necessary and identify by block number)
FIELD	GROUP	SUB-GROUP	Regional Seismology, Generalized Inversion, Attenuation, Seismic Moment, NORESS Array, Detection Capability.

19. ABSTRACT (Continue on reverse if necessary and identify by block number)

The attenuation and detectability of regional Pn and Lg phases recorded at the NORESS array in Norway are estimated. We determine the frequency-dependent attenuation by inverting Pn and Lg single-channel spectra recorded at NORESS from 186 events at ranges between 200-1400 km with magnitudes between 1.1 and 4.8. The Pn spectra are inverted between 1-15 Hz and the Lg spectra between 1-7 Hz for both seismic moment and apparent attenuation. To resolve parameter trade-offs, we require that the separate Pn and Lg attenuation models produce an internally consistent set of source parameters. We find that regional Pn spectra are accurately described by $r^{-1.3}$ geometric spreading and $Q(f) = 325f^{0.48}$. Lg spectra computed for a group velocity window of 3.6-3.0 km/s are consistent with cylindrical spreading and $Q(f) = 560f^{0.26}$. We determine the sensitivity of our estimates to the window length used in

20. DISTRIBUTION / AVAILABILITY OF ABSTRACT	21. ABSTRACT SECURITY CLASSIFICATION
☐ UNCLASSIFIED/UNLIMITED ☒ SAME AS RPT. ☐ DTIC USERS	Unclassified

22a. NAME OF RESPONSIBLE INDIVIDUAL	22b. TELEPHONE (Include Area Code)	22c. OFFICE SYMBOL
James F. Lewkowicz	(617) 377-3028	AFGL/LWH

DD FORM 1473, 84 MAR 83 APR edition may be used until exhausted. SECURITY CLASSIFICATION OF THIS PAGE
All other editions are obsolete. Unclassified

Fourier analysis, geometric spreading and source assumptions, and the inversion bandwidth. The final result is a simple parameterization of the source and range dependence of regional Pn and Lg spectra. However, since signal detection is based on time domain amplitudes measured on filtered beams, a parameterization of single-channel spectra is not sufficient to determine detection capability. Therefore, we determine a relationship between the spectral amplitudes used in the inversion and the time domain amplitudes used in signal detection. There are two separate issues that are central in developing this relationship. One is the relation between temporal and spectral amplitudes on filtered beams and the other is the relation between beam spectra and single-channel spectra. The first of these depends on the dispersion while the second is essentially the beam gain. We find that the temporal signal-to-noise ratio (SNR) for Pn measured on a filtered beam can be expressed as a product of the single-channel spectral SNR and terms specific to the NORESS array configuration and beamforming. This factorization allows us to predict the Pn detection capability for other regions of estimated attenuation or for other station configurations. However, the relationship is more complicated for Lg because it is a dispersed phase and because the pre-Lg noise is a complicated function of magnitude, distance, and frequency. Therefore for Lg we simply determine an empirical relationship for the time domain amplitudes in terms of the spectral amplitudes used in the inversion and acknowledge that our Lg detection capability cannot be extrapolated with confidence to other areas or to ranges greater about 1400 km. To demonstrate the validity of our parameterization, we compare the predicted detection capability based on our inversion results to the observed temporal SNRs and find that they are generally consistent. We estimate the 90% NORESS M_L detection thresholds for Pn to be 2.0 at 400 km and 2.8 at 1000 km. For Lg the 90% thresholds are 2.0 at 400 km and 3.3 at 1000 km. The 90% thresholds for detection of either Pn or Lg are 1.7 at 400 km and 2.6 at 1000 km. These results are also consistent with NORESS magnitude detection thresholds determined by *Ringdal* (1986), and this provides independent support for our parameterization.

Table of Contents

1. INTRODUCTION

We estimate the attenuation and detectability of regional *Pn* and *Lg* phases recorded by the NORESS array in Norway. This is a continuation of the work described in our previous semi-annual report [*Sereno et al.*, 1987]. There we presented attenuation estimates based on the inversion of spectra from 190 regional events. In this study we extend these results by (1) examining the sensitivity of the attenuation estimates to our signal processing procedures, (2) bounding the bias in the *Lg* attenuation estimates caused by contamination by *Sn* coda, (3) investigating the relationship between the spectral amplitudes used in the inversion and the time-domain amplitudes used in signal detection.

1.1 Objectives

The primary objective of this research is to accurately determine frequency-dependent attenuation curves for regional phases recorded at NORESS. A successful parameterization of regional wave spectra in terms of event magnitude and epicentral distance has important implications for many practical issues in nuclear explosion seismology such as event detection and and identification capabilities. However, because signal detection is based on time-domain amplitudes measured on filtered beams, a spectral parameterization is insufficient to determine detection capability. Therefore, in this report we focus on the connection between the temporal amplitudes used in signal detection and the array-averaged spectral amplitudes used in our inversion. In particular, we examine the following:

- *Spectral amplitudes and signal processing.* Spectral amplitudes are a function of the time window selected for Fourier analysis, particularly for dispersed phases. Therefore, it is necessary to determine the sensitivity of our attenuation estimates to our signal processing procedures. The selection of an "appropriate" time window depends upon the specific application of the attenuation results. For example, a time window long enough to include the contribution of dispersed modes is required to estimate the average anelasticity of the crust from *Lg* spectra. However, signal detection is not based on the energy distribution over a long time window, but is more accurately represented by a parameterization of spectra computed over a short window length. We previously presented results that accurately describe the important characteristics of *Pn* and *Lg* spectra computed for fixed 5-s windows [*Sereno et al.*, 1987]. In this report we compare attenuation estimates obtained from *Lg* spectra computed in three ways, for fixed time lengths of 5 s and 17 s and for a fixed group velocity window from 3.0 to 3.6 km/s.

1

- *Bias from interfering phases.* Secondary phase detection capability depends not only on signal amplitudes, but also on the amplitude and spectral content of the coda of previously arriving phases. Because Sn is a higher-frequency phase than Lg, its coda could introduce an upward bias in the $Lg\ Q$ estimate. To check this, we invert the Lg spectra over several frequency bands and compare the Sn coda spectra to the Lg spectra over a broad distance range to bound the bias in Q_{Lg}.

- *Spectral and temporal amplitudes.* The STA/LTA detector is used for processing NORESS data. That is, signal detection is achieved when the short term average (STA) divided by the long term average (LTA) exceeds a prescribed threshold. These amplitudes are measured on filtered beams. The spectra used in the inversion are array-averages of single-channel spectra. Therefore, the relationship between temporal amplitudes used in detection and the spectral amplitudes used in our inversion depends on the beam gain, filter bandwidth, and the relation between single-channel time and frequency domain amplitudes. Each of these must be considered if detection capability is to be estimated from attenuation models obtained through spectral analysis.

1.2 Outline of the report

This report in divided into five sections, including this introduction. Section 2 describes the results of the inversion of Pn and Lg spectra and their dependence on the time window selected for Fourier analysis. In particular we compare Lg attenuation estimates based on fixed time length (FTL) and fixed group velocity (FGV) windowing. The main results are in Section 2.9 where we compare results for fixed 5-s and 17-s windows and for a fixed group velocity window of 3.6-3.0 km/s. The results for FGV windowing were summarized by *Sereno et al.* [1988]. We present the complete results of that study in Section 2 and Appendix A. Section 2.10 compares predicted spectra based on the results of our inversion to those based on the attenuation curves used by *Evernden et al.* [1986] to estimate detection capability in the Soviet Union. We find that the *Evernden at al.* curves vastly overestimate the detectability of high-frequency waves seen in NORESS recordings of events in northern Europe.

Section 3 examines the influence of Sn coda on the $Lg\ Q$ estimate. We superimpose pre-Lg and Lg spectra to determine the approximate frequency band for which Lg can be considered free of Sn coda contamination. We find that Sn coda contaminates the Lg spectra at frequencies greater than about 12 Hz at distances near 300 km and at frequencies greater than about 4 Hz at distances near 1000 km. *Sereno et al.* [1988] inverted Lg spectra over a 1-7 Hz band for data spanning a distance range of 200-1400 km. Therefore, it is quite possible that their results (described in Section 2) are affected by Sn coda. In Section 3 we invert the Lg spectra over 1-3 and 1-5 Hz bands and compare to our 1-7 Hz results to bound the Sn coda bias in Q_{Lg}.

The relationship between time and frequency domain amplitudes is explored in Section 4. Detection statistics are compiled from the output of an automated detection and post-processing program, SAIAP, which is an extension of the RONAPP program used at NORSAR

2

[*Mykkeltveit and Bungum*, 1984]. In general, predictions based on the spectral inversion results are consistent with the observed detection statistics. Array-averaged spectral levels are compared to the LTAs and STAs measured on the detecting beams. In Section 4.6 we parameterize the detectability of *Pn* and *Lg* phases using only time domain measurements and compare the results to our spectral analysis. Section 5 presents our main conclusions and summarizes the results of this study.

2. REGIONAL WAVE SPECTRA, Q AND WINDOW LENGTH

In this section we estimate the frequency-dependent attenuation of *Pn* and *Lg* phases from 186 regional events recorded by the NORESS array in Norway. The important differences between the results presented in this section and our previous results [*Sereno et al.*, 1987; *Sereno et al.*, 1988] are summarized below:

- *Sereno et al.* [1987] estimate attenuation and seismic moment from *Pn* and *Lg* spectra computed for fixed 5-s windows. Data from 190 regional events were used in the analysis. Here we determine the sensitivity of those estimates to the time window used in the calculation of the spectra. Four of the events used by *Sereno et al.* [1987] were excluded from this analysis because the FGV window included spurious detections. We find that the *Lg* inversion results are strongly dependent upon the window length, while the results for *Pn* are not. Because *Lg* is dispersed, attenuation and moment estimated from spectra computed for fixed time windows can be biased by the exclusion of the lower group velocity modes at long ranges. Therefore, Q estimated from spectra computed in this way cannot be interpreted in terms of crustal rheology unless the fixed time length is sufficient to include the entire dispersed wave train at all ranges. Thus, we estimate the Q for *Lg* using spectra computed with a fixed group velocity window, 3.6-3.0 km/s. The resulting Q_{Lg} can be interpreted as a measure of the average anelastic absorption of shear waves in the crust [*Campillo et al.*, 1985]. Although the *Pn* windowing procedure remains unchanged, the results presented here for *Pn* differ slightly from those presented in our previous report [*Sereno et al.*, 1987]. This is because our method uses the consistency of the derived source parameters from the separate *Pn* and *Lg* inversion to resolve parameter trade-offs. Since the *Lg* model is different for the FGV spectra, a different *Pn* model produces an internally consistent set of source parameters.

- *Sereno et al.* [1988] summarize attenuation and seismic moment results for *Pn* computed for fixed 5-s windows and *Lg* spectra computed for the fixed group velocity range 3.0 to 3.6 km/s. This section and Appendix A present the complete results of that study. We also compare these Q_{Lg} estimates with estimates for fixed time lengths of 5 s and 17 s. The 17-s window was chosen since it has been used in other studies of *Lg* attenuation.

For a given set of source and spreading assumptions, the inversion clearly defines a broad minimum in the data residuals corresponding to a suite of models that fit the data equally well in a least squares sense. In Sections 2.4-2.7 the results for our "preferred model" are presented. In Section 2.8 we discuss the trade-offs among model parameters, the dependence of the results on our source and spreading assumptions, and the basis for selecting our "preferred model." Throughout this section we present only representati· comparisons of theoreti-

cal and observed spectra. A complete catalog of the estimated source parameters and plots comparing theoretical and observed spectra is given in Appendix A.

2.1 Method

This section is a brief summary of the method we used to estimate attenuation and source parameters. A detailed description of our method is given by *Sereno et al.* [1987]. The analysis assumes a simple source scaling model and that all observed spectra can be fit by a single frequency-dependent Q model. We parameterize the instrument-corrected amplitude spectrum of a seismic signal as

$$A(f,r) = S(f) \, G(r,r_0) \, \exp\left[\frac{-\pi f t}{Q(f)}\right] \qquad (2.1)$$

where $A(f,r)$ is the observed displacement spectrum at range r and frequency f, $S(f)$ is the source spectrum, $G(r,r_0)$ is geometric spreading, and the last term is the effective attenuation for travel time t. Note that the effective attenuation includes contributions from both anelasticity and scattering.

Source spectra. We adopt a simplified *Mueller and Murphy* [1971] explosion source function characterized by f^{-2} decay beyond a corner frequency that scales inversely with the cube root of the long-period level. That is,

$$f_c = c S_0^{-1/3} \qquad (2.2)$$

where S_0 is the long-period source level, f_c is the corner frequency, and c is a scaling constant.

The source parameters estimated by the inversion are S_0 for each event and a single value of c relating corner frequency to long-period source level. The explosion moments are estimated from the long-period levels derived from Pn [*Stevens and Day*, 1985]. Since our observations are from a single station and the focal mechanisms for the small earthquakes in our data set are unknown, we do not know the radiation pattern and are therefore unable to estimate seismic moment from $S_0^{eq}(Pn)$. However, since Lg samples a large fraction of the focal sphere, the earthquake moments can be estimated from the long-period source levels derived from Lg [*Street et al.*, 1975]. The relationships we use to estimate seismic moment are

$$M_0^{exp} = 4\pi \rho_s \alpha_s^3 S_0^{exp}(Pn) \qquad (2.3)$$

$$M_0^{eq} = 4\pi \rho_c \beta_c^3 S_0^{eq}(Lg) \qquad (2.4)$$

where ρ_s and α_s are near-surface density and compressional velocity, and ρ_c and β_c are the average crustal density and shear wave velocity.

The amount of Lg energy excited by an explosion is depth-dependent and complicated by near-source wave conversions [*Bennett et al.*, 1987]. Explosions generate Lg energy primarily through P–SV mode conversions and scattering, while earthquakes produce much more direct shear wave energy. Therefore, for a given source moment and focal depth, earthquakes are

5

expected to generate larger Lg amplitudes than explosions. We will express the long-period Lg source level for an explosion as an unknown fraction of the long-period level for an earthquake of equal moment and depth. That is,

$$S_0^{exp}(Lg) = \kappa \, S_0^{eq}(Lg) \qquad (2.5)$$

where κ is an unknown constant, presumably less than one. We will estimate this constant using (2.3), (2.4), and (2.5), together with the observed ratio of $S_0^{exp}(Lg)$ to $S_0^{exp}(Pn)$.

Geometric spreading. The inversion also requires that we assume the geometric spreading function. Following *Herrmann and Kijko* [1983], we express the spreading function in the frequency domain as

$$
\begin{aligned}
G(r,r_0) &= (1/r) & \text{for } r \leq r_0 \\
G(r,r_0) &= r_0^{-1} \, (r_0/r)^m & \text{for } r \geq r_0
\end{aligned}
\qquad (2.6)
$$

where r_0 is a transition distance from spherical spreading to spreading rate m. The Lg phase consists of higher-mode surface waves which are accurately described at long ranges by cylindrical spreading ($m = 1/2$), provided the window length is sufficient to encompass the entire dispersed wave train. By comparing the long-period amplitude spectrum of Lg to moments calculated from long-period surface waves, *Street et al.* [1975] empirically determined $r_0 \approx 100$ km, or roughly twice the crustal thickness. Measuring the decay rate of synthetic Lg phases computed for an elastic medium, *Herrmann and Kijko* [1983] verified that Lg frequency domain spreading was accurately described as cylindrical and substantiated the empirical result of *Street et al.* [1975] for r_0. Therefore we adopt (2.6) with $r_0 = 100$ km and $m = 1/2$ to approximate Lg geometric spreading.

Less work has been done on the spreading rate of Pn. Because its energy density is more localized about a single ray path, Pn geometric spreading is more sensitive to velocity gradients in the upper mantle. Numerical studies of Pn indicate that for typical upper mantle structures the spreading rate lies between r^{-1} and r^{-2} [*Langston*, 1982; T. C. Wallace, personal communication, 1987]. That is, the spreading rate lies between that for the "simple turning ray" and the "canonical head wave" interpretations of the Pn ray path. We find that an important constraint on Pn spreading is the consistency of the derived source parameters from the separate Lg and Pn inversions. As discussed in Section 2.8, this criterion supports a choice of $r^{-1.3}$ for the Pn spreading rate. Therefore we use (2.6) with $r_0 = 1$ km and $m = 1.3$ to describe Pn spreading. In Section 2.8 we discuss how the results change when different spreading is assumed.

Effective attenuation. We characterize the range-dependent decay of the seismic spectrum in terms of a power law frequency dependence of Q. That is,

$$Q(f) = Q_0 f^{\eta} \qquad (2.7)$$

where Q_0 and η are parameters of the inversion. No attempt is made to distinguish intrinsic absorption from scattering. In this form, our results are easily compared to those for other

geographic regions. We have not accounted for any azimuthal variations in Q, but have combined data from all azimuths into an inversion for a single, average Q model. Examination of the fit of the model to the data demonstrates the validity of this procedure.

Inversion. The input data for the inversion are the logarithms of the observed displacement spectra corrected for the assumed geometric spreading. These data are inverted for apparent attenuation, source moment, and the constant relating corner frequency and moment. Adopting standard methods for solving non-linear inverse problems, we linearize the system of equations governing the relationship between the data and model parameters. We assume a starting model, compute theoretical data, subtract it from the observed data, and solve iteratively for the model perturbations that minimize the data residual in the least squares sense. In practice, we have found it necessary to include damping to stablize the solution. That is, we minimize a weighted sum of the data residuals and the model perturbation norm. The explicit problem formulation, matrices, and partial derivatives are given by *Sereno et al* [1987].

2.2 Data

The data used in this study consist of stable, array-averaged spectra for 186 regional events recorded by the small aperture NORESS seismic array in Norway. Event magnitudes range between 1.1 and 4.8 and epicentral distances are between 200 and 1400 km. The NORESS array configuration and sampling rate were designed to enhance the detection of signals from small regional events [*Mykkeltveit et al.*, 1983]. The array includes 25 short-period instruments in concentric rings with a maximum diameter of 3 km. The data are digitally recorded at 40 samples per second.

Table 2.1 is a list of all events and phases (*Pn* and/or *Lg*) used in the inversion. In some cases only one phase was included because the other was not detected or because it had a low signal/noise ratio over the frequency band used in the inversion. Reported mining explosions are identified by an "EX" under the column heading, "Type." The label following "EX" identifies the mine. Three are in southwest Norway; BLA (Blasjo), TIT (Titania), and NYG (Nygardstaugen). Other mine codes are those used in the bulletin published by the University of Helsinki based on the Finish Seismic Array. An "EQ" designator identifies presumed earthquakes, although some may be unreported explosions. Events that are not reported explosions, but have locations within 50 km of known mines are considered of unknown source type.

The location and origin times are from a local bulletin published by the University of Bergen or the University of Helsinki, when available, or from the Preliminary Determination of Epicenters (PDE) bulletin. Events for which an independent network solution is not available are assigned either *RONAPP* (single asterisk) or *SAIAP* (double asterisk) locations. The *RONAPP* locations are published in the NORESS bulletin, along with the detection times of the *P* and *Lg* phases used in the location solutions. In some cases *RONAPP* did not associate phases correctly, and we were able to use the *SAIAP* solution with the appropriate phase association. *SAIAP* also uses a broad band, frequency-wavenumber calculation (*Kvaerna and Ringdal*, 1986) that gives more accurate azimuth estimates than those used in the *RONAPP* locations.

7

Table 2.1. Events used in the generalized inversion.

Event	Date	Time	Location	Type	Phases		M_L	
1	10-25-85	12:04	59.30N 28.10E	EX-E7	*Pn*	*Lg*	3.0	
2	10-27-85	4:36	61.30N 4.30E	EQ	*Pn*	*Lg*	2.8	(B)
3	10-27-85	4:41	66.40N 11.60E*	EQ	*Pn*	*Lg*	2.3	
4	10-27-85	4:52	66.00N 14.10E**	EQ	*Pn*	*Lg*	2.2	
5	10-29-85	10:23	59.31N 6.95E	EX-BLA	*Pn*	*Lg*	1.9	(R)
6	10-31-85	2:56	62.78N 18.03E	EQ	*Pn*	*Lg*	2.8	
7	10-31-85	14:11	60.70N 29.00E	EX-V5	*Pn*	*Lg*	2.8	
8	11- 6-85	14:51	59.31N 6.95E	EX-BLA	*Pn*	*Lg*	2.4	
9	11- 9-85	14:43	58.34N 6.43E	EX-TIT	*Pn*	*Lg*	2.1	
10	11- 9-85	18:21	62.60N 6.70E**	--	*Pn*	*Lg*	2.0	(R)
11	11-12-85	12:22	59.50N 25.00E	EX-E3		*Lg*	2.6	
12	11-13-85	12:08	59.30N 28.10E	EX-E7	*Pn*	*Lg*	2.7	
13	11-13-85	14:11	58.34N 6.43E	EX-TIT	*Pn*	*Lg*	1.9	
14	11-14-85	12:52	60.70N 28.70E	EX-V12	*Pn*	*Lg*	2.9	
15	11-15-85	13:54	61.10N 29.90E	EX-V8	*Pn*		2.9	
16	11-21-85	11:50	59.30N 27.20E	EX-E4		*Lg*	2.4	(H)
17	11-21-85	13:17	59.29N 7.04E	--	*Pn*	*Lg*	1.9	
18	11-23-85	13:06	59.50N 25.00E	EX-E3		*Lg*	2.5	
19	11-25-85	13:06	59.40N 28.50E	EX-E8		*Lg*	3.0	
20	11-27-85	4:54	59.73N 5.71E	EQ	*Pn*	*Lg*	3.0	
21	11-27-85	12:18	61.40N 31.60E	EX-V4	*Pn*		2.8	
22	11-28-85	9:30	57.90N 11.50E**	EQ	*Pn*	*Lg*	2.1	(R)
23	11-30-85	19:05	61.55N 4.65E	EQ	*Pn*	*Lg*	3.0	
24	12- 1-85	7:21	67.70N 33.70E	EX-K1		*Lg*	2.8	
25	12- 5-85	12:25	61.10N 30.20E	EX-V2	*Pn*		<2.0	(H)
26	12- 7-85	13:18	59.30N 27.20E	EX-E4		*Lg*	3.1	
27	12- 7-85	14:16	60.19N 5.25E	--	*Pn*	*Lg*	2.2	
28	12- 7-85	14:39	58.90N 5.98E	EQ	*Pn*	*Lg*	1.9	
29	12-10-85	12:06	59.40N 28.50E	EX-E8		*Lg*	3.2	
30	12-10-85	12:18	60.60N 29.20E	EX-V11	*Pn*	*Lg*	2.0	(R)
31	12-10-85	13:43	59.72N 22.56E	EQ	*Pn*		2.0	
32	12-11-85	12:14	59.40N 28.50E	EX-E8	*Pn*	*Lg*	3.3	
33	12-11-85	12:51	59.30N 27.60E	EX-E6		*Lg*	2.8	
34	12-13-85	12:09	59.40N 28.50E	EX-E8	*Pn*	*Lg*	2.8	
35	12-14-85	14:35	61.10N 30.20E	EX-V2	*Pn*		2.4	(H)
36	12-17-85	13:08	61.10N 30.20E	EX-V2	*Pn*		2.5	(H)
37	12-23-85	4:27	50.18N 12.35E	EQ	*Pn*		3.2	(R)
38	12-24-85	0:04	50.17N 12.44E	EQ	*Pn*		2.6	(R)

Event	Date	Time	Location	Type	Phases		M_L	
39	12-24-85	13:13	59.50N 25.00E	EX-E3		*Lg*	2.6	
40	12-25-85	12:04	60.90N 29.30E	EX-V1C	*Pn*	*Lg*	2.9	
41	12-25-85	13:19	59.30N 27.60E	EX-E6		*Lg*	2.6	
42	12-25-85	14:18	60.00N 28.50E**	EQ	*Pn*	*Lg*	2.7	
43	12-27-85	11:06	61.40N 31.60E	EX-V4	*Pn*		2.2	(H)
44	12-27-85	12:16	59.40N 28.50E	EX-E8	*Pn*	*Lg*	3.3	
45	12-27-85	12:42	61.10N 30.20E	EX-V2	*Pn*		2.4	(H)
46	12-28-85	11:47	57.69N 26.54E	EQ	*Pn*	*Lg*	2.8	
47	12-29-85	21:38	73.29N 6.86E	EQ	*Pn*		4.7	(P)
48	12-30-85	12:03	59.50N 26.50E	EX-E9		*Lg*	2.7	
49	12-30-85	12:19	59.31N 27.34E	--		*Lg*	2.7	
50	12-31-85	6:57	73.36N 6.77E	EQ	*Pn*		4.8	(P)
51	12-31-85	7:10	73.29N 6.70E	EQ	*Pn*		4.6	(P)
52	12-31-85	12:08	63.20N 27.80E	EX-M7	*Pn*		2.3	(H)
53	12-31-85	13:37	58.34N 6.43E	EX-TIT	*Pn*	*Lg*	2.1	
54	1- 3-86	14:59	61.90N 30.60E	EX-V7	*Pn*	*Lg*	2.9	
55	1- 7-86	11:20	60.92N 29.05E	--	*Pn*	*Lg*	2.8	
56	1- 7-86	14:14	58.34N 6.43E	EX-TIT	*Pn*	*Lg*	1.8	
57	1- 9-86	1:59	66.80N 21.80E*	EQ		*Lg*	2.6	
58	1- 9-86	12:08	59.30N 28.10E	EX-E7	*Pn*	*Lg*	2.5	
59	1-13-86	12:06	59.64N 24.07E	--	*Pn*	*Lg*	2.7	
60	1-15-86	12:06	59.40N 28.50E	EX-E8	*Pn*	*Lg*	3.4	
61	1-16-86	12:08	59.40N 28.50E	EX-E8	*Pn*	*Lg*	2.7	
62	1-17-86	12:12	59.30N 28.10E	EX-E7	*Pn*	*Lg*	3.3	
63	1-17-86	14:11	58.34N 6.43E	EX-TIT	*Pn*	*Lg*	2.3	
64	1-20-86	23:38	50.18N 12.31E	EQ	*Pn*	*Lg*	3.3	
65	1-21-86	8:56	55.30N 13.60E*	EQ	*Pn*	*Lg*	2.5	
66	1-25-86	22:58	57.10N 7.00E**	EQ	*Pn*	*Lg*	1.7	
67	1-25-86	23:13	61.48N 16.94E	EQ	*Pn*	*Lg*	2.9	
68	1-31-86	6:00	65.39N 10.65E	EQ	*Pn*	*Lg*	2.5	
69	1-31-86	10:49	61.10N 29.90E	EX-V8	*Pn*	*Lg*	3.3	
70	1-31-86	12:10	59.30N 28.10E	EX-E7	*Pn*		3.3	
71	1-31-86	14:18	58.34N 6.43E	EX-TIT	*Pn*	*Lg*	1.9	
72	2- 2-86	4:57	67.60N 34.00E	EX-K2		*Lg*	2.9	
73	2- 3-86	1:30	59.60N 1.43E	EQ		*Lg*	1.9	
74	2- 5-86	15:23	62.60N 6.80E*	EQ		*Lg*	1.6	
75	2- 5-86	23:36	62.74N 4.50E	EQ	*Pn*	*Lg*	2.3	
76	2- 6-86	6:20	62.90N 4.86E	EQ	*Pn*	*Lg*	1.9	
77	2- 6-86	12:22	59.30N 28.10E	EX-E7	*Pn*	*Lg*	2.6	
78	2- 6-86	16:30	67.10N 20.60E	EX-R1		*Lg*	2.6	
79	2 -7-86	11:00	64.70N 30.70E	EX-V10	*Pn*	*Lg*	3.1	

Event	Date	Time	Location	Type	Phases		M_L	
80	2 -7-86	12:09	59.40N 28.40E	EX-E12		*Lg*	2.5	
81	2- 7-86	12:17	59.20N 31.00E**	EQ		*Lg*	1.9	(R)
82	2- 7-86	14:05	67.60N 34.20E	EX-K5	*Pn*		2.8	(H)
83	2 -7-86	21:03	66.45N 14.89E	EQ	*Pn*	*Lg*	2.2	(H)
84	2-10-86	12:42	59.40N 28.50E	EX-E8	*Pn*	*Lg*	2.7	
85	2-14-86	14:13	58.34N 6.43E	EX-TIT	*Pn*	*Lg*	2.4	
86	2-14-86	17:54	58.34N 6.43E	EX-TIT	*Pn*		2.3	(B)
87	2-16-86	18:20	61.69N 4.90E	EQ	*Pn*		1.7	
88	2-17-86	12:37	59.30N 27.20E	EX-E4		*Lg*	2.5	(H)
89	2-18-86	10:46	59.30N 27.20E	EX-E4		*Lg*	3.1	
90	2-18-86	12:46	64.70N 30.70E	EX-V10	*Pn*	*Lg*	2.6	
91	2-23-86	6:14	67.60N 34.00E	EX-K2	*Pn*	*Lg*	3.1	
92	2-26-86	2:12	62.76N 5.29E	EQ	*Pn*	*Lg*	1.9	
93	3- 5-86	12:13	59.50N 26.50E	EX-E9		*Lg*	3.2	
94	3- 5-86	13:02	57.20N 7.00E**	EQ	*Pn*	*Lg*	1.8	
95	3- 7-86	13:08	59.30N 28.10E	EX-E7	*Pn*	*Lg*	3.3	
96	3- 8-86	16:21	61.67N 2.58E	EQ	*Pn*	*Lg*	1.9	
97	3-10-86	4:20	62.81N 4.91E	EQ	*Pn*	*Lg*	2.1	
98	3-10-86	12:02	59.30N 28.10E	EX-E7	*Pn*	*Lg*	3.2	
99	3-11-86	12:02	59.30N 28.10E	EX-E7	*Pn*	*Lg*	3.2	
100	3-13-86	10:27	61.10N 29.90E	EX-V8	*Pn*		2.8	
101	3-13-86	11:39	60.70N 29.00E	EX-V5	*Pn*	*Lg*	2.9	
102	3-21-86	13:02	59.50N 25.00E	EX-E3		*Lg*	2.6	
103	3-24-86	11:18	59.30N 27.20E	EX-E4	*Pn*	*Lg*	2.5	
104	3-25-86	9:05	62.76N 4.76E	EQ	*Pn*	*Lg*	2.0	
105	3-27-86	12:24	59.40N 28.50E	EX-E8	*Pn*	*Lg*	3.5	
106	3-30-86	3:23	61.66N 4.53E	EQ	*Pn*	*Lg*	1.6	
107	4- 4-86	13:13	58.34N 6.43E	EX-TIT	*Pn*	*Lg*	1.9	
108	4- 4-86	22:43	70.86N 8.91E	EQ	*Pn*		4.4	(H)
109	4- 7-86	0:35	61.84N 4.88E	EQ	*Pn*	*Lg*	2.0	
110	4-14-86	14:55	59.49N 24.11E	--	*Pn*	*Lg*	2.8	
111	4-15-86	10:53	60.90N 29.30E	EX-V1C	*Pn*		3.0	
112	4-16-86	11:51	60.39N 5.34E	EX-NYG		*Lg*	1.8	(B)
113	4-16-86	13:15	58.15N 5.97E	--	*Pn*	*Lg*	2.1	
114	4-18-86	8:33	67.60N 34.00E	EX-K2		*Lg*	2.7	
115	4-19-86	10:59	61.10N 30.20E	EX-V2	*Pn*	*Lg*	2.5	
116	4-28-86	15:53	60.18N 4.88E	--	*Pn*	*Lg*	2.4	
117	4-29-86	17:48	59.82N 24.06E	EQ		*Lg*	2.6	
118	4-30-86	10:19	59.31N 6.95E	EX-BLA	*Pn*	*Lg*	2.2	
119	5- 8-86	17:14	58.70N 17.99E	EQ		*Lg*	2.3	
120	5-16-86	15:02	61.90N 30.60E	EX-V7		*Lg*	3.1	

Event	Date	Time	Location	Type	Phases		M_L
121	5-17-86	16:01	62.94N 4.94E	EQ	*Pn*	*Lg*	2.4
122	5-21-86	8:57	61.65N 31.38E	--		*Lg*	2.6
123	5-27-86	18:36	59.31N 6.95E	EX-BLA	*Pn*	*Lg*	2.3
124	5-28-86	17:52	59.31N 6.95E	EX-BLA	*Pn*	*Lg*	2.4
125	6- 3-86	11:04	59.17N 5.66E	EQ	*Pn*	*Lg*	2.0
126	6- 3-86	14:30	61.46N 4.08E	EQ	*Pn*	*Lg*	2.7
127	6- 4-86	9:07	61.50N 30.40E	EX-V3	*Pn*	*Lg*	3.9
128	6- 6-86	13:14	58.34N 6.43E	EX-TIT	*Pn*	*Lg*	1.7
129	6- 7-86	12:13	59.20N 27.60E	EX-E5		*Lg*	3.0
130	6-12-86	9:31	61.50N 30.40E	EX-V3	*Pn*		3.7
131	6-12-86	13:04	60.90N 29.30E	EX-V1C	*Pn*	*Lg*	2.6
132	6-13-86	14:41	59.66N 24.28E	--	*Pn*	*Lg*	3.1
133	6-15-86	15:01	61.67N 3.85E	EQ	*Pn*	*Lg*	3.2
134	6-16-86	15:59	60.04N 7.24E	EQ		*Lg*	1.1
135	6-19-86	3:55	59.31N 6.95E	EX-BLA	*Pn*	*Lg*	2.5
136	6-20-86	22:08	61.47N 3.92E	EQ	*Pn*	*Lg*	1.6
137	6-23-86	13:14	58.34N 6.43E	EX-TIT	*Pn*	*Lg*	1.8
138	6-25-86	12:33	61.40N 31.60E	EX-V4	*Pn*	*Lg*	2.9
139	6-26-86	4:06	61.88N 5.10E	EQ	*Pn*	*Lg*	2.1
140	6-27-86	3:50	59.28N 6.76E	--	*Pn*	*Lg*	2.4
141	6-27-86	9:00	64.70N 30.70E	EX-V10		*Lg*	2.6
142	6-30-86	17:11	57.46N 27.22E	EQ	*Pn*	*Lg*	2.8
143	7- 1-86	15:28	60.70N 28.70E	EX-V12	*Pn*	*Lg*	2.7
144	7- 8-86	12:06	60.04N 29.36E	--	*Pn*	*Lg*	3.2
145	7- 8-86	13:09	59.30N 27.20E	EX-E4	*Pn*	*Lg*	2.7
146	7-10-86	20:10	59.31N 6.95E	EX-BLA	*Pn*	*Lg*	2.3
147	7-12-86	13:38	62.98N 6.47E	EQ	*Pn*	*Lg*	2.0
148	7-14-86	13:51	58.33N 13.89E	EQ	*Pn*		4.3
149	7-14-86	14:30	61.10N 29.90E	EX-V8	*Pn*	*Lg*	3.2
150	7-14-86	14:45	58.42N 13.90E	EQ	*Pn*	*Lg*	3.4
151	7-14-86	15:02	69.30N 34.40E	EX-K9	*Pn*	*Lg*	3.1
152	7-15-86	18:46	66.97N 13.02E	EQ	*Pn*		3.5
153	7-16-86	11:27	59.30N 27.20E	EX-E4	*Pn*	*Lg*	3.0
154	7-16-86	17:49	59.31N 6.95E	EX-BLA	*Pn*	*Lg*	2.3
155	7-18-86	11:03	59.40N 28.50E	EX-E8	*Pn*	*Lg*	3.1
156	7-18-86	13:42	59.30N 27.60E	EX-E6	*Pn*	*Lg*	3.0
157	7-23-86	13:10	60.80N 29.30E	EX-V1B	*Pn*	*Lg*	2.8
158	7-23-86	20:47	59.31N 6.95E	EX-BLA	*Pn*	*Lg*	2.2
159	7-24-86	10:56	68.10N 33.20E	EX-K4	*Pn*		2.6 (H)
160	7-29-86	13:14	59.31N 6.95E	EX-BLA	*Pn*	*Lg*	2.3
161	7-30-86	11:03	59.30N 28.10E	EX-E7	*Pn*	*Lg*	3.2

Event	Date	Time	Location	Type	Phases		M_L	
162	7-30-86	13:39	59.30N 27.20E	EX-E4		Lg	2.6	
163	7-30-86	13:50	59.34N 27.55E	--	Pn	Lg	2.8	
164	7-30-86	18:00	59.31N 6.95E	EX-BLA	Pn	Lg	2.4	
165	7-31-86	14:23	59.63N 24.48E	--	Pn		3.1	
166	7-31-86	15:06	59.40N 24.60E	EX-E2	Pn	Lg	3.0	
167	8-13-86	15:32	67.10N 20.60E	EX-R1	Pn	Lg	2.6	
168	8-14-86	13:15	58.34N 6.43E	EX-TIT	Pn	Lg	1.9	
169	8-14-86	14:40	59.31N 6.95E	EX-BLA	Pn	Lg	2.4	
170	8-16-86	4:25	62.82N 4.98E	EQ	Pn	Lg	2.3	
171	9- 1-86	22:11	60.82N 2.93E	EQ	Pn	Lg	3.9	
172	9- 2-86	12:54	59.31N 6.95E	EX-BLA	Pn	Lg	2.1	
173	9- 4-86	11:23	60.96N 28.99E	--		Lg	3.0	
174	9- 9-86	17:56	59.31N 6.95E	EX-BLA	Pn	Lg	2.4	
175	9-18-86	15:54	60.77N 20.68E	EQ	Pn	Lg	2.5	
176	9-20-86	22:15	60.03N 16.29E	EQ	Pn	Lg	3.3	
177	9-30-86	20:03	60.79N 4.23E	EQ	Pn	Lg	1.9	
178	10- 1-86	14:15	58.34N 6.43E	EX-TIT	Pn	Lg	1.9	
179	10- 9-86	14:14	58.34N 6.43E	EX-TIT	Pn	Lg	2.0	
180	10-10-86	19:57	61.97N 2.33E	EQ	Pn	Lg	2.1	
181	10-26-86	11:45	61.46N 3.29E	EQ	Pn	Lg	2.4	
182	10-26-86	11:57	61.72N 3.27E	EQ	Pn	Lg	2.6	(B)
183	10-29-86	21:05	60.81N 3.04E	EQ	Pn	Lg	2.3	
184	11- 1-86	14:55	62.47N 6.19E	EQ	Pn	Lg	2.4	
185	11- 2-86	7:48	58.58N 13.44E	EQ	Pn	Lg	3.4	(B)
186	11-13-86	8:01	58.17N 8.10E	EQ	Pn	Lg	1.8	

* *RONAPP* Location

** *SAIAP* Location

(B) Bergen network magnitude

(H) Helsinki network magnitude

(P) PDE magnitude (M_b)

(R) *RONAPP* uncorrected magnitude

The M_L are based on the Lg amplitude computed by *RONAPP*. They differ slightly from the *RONAPP* M_L in the NORESS bulletin by being distance-corrected to the event location computed by one of the independent networks. For some events *RONAPP* had no detected Lg phase, or chose the wrong phase as Lg. For these events the M_L is that reported by one of the independent networks (if available) or the *RONAPP* uncorrected magnitude. These are listed in Table 2.1 for information but were not included in any subsequent analysis. The relation between seismic moment and magnitude (Section 2.7) was derived using only events with distance-corrected NORESS magnitudes.

The 186 events used in the inversion include 107 explosions, 63 presumed earthquakes, and 16 events of unknown source type. The Pn inversion included 152 of these events, with 83 explosions, 56 presumed earthquakes, and 13 events of unknown source type. The Lg inversion used 160 events, including 92 explosions, 53 presumed earthquakes, and 15 unknown. Of the 186 events, 126 were used for both the Pn and the Lg analyses. The NORESS array location and event epicenters are plotted in Figure 2.1. The distance range 300-450 km is dominated by events in west to southwest Norway, while events from 700 to 1200 km are located primarily to the east of NORESS. If the attenuation along paths to the east is distinctly different from that along paths to the west, then our inversion would give an average Q which would not adequately represent spectra from either direction. However, separate inversions were run for restricted azimuth windows, and significant path differences were not observed.

2.3 Signal processing

The calculation of the Pn spectra is incorporated into an automated seismic array processing program (SAIAP) developed as an extension of the RONAPP program used at NORSAR [*Mykkeltveit and Bungum*, 1984]. The program computes spectra for each automatically detected signal. The spectral estimation technique is that proposed by *Bache et al.* [1985]. A 10% cosine-squared taper is applied to a 5-s window starting 0.3 s before the onset time of the arrival on the vertical component. The time series is padded with zeros to 512 samples and fast Fourier transformed. The same procedure is applied to a noise sample taken prior to the first P detection. The squared noise amplitude spectrum (power) is subtracted from the squared signal spectrum (energy density). The resulting noise-corrected signal spectra are averaged across the array and corrected for the instrument response. *Bache et al.* [1985] point out that if the noise is random, stationary, and uncorrelated with the signal, the signal spectrum estimate obtained with this method converges to the true signal spectrum as the number of elements increases. Array averaging has the desirable effect of suppressing uncorrelated local site effects. We experimented with Pn window lengths of 5, 10, and 15 s and found that the spectra are insensitive to that parameter (Figure 2.2).

The inversion results presented here were obtained using Lg spectra computed for a fixed group velocity window of 3.6-3.0 km/s. The spectra were computed for each array element, corrected for the ambient (pre-Pn) noise, and array-averaged using the method of *Bache et al.* [1985]. Our low group velocity cutoff was chosen as 3.0 km/s because our events typically produced Lg phases with low signal/noise for group velocities less than this. Section 2.9 compares the inversion results using Lg spectra computed with FGV and FTL windows.
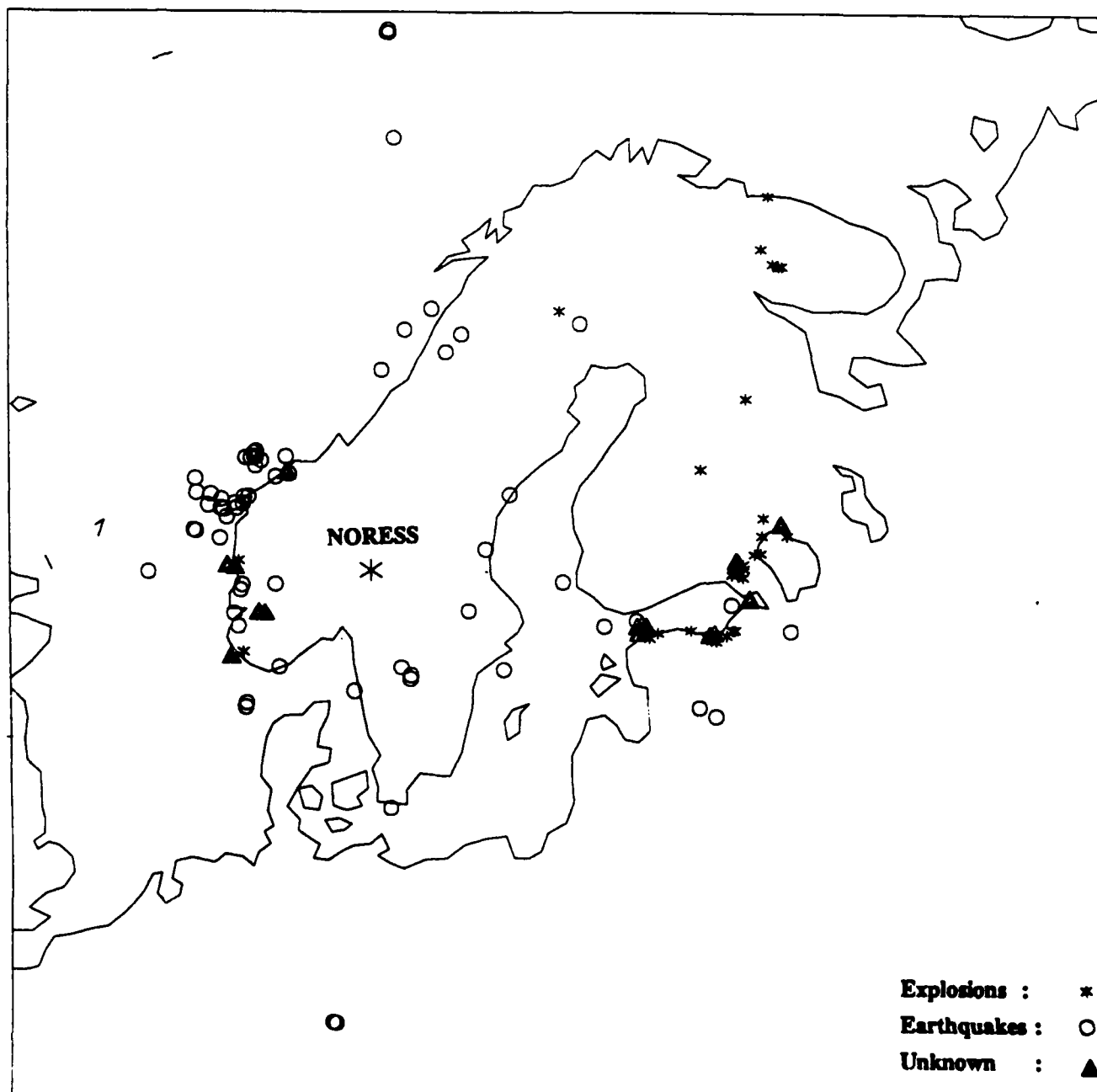
Figure 2.1. Map of the epicenters of events used in the inversion. Earthquakes, explosions, and sources of unknown type are plotted with different symbols. The total number of events is 186. Of these, 152 were used in the *Pn* inversion and 160 were used in the *Lg* inversion.
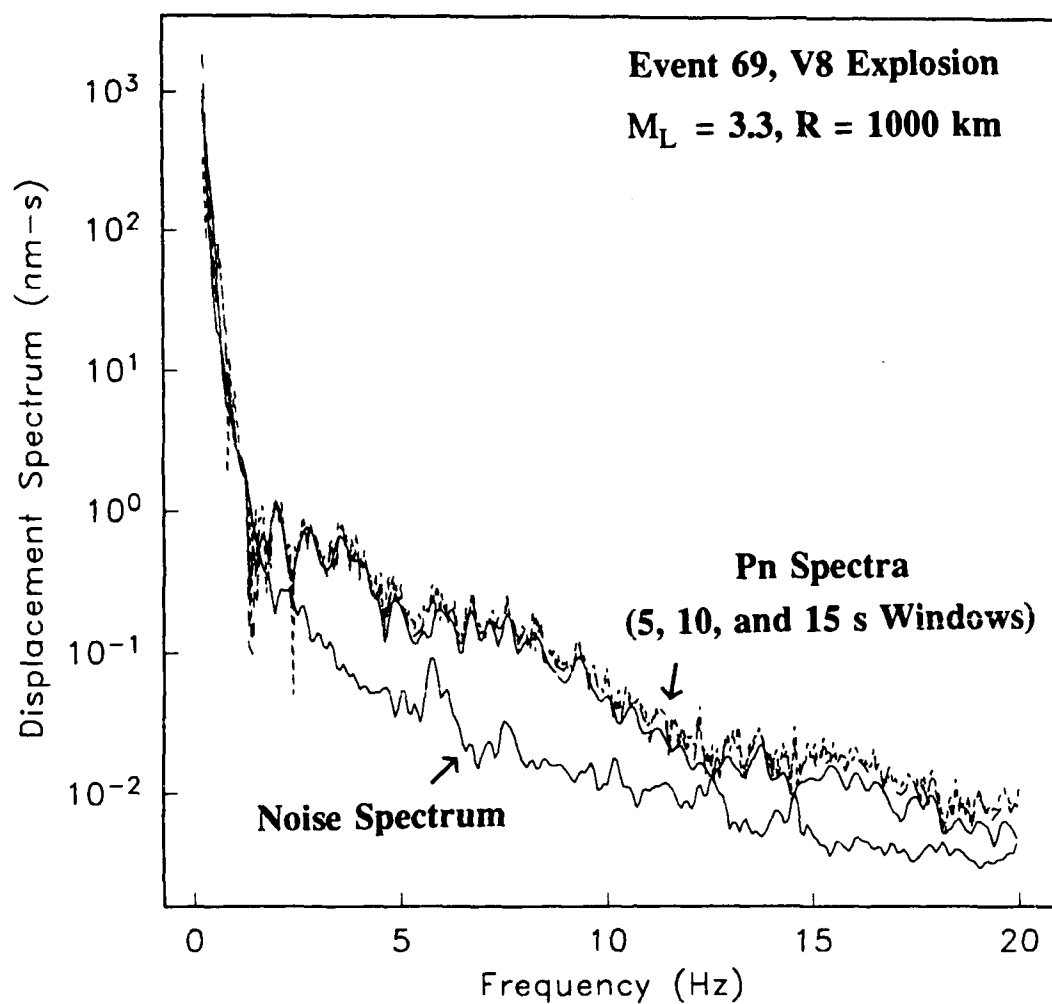
Figure 2.2. Examples of *Pn* spectra for a V8 mine blast (Event 69, Table 2.1) computed for 5, 10, and 15 s windows. The noise spectrum was computed for a 5 s window prior to *Pn*.

Previously, we applied 2 Hz smoothing to the spectra [*Sereno et al.*, 1987]. However, after inverting both smoothed and raw spectra we find no significant difference in the results, except that smoothing causes an artificially small data variance. Therefore we use the raw spectral amplitudes throughout this analysis.

2.4 Pn spectra and Q

Regional *Pn* spectra of 152 events were inverted between 1 and 15 Hz, sampled every 0.25 Hz. However, we note that at ranges less than 300-400 km, *Pn* and *Pg* arrive within the same 5-s window, so it is possible that some of our short-range spectra include a *Pg* contribution. The number of data in the *Pn* inversion is 8664, and the number of parameters is 155. The *Pn* spectra were corrected for geometric spreading and inverted for seismic moment and $Q(f)$.

The apparent attenuation from the *Pn* inversion is represented by $Q_{Pn}(f) = 325f^{0.48}$. Selected examples of the fit of theoretical spectra to data spectra are shown in Figure 2.3. The *Pn* amplitude is more variable than the *Lg* amplitude, probably due to greater sensitivity to source radiation pattern, focusing/defocusing, and scattering. Nevertheless, acceptable fits to the *Pn* spectra were achieved with our simple parameterization. However, we recognize that our $Q_{Pn}(f)$ is an empirical representation of observed data, and we do not interpret it in terms of upper mantle rheology.

2.5 Lg spectra and Q

Regional *Lg* spectra of 160 events were inverted between 1 and 7 Hz, sampled every 0.25 Hz. The spectra were computed for the fixed group velocity range 3.6-3.0 km/s. The possibility that these spectra are contaminated by *Sn* coda at high frequency [*Chun et al.*, 1987; *Ringdal*, 1986; *Shin and Herrmann*, 1987] is discussed in Section 3. The number of data in the *Lg* inversion is 4000, and the number of parameters is 163.

The attenuation resulting from the inversion is $Q_{Lg}(f) = 560f^{0.26}$. Selected examples of the fit of theoretical spectra to data spectra are shown in Figure 2.4. All of these events have corner frequencies greater than 6 Hz, so the source parameterization has only a minor effect on the results. Numerical modeling of *Lg* suggests that its observed attenuation is an effective measure of the average absorption of shear waves in the crust [*Campillo et al.*, 1985]. Our $Q_{Lg}(f)$ is therefore an approximation to the average Q_β of the crust, although it also includes the effects of apparent attenuation due to scattering.

Table 2.2 compares our *Lg* attenuation estimate to those for various regions. Entries 1-4 are attenuation estimates for paths in the western United States. With the exception of *Chavez and Priestley* [1986], these studies are band limited to relatively low frequencies. Entries 5-10 are estimates for paths across eastern North America. An obvious conclusion is that the tectonically active western United States is characterized by a lower Q and stronger frequency dependence than the stable eastern North American shield. Our $Q_{Lg}(f)$ falls between the ENA and WUS estimates.
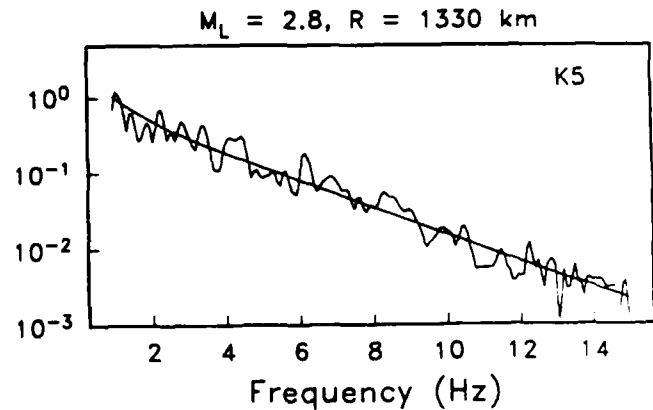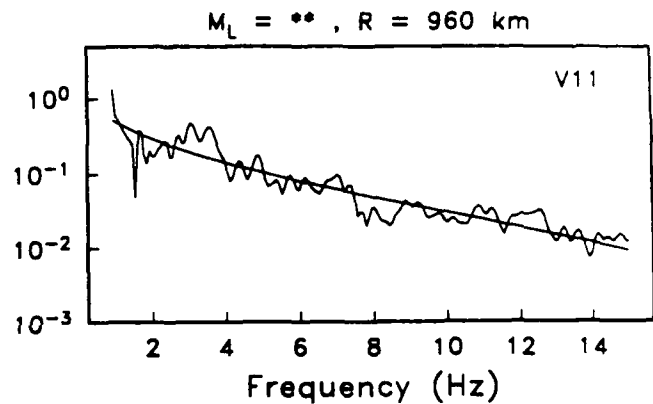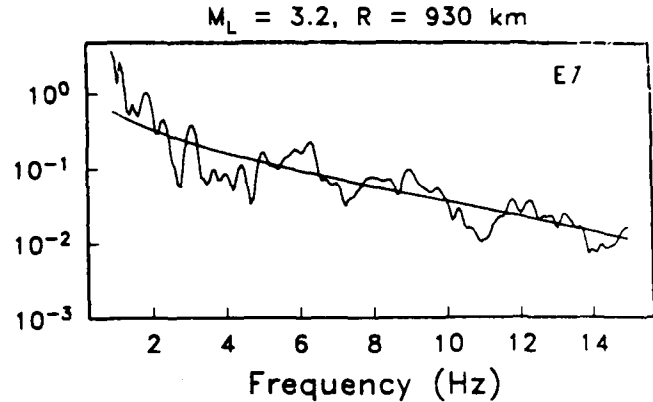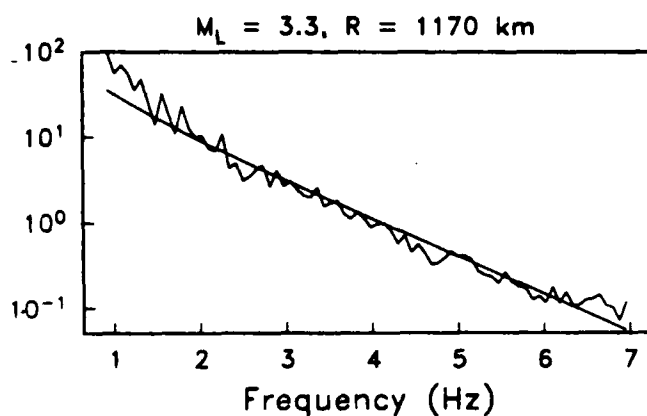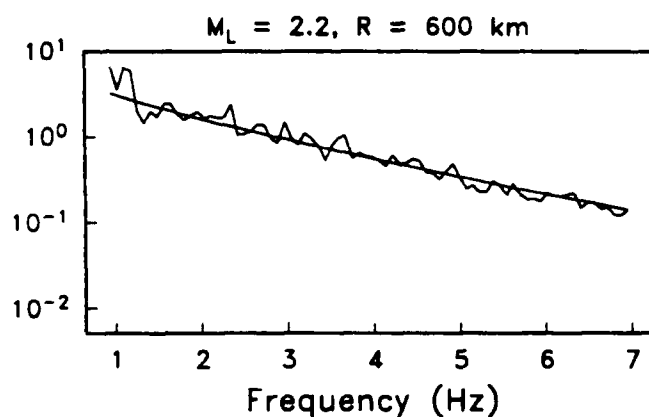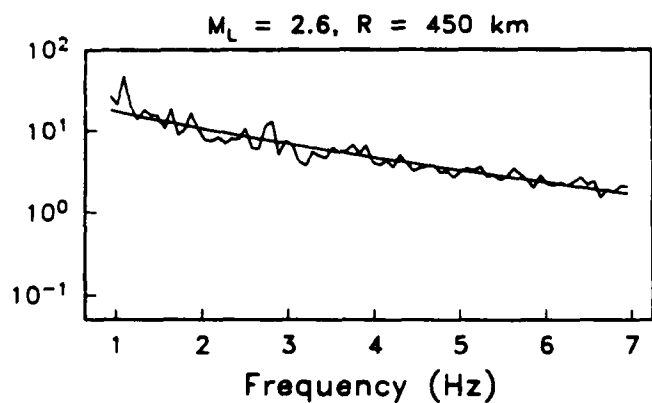
16
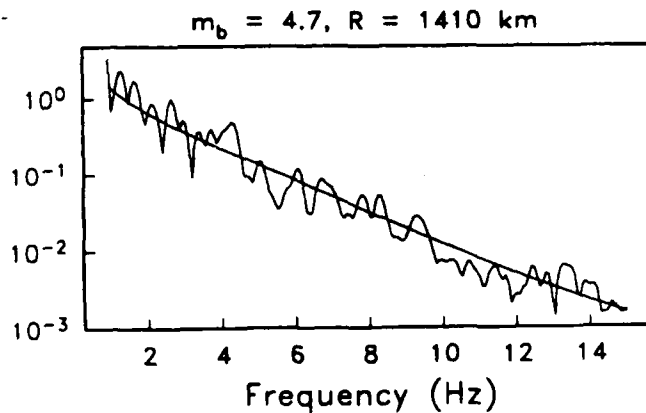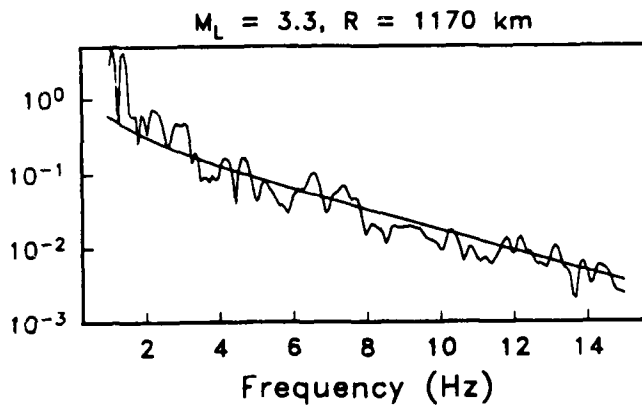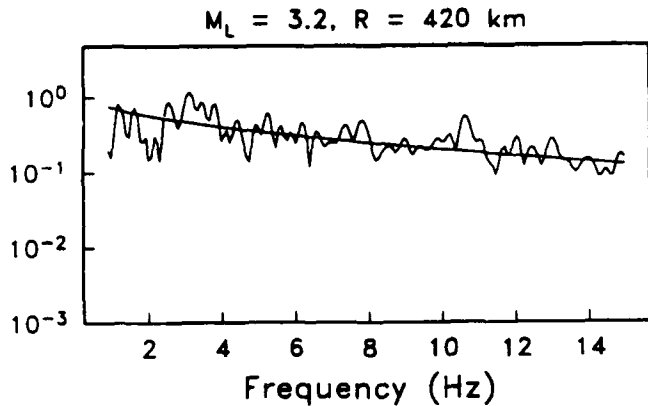
Figure 2.3. Selected comparisons of theoretical *Pn* spectra based on the inversion results to observed spectra. *Pn* spectra of three earthquakes are on the left, and *Pn* spectra of three mine blasts are on the right. All spectra are labeled by the event local magnitude and epicentral distance. The explosion spectra are labeled by the University of Helsinki mine identification code. Local magnitude was not available for the V11 mine blast. The spectral amplitudes are in nanometer-seconds.
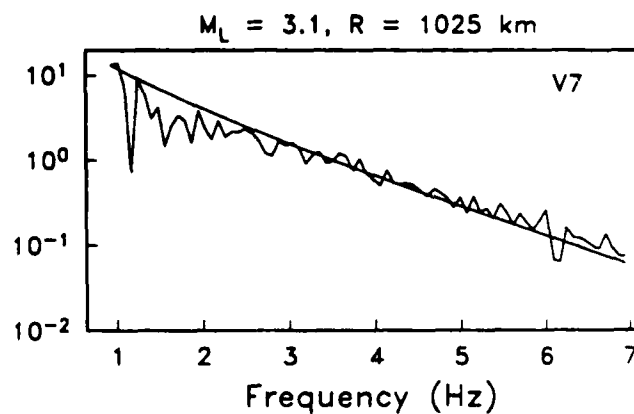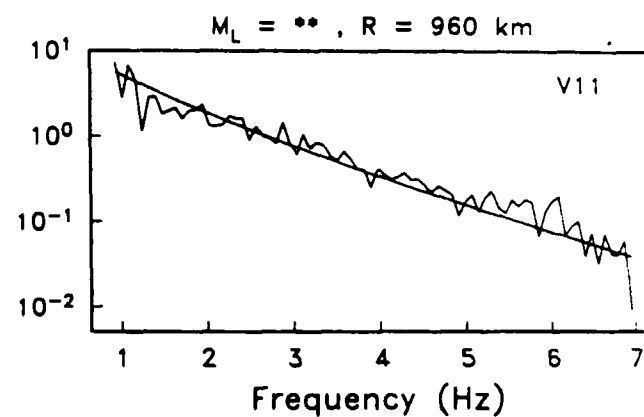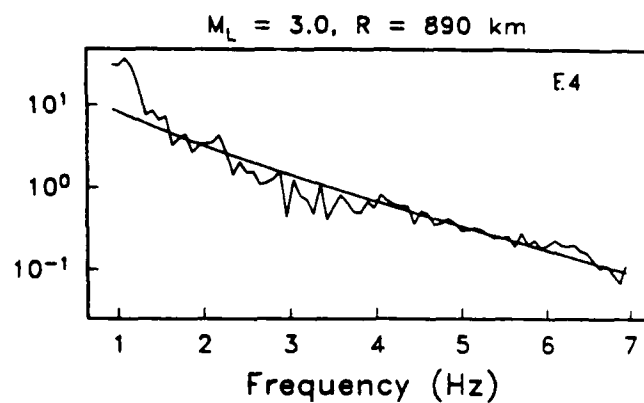
Figure 2.4 Selected comparisons of theoretical Lg spectra based on the inversion results to observed spectra. Lg spectra of three earthquakes are on the left, and Lg spectra of three mine blasts are on the right. All spectra are labeled by the event local magnitude and epicentral distance. The explosion spectra are labeled by the University of Helsinki mine identification code. Local magnitude was not available for the V11 mine blast. The spectral amplitudes are in nanometer-seconds.

18

Table 2.2. Reported $Q_{Lg}(f)$ estimates.

	Region	Frequency, Hz	$Q_{Lg}(f)$		Reference
			Q_0	η	
1	western United States	0.5–3.5	140–200	0.4–0.6	*Singh and Herrmann* [1983]
2	western United States (NTS explosions)	1.0–2.0	200–300	0.2–0.4	*Peseckis and Pomeroy* [1984]
3	western United States (NTS explosions)	1.0–2.0	139	0.6	*Nuttli* [1986]
4	western United States (Great Basin)	0.25–12.5	206	0.68	*Chavez and Priestley* [1986]
5	eastern United States	0.5–3.5	1000	0.3–0.4	*Singh and Herrmann* [1983]
6	eastern North America	1.0–15.0	900	0.2	*Hasegawa* [1985]
7	eastern United States	0.5–14.0	1000	0.35	*Goncz et al.* [1987]
8	eastern Canada	0.6–10.0	1100	0.19	*Chun et al.* [1987]
9	eastern United States	0.5–7.0	800	0.32	*Gupta and McLaughlin* [1987]
10	eastern North America	0.5–15.0	500–550	0.65	*Shin and Herrmann* [1987]
11	central France	0.5–10.0	290	0.52	*Campillo et al.* [1985]
12	southern Africa	–	600	0.4	*Mitchell et al.* [1987]
13	Scandinavia	1.0–7.0	560	0.26	this study

The most relevant comparison of our result to those of other studies is that of spectral shape. Figure 2.5 plots $\exp(-\pi f t/Q(f))$ for the Q models in Table 2.2. Note that the spectral shape for our Q model is similar to that predicted for the low exponent ENA Q models (entries 6 and 8 of Table 2.2). However, models with large Q_0 and strong frequency dependence (like entry 10) give spectra that severely overestimate the ratio of high- to low-frequency energy seen in the NORESS data.

Our Q_{Lg} estimate is controlled by data from ranges between 300 and 1200 km. We are not aware of comparable estimates of Q in Scandinavia. However, *Kvamme and Havskov* [1985] estimated from spectral ratios of S waves from local events in southern Norway, $Q = 127 f^{1.08}$. Although the frequency dependence differs significantly, our Q_{Lg} is equal to their Q_S at about 6 Hz. All their data are from events at epicentral distances les' than 300 km, and their analysis extended to 16 Hz. Since the ray paths of local S waves are restricted to shallower depths in the crust, one plausible explanation for the difference is that the stronge: frequency dependence is caused by a higher concentration of scatterers at shallow depth. However, it may be that the differences are methodological, and therefore without much physical significance.

2.6 Pn/Lg consistency

An important constraint on the attenuation estimates is the consistency of the derived source parameters from the independently inverted Pn and Lg spectra. In particular, the ratio of the Lg to Pn long-period source levels should be range-independent. Range dependence would indicate that geometric spreading and/or Q have been improperly modeled for one or both phases. Figure 2.6 is a plot of $S_0(Lg)/S_0(Pn)$ for the 126 events common to both inversions. Note that for explosions the ratio does not show evidence of range dependence (models that do show a range dependence are discussed in the Section 2.8). There is a much larger scatter in the earthquake ratios, as expected from source radiation pattern effects. Based on the explosion data, the range-independent value of $S_0(Lg)/S_0(Pn)$ is 0.74. Combining equations (2.3), (2.4), and (2.5), this implies that for earthquakes and explosions of equal moment,

$$\frac{S_0^{exp}(Lg)}{S_0^{exp}(Pn)} = \kappa \frac{\rho_s \alpha_s^3}{\rho_c \beta_c^3} = 0.74 \qquad (2.8)$$

Assuming near-surface values of $\rho_s = 2.5$ g/cm^3 and $\alpha_s = 5.0$ km/s and average crustal values of $\rho_c = 2.7$ g/cm^3 and $\beta_c = 3.5$ km/s, we have $\kappa = 0.27$. From (2.5), this means that the average Lg earthquake excitation is approximately 4 times the average Lg explosion excitation for sources of equal moment. Others have observed similar ratios. For example, *Willis* [1963] compared Lg amplitudes from an NTS explosion and a colocated earthquake at a range of 450 km and found a value of 5 for this ratio. *Pomeroy* [1977] found a ratio of 3-5 for relative Lg excitation by comparing 12 earthquakes to the SALMON nuclear explosion detonated in Mississippi. *Nuttli* [1981] compared Lg/P amplitude ratios for explosions and earthquakes in the western and central parts of the Soviet Union. He found that the average ratio was 3.5 times greater for earthquakes than for explosions, although there was considerable overlap. *Murphy*
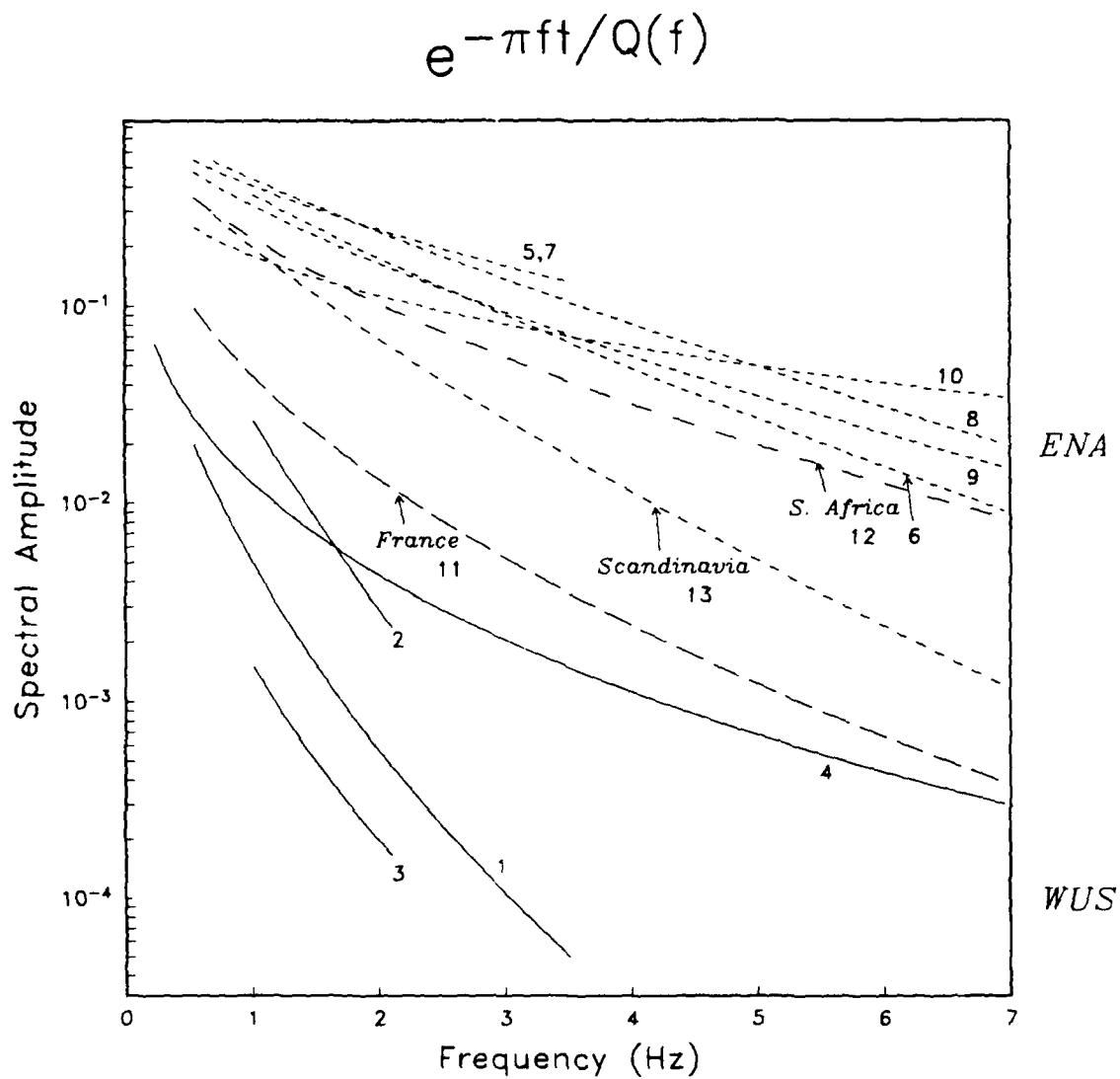
$$e^{-\pi ft/Q(f)}$$

Figure 2.5. *Lg* spectral attenuation for the Q models listed in Table 2.2 and for our Scandinavian Q estimate. The curves are identified by their numbered entries in Table 2.2. Attenuation is plotted as $\exp[-\pi ft/Q(f)]$, where the travel time t is appropriate for a range of 1000 km. Note the distinct offset between eastern North America (ENA) and western United States (WUS).
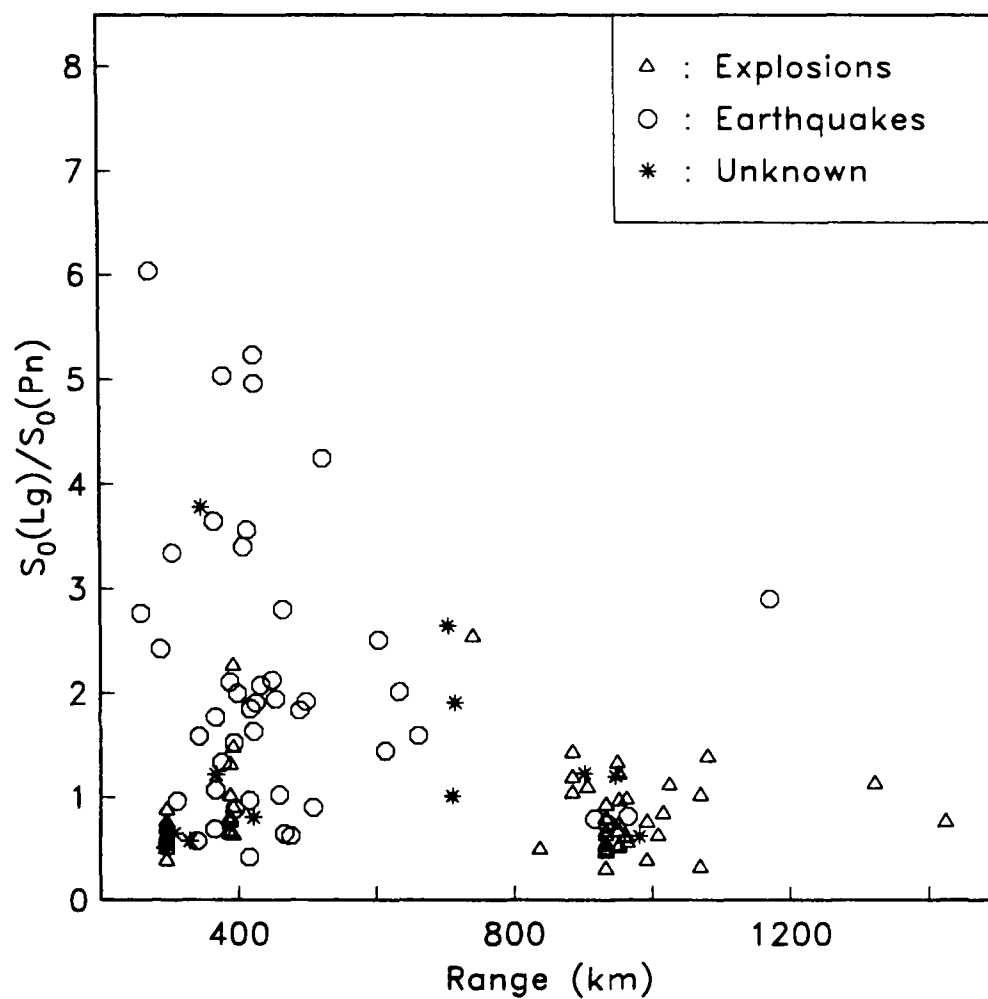
21

Figure 2.6. Ratio of *Lg* to *Pn* inverted long period source levels as a function of epicentral distance. Explosions, earthquakes, and events of unknown source type are plotted with different symbols.

22

and Bennett [1982] compared Nevada Test Site (NTS) explosions to nearby earthquakes and found that observed Lg amplitudes were typically greater for earthquakes than for explosions with comparable P wave amplitudes, though again there is much scatter and overlapping between the two populations. We will address the sensitivity of κ to the spreading assumptions in the next section. Finally, we note in Figure 2.6 that the $S_0(Lg)/S_0(Pn)$ ratio separates many of the earthquakes from the explosions. However, there is considerable overlap, and the large ratios for some earthquakes are presumably due to the source radiation pattern for Pn.

The corner frequency parameter c derived from Lg spectra is 19.9, and from Pn spectra it is 25.8. With the $S_0(Lg)/S_0(Pn)$ ratio of 0.74 typical for the explosions, the ratio of Lg and Pn derived corner frequency is 0.85. This is surprisingly close agreement since corner frequency is not well constrained in the Lg inversion (Section 2.8). Based on these attributes, we conclude that our $Q(f)$ models result in consistent source parameters (moment and corner frequency) for the events common to both inversions, and this substantially improves confidence in the validity of the results.

2.7 Seismic moment and corner frequency

Regional Lg phases have also been used to estimate source parameters, including corner frequency and seismic moment [*Street et al.*, 1975; *Dwyer et al.*, 1983; *Hasegawa*, 1983; *Shin and Herrmann*, 1987]. The results are generally consistent with those from near-field source studies, with the possible exception that corner frequencies obtained from Lg tend to be lower than those estimated at short range [*Mueller and Cranswick*, 1985].

Seismic moment is estimated from the inversion parameter S_0 using equations (2.3) and (2.4) with $\rho_s = 2.5$ g/cm^3, $\alpha_s = 5.0$ km/s, $\rho_c = 2.7$ g/cm^3, and $\beta_c = 3.5$ km/s. In Figure 2.7 we plot explosion moment versus NORESS local magnitude (including only events with consistent distance-corrected M_L based on RONAPP Lg amplitudes). The inset in Figure 2.7*b* compares the range dependence of the RONAPP magnitude correction table at 1 Hz to our Lg attenuation model and demonstrates their consistency. The least squares linear fits to log M_C are given by

$$Pn : \log M_0^{\text{exp}} = 1.08 \, M_L + 17.6 \tag{2.9}$$

$$Lg : \log M_0^{\text{exp}} = 1.04 \, M_L + 17.7 \tag{2.10}$$

where we assume $\kappa = 0.27$ for Lg. The value of κ affects the intercept, but not the slope in (2.10). Comparing the two moment-magnitude relationships, the M_0^{exp} derived from Lg is equal to that from Pn when $M_L = 2.5$. This is near the center of the M_L distribution for our data set and provides further confirmation of the internal consistency of our analysis. The large scatter in the explosion moments near $M_L = 3.0$ results from systematic variations in the Lg amplitude for explosions in two sets of western USSR mines [*Henson and Bache*, 1988; *Sereno et al.*, 1987]. Mine blasts south of the Gulf of Finland produce larger Lg amplitudes at NORESS than their counterparts to the north for fixed moment. However, the shapes of the Lg spectra from these mine blasts are consistent with the same Q model. One possible explanation is that Lg propagation is structurally inhibited north of the Gulf of Finland; another is that different mining practices result in distinctly different Lg excitations.

23

(a)

Pn Inverted Moment vs M_L — Explosions
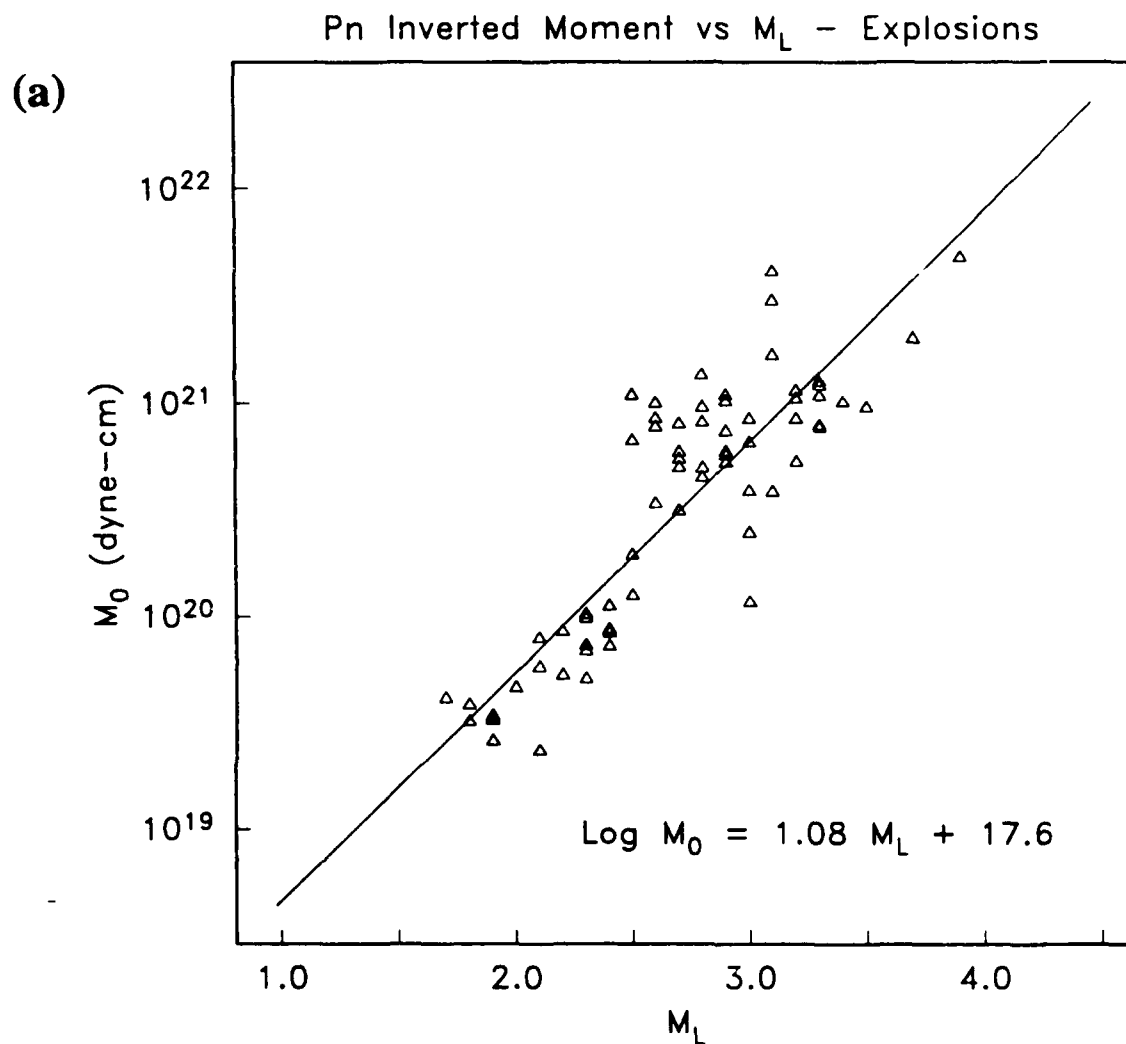
$$\text{Log } M_0 = 1.08 \; M_L + 17.6$$

Figure 2.7. Inverted explosion moment versus NORESS local magnitude for (a) Pn and (b) Lg with $\kappa = 0.27$. The best fitting straight line to log M_0^{exp} is shown in both Figures 2.7a and 2.7b. The inset in Figure 2.7b compares the 1-Hz magnitude correction table used in RONAPP (asterisks) to the distance dependence of 1-Hz Lg waves predicted by our inversion results (dashed curve).
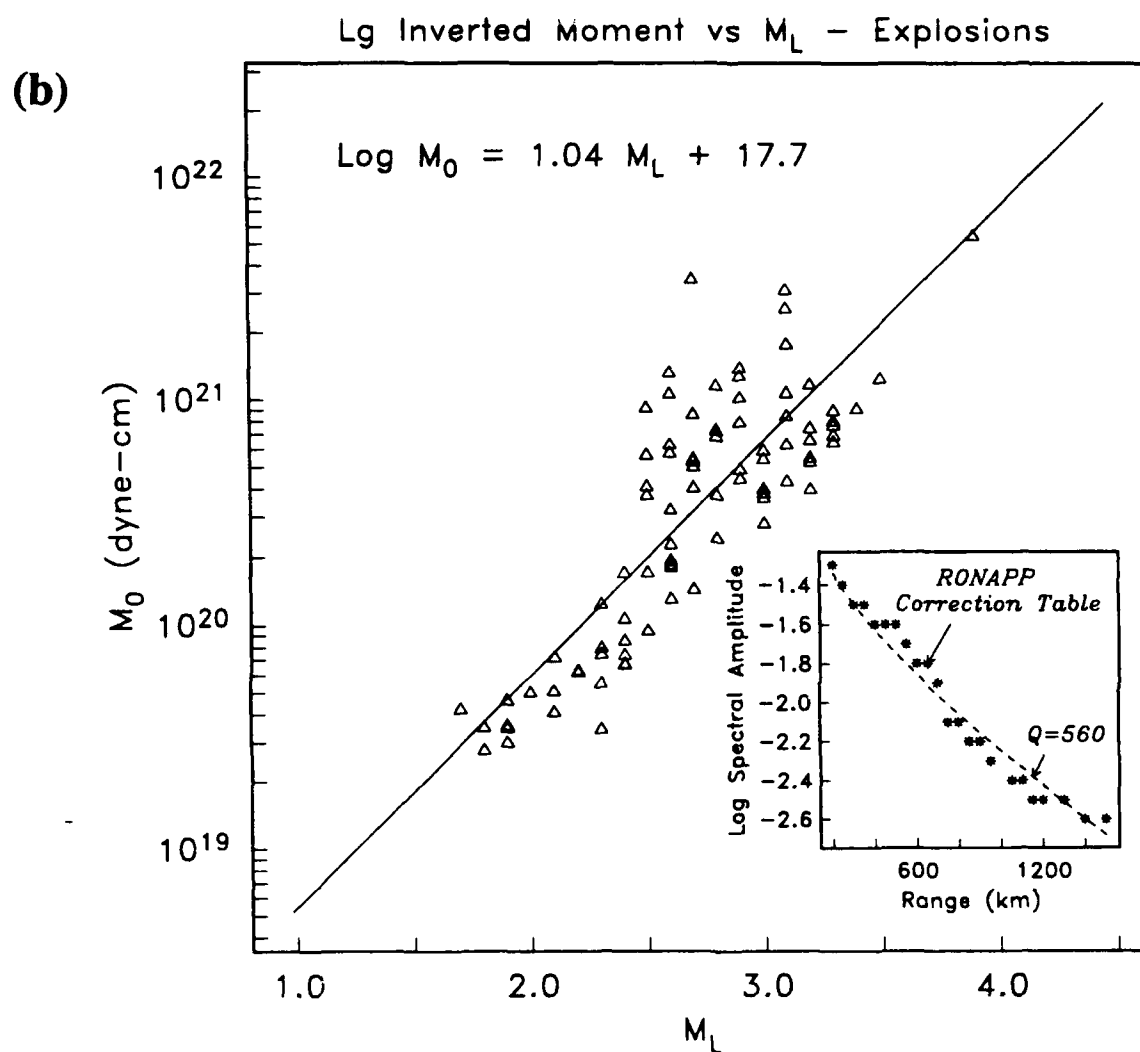
Figure 2.7. (Continued).

The earthquake moments were estimated from Lg using (2.4), and the results are displayed in Figure 2.8. The least squares linear fit to these data is

$$\log M_0^{eq} = 1.03 \, M_L + 17.1 \tag{2.11}$$

Comparing (2.11) to (2.9) and (2.10) for equivalent moments, the earthquake M_L is larger than the explosion M_L by 0.6, which corresponds to a factor of 4 in Lg amplitude. Table 2.3 compares our earthquake moment-magnitude relation (2.11) to results from previous studies including *Bungum et al.* [1982], who used near-field S wave spectra from the 1978 Meloy earthquake sequence in northern Norway. Our results generally agree with those from these other studies. Since magnitude does not enter the inversion, this result lends considerable support to our derived Q model.

Table 2.3 Reported moment-magnitude relations.

M_L	ρ, g/cm^3	β, km/s	$\log M_0$	Distance	Reference
−0.4–2.2	2.7	3.5	$0.90 M_L + 17.5$	near-field	*Bungum et al.* [1982]
1.0–3.5	2.7	3.5	$1.01 M_L + 16.7*$	near-field	*Mueller and Cranswick* [1985]
2.1–4.3	2.8	3.8	$1.18 M_L + 16.6*$	regional	*Shin and Herrmann* [1987]
1.0–4.2	2.8	3.8	$0.94 M_L + 17.32$	regional	*Hasegawa* [1983]
1.8–4.9	2.5	3.5	$1.26 M_L + 16.44$	< 200 km	*Dwyer et al.* [1983]
1.1–3.8	2.7	3.5	$1.03 M_L + 17.1$	regional	this study

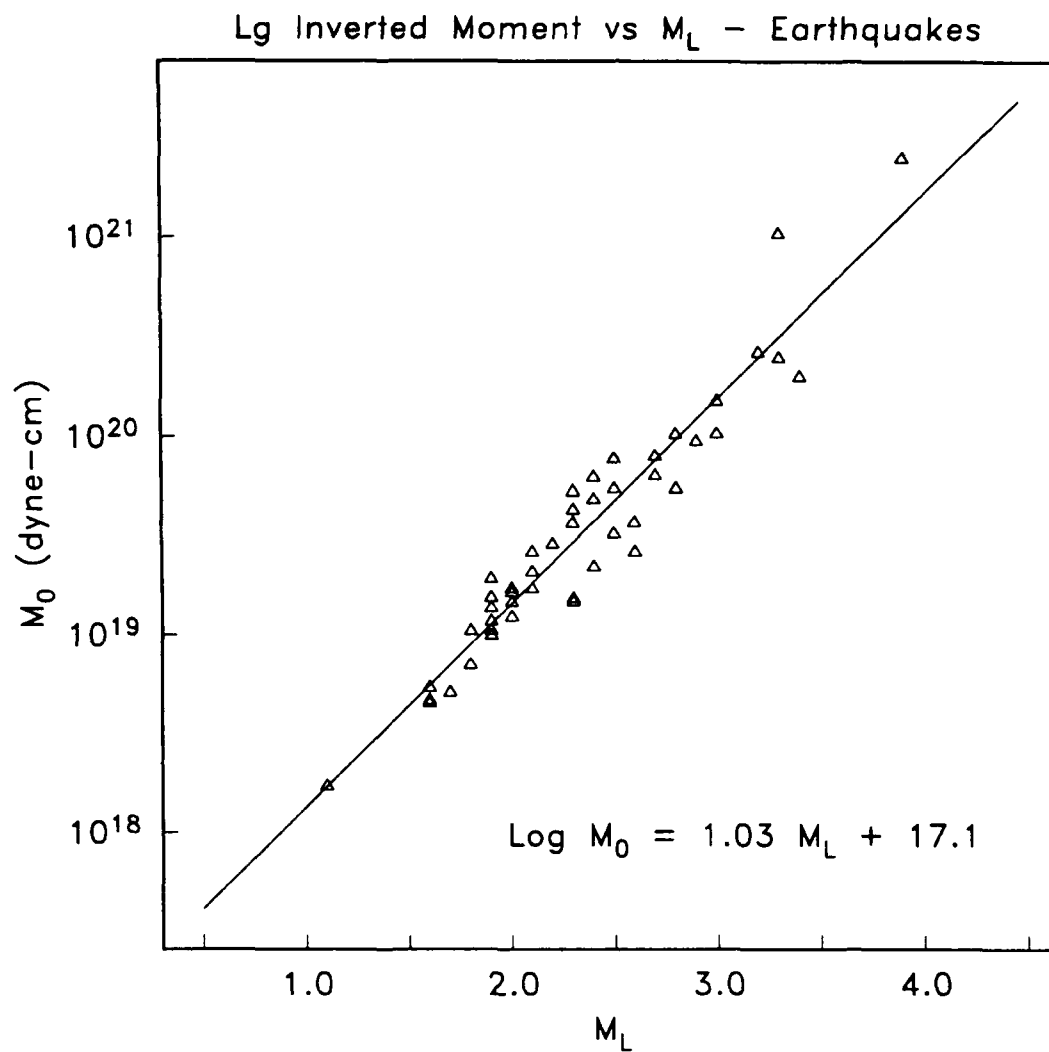* We estimated the regression coefficients from tabulated moments and magnitudes.

Figure 2.8. Inverted earthquake moment versus NORESS local magnitude for *Lg*. The solid line is the best fitting straight line to log M_0^{eq}.

Corner frequency was assumed to scale inversely with the cube root of the long-period source level (2.2), and we inverted for the scaling constant c. Our results indicate that an M_L = 3.0 earthquake has a corner frequency of approximately 10 Hz. Most of the events have M_L < 3.0 and thus have higher corner frequencies. Therefore the data are not adequate to resolve source corner frequency accurately, but we note that our results are consistent with those from similar studies. For example, *Bungum et al.* [1982] expressed the corner frequency-moment relationship for the 1978 Meløy earthquake sequence in northern Norway as

$$f_c = -205 + 30.8 \log M_0 - (\log M_0)^2 \qquad (2.12)$$

Adopting their moment-magnitude relation (Table 2.3), this gives a corner frequency of 9 Hz for an M_L = 3.0 event. Similarly, a least squares fit to the Miramichi aftershock corner frequencies derived by *Mueller and Cranswick* [1985] gives a corner frequency of 12 Hz for an M_L = 3.0 earthquake (assuming cube root scaling). In general, the corner frequencies derived in this study are within a few hertz of those from near-field estimates for events with the same local magnitude.

2.8 Parameter uncertainty

The *Pn* and *Lg* inversions produce a range of models that cannot be ranked by their data variance. In the previous sections we described our "preferred model," but in this section we define the range of acceptable models and the basis upon which we selected the model we prefer. The following summarizes the selection process.

1. For fixed source and spreading assumptions, identify the full range of parameter trade-offs for each phase (models that produce essentially the same data variance). Estimate the formal inversion errors.

2. For fixed source and spreading assumptions, select *Pn* and *Lg* Q models that give consistent source parameters for the events common to both inversions. That is, constrain $S_0(Lg)/S_0(Pn)$ to be range-independent. This reduces the acceptable solutions to a set of model pairs. That is, for a fixed Q_{Lg} model, tight bounds are placed on acceptable Q_{Pn} models.

3. Analyze the trade-off between data variance and M_0-M_L variance. Models which reduce the data variance increase the variance of the M_0-M_L relation. Exclude models that increase either variance without significant decrease in the other. The "preferred model" (for fixed source and spreading assumptions) is selected from the midrange of the acceptable model pairs.

4. Analyze the effect of the source assumptions. The results are not strongly dependent upon the details of our source assumptions because of the high apparent corner frequencies for most of the events.

5. Analyze the effect of the geometric spreading assumptions. We fix *Lg* spreading and change the *Pn* spreading rate. The new set of Q_{Pn} models are input to steps 2 and 3 to define acceptable models for the *Pn* spreading rate. Require that the *Lg* earthquake-explosion ratio be consistent with the results of previous studies to bound the acceptable *Pn* spreading.

Each of these steps will now be discussed in some detail. First, we discuss the formal inversion errors, noting that the relatively small formal errors obtained do not reflect the true uncertainty in our parameter estimates. Then we discuss the trade-offs among model parameters for the fixed spreading and source assumptions used in the previous section and explore the consequences of changing these assumptions.

Formal inversion errors. The variance of the inversion is defined as the sum of the squared data residuals divided by the number of data (nd) minus the number of parameters (np). That is,

$$\sigma_d^2 = \frac{1}{nd-np} \sum_{i=1}^{nd}(d_i - d_i^{th})^2 \qquad (2.13)$$

In this case, the data are log amplitudes corrected for geometric spreading. The variance of the *Pn* inversion is approximately 0.09 and the *Lg* variance is approximately 0.05. These errors only include the estimated uncertainty in the spectral estimate for fixed moment and do not include the scatter in the moment-magnitude relationship.

Formal error estimates on the individual inversion parameters are obtained from the parameter covariance matrix. Our "preferred model" had Lg $Q_0 = 560$ with a standard deviation of ± 11 and $\eta = 0.261 \pm 0.009$. The Q_{Pn} model had $Q_0 = 325 \pm 12$ and $\eta = 0.484 \pm 0.012$. The corner frequency parameters are $c(Pn) = 25.78 \pm 0.05$ and $c(Lg) = 19.88 \pm 0.03$. The artificially small formal errors on c are a consequence of the poor resolution of this parameter. That is, damping has decreased the variance of the estimate with an associated decrease in its resolution. On the average, the standard deviations of the individual S_0 estimates were about 10%. The standard errors of the explosion moment-magnitude relations are $\log M_0 = 1.08(\pm 0.07) M_L + 17.6(\pm 0.2)$ for Pn and $\log M_0 = 1.04(\pm 0.07) M_L + 17.7(\pm 0.2)$ for Lg. The Lg earthquake moment-magnitude relation is $\log M_0 = 1.03(\pm 0.05) M_L + 17.1(\pm 0.1)$.

Parameter trade-off. Here we discuss the trade-offs among M_0, Q_0, η, and c for fixed source and spreading assumptions. The low-frequency spectral level depends on M_0 and Q_0. When M_0 increases, Q_0 decreases to preserve the fit to the long-period spectral level and slope. When Q_0 decreases, η increases to preserve the fit to the high-frequency spectrum. The corner frequency scaling parameter c is constrained by a few large events, and increases in the M_0 estimates cause c to increase to retain approximately the same corner frequency for these events. These trade-offs are illustrated in Table 2.4 with six models that fit the Lg data with nearly equal fidelity (their data variances differ by less than 2%).

Table 2.4. *Lg* parameter trade-off.

Model Index	Q_0	η	c	$\log M_o^{exp}$ ($\kappa = 0.27$)	$\log M_o^{eq}$	σ_d^2
1	569	0.26	19.2	$1.03 M_L + 17.70$	$1.03 M_L + 17.08$	0.0524
2*	560	0.26	19.9	$1.04 M_L + 17.69$	$1.03 M_L + 17.09$	0.0523
3	502	0.30	23.8	$1.09 M_L + 17.63$	$1.03 M_L + 17.13$	0.0519
4	470	0.32	26.8	$1.12 M_L + 17.60$	$1.04 M_L + 17.15$	0.0517
5	435	0.35	31.0	$1.16 M_L + 17.55$	$1.04 M_L + 17.18$	0.0516
6	420	0.36	33.5	$1.18 M_L + 17.53$	$1.05 M_L + 17.19$	0.0515

* Our "preferred model."

The trade-offs in the Pn results are illustrated in Table 2.5 with seven models that have data variances within 5%. All were done with the $r^{-1.3}$ spreading assumption. If the Q_{Lg} model is fixed, then the requirement that $S_0(Lg)/S_0(Pn)$ be range-independent places tight bounds on acceptable Q_{Pn} models. For example, in Figure 2.9 we plot long-period source ratios for Lg $Q_0 = 560$ and three Pn models with $Q_0 = 503$, 325, and 205. Only explosion ratios are plotted because the earthquake ratio is contaminated by unknown Pn radiation pattern effects. The ratios for the top and bottom models display a clear range dependence. The least squares straight line is plotted in each. The Pn model that minimizes the range dependence of the source ratio has $Q_0 = 325$. Thus, if Lg Q_0 is 560, the corresponding Pn Q_0 is 325, and
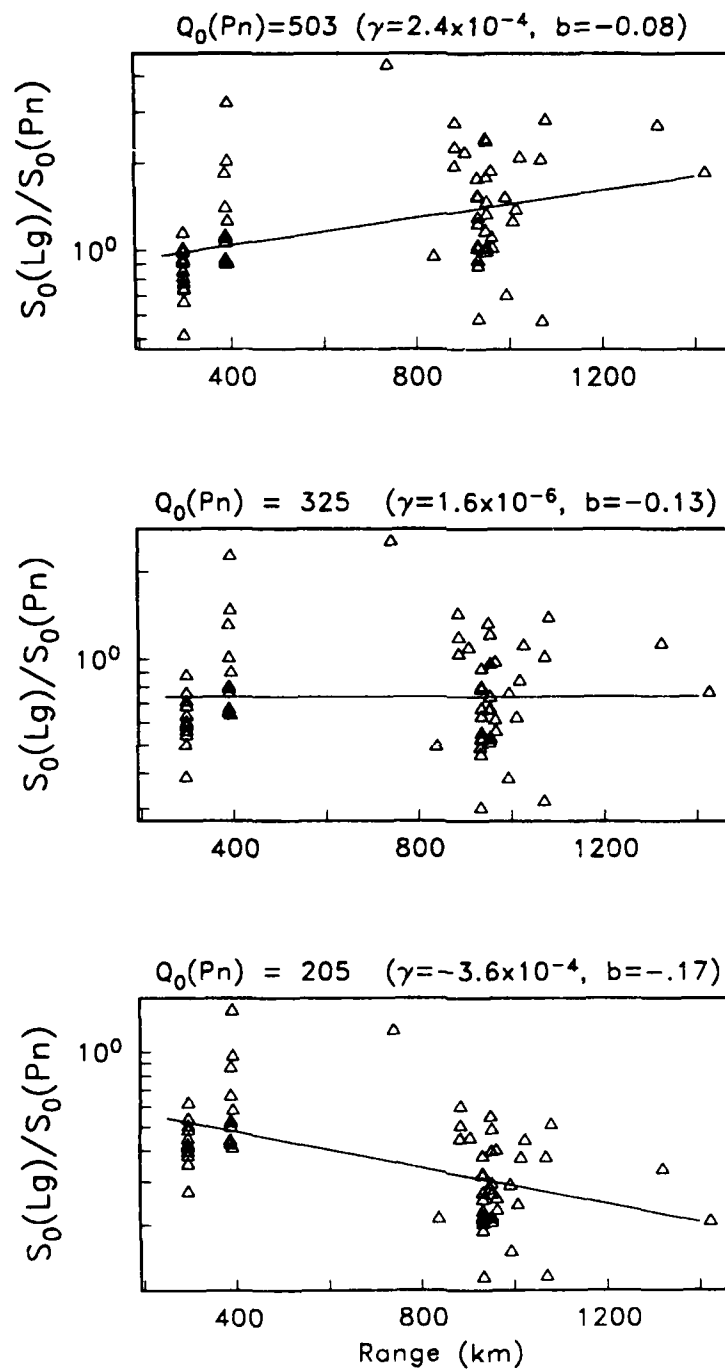
Figure 2.9. Ratio of *Lg* to *Pn* long-period explosion source levels from the inversion as a function of epicentral distance. *Lg* Q_0 is fixed for all three plots at 560 (model 2 of Table 2.4). *Pn* Q_0 is varied from 503 to 205 (models 1, 4, and 7 of Table 2.5). The slope and intercept of the log ratio are shown at the top of each plot.

these are the Q_0 for our "preferred models." The range-independent value of the source ratio is 0.74, which was used to estimate κ in (2.8).

Table 2.5 *Pn* parameter trade-off.

Model Index	Q_0	η	c	$\log M_o^{\text{exp}}$	σ_d^2
1	503	0.40	16.4	$0.97M_L + 17.65$	0.0912
2	402	0.44	20.9	$1.02M_L + 17.63$	0.0889
3	351	0.47	23.8	$1.06M_L + 17.61$	0.0881
4*	325	0.48	25.8	$1.08M_L + 17.59$	0.0877
5	292	0.51	28.3	$1.11M_L + 17.56$	0.0874
6	251	0.54	33.4	$1.17M_L + 17.51$	0.0870
7	205	0.59	42.5	$1.26M_L + 17.43$	0.0867

* Our "preferred model."

For different *Lg* Q_0, other *Pn* Q models are consistent with a range-independent S_0 ratio. For example, *Lg* Q_0 = 502 suggests *Pn* Q_0 = 280 and *Lg* Q_0 = 420 suggests *Pn* Q_0 = 225. There is no obvious basis for choosing among these model pairs. However, there is a trade-off between data variance and variance in the moment-magnitude relation. Figure 2.10a plots this trade-off for the full suite of *Pn* and *Lg* models.

Our primary goal is to define the range of models that provide a good fit to the data (i.e., reduce the data variance). Because the fit to the moment-magnitude relation depends on the similarity of our Q model to the RONAPP magnitude correction table, we place lower weight on reducing $\sigma^2_{M_o-M_L}$. Nevertheless, we can exclude models that offer little or no improvement in data variance at the cost of a large increase in moment-magnitude variance. The derivative of the trade-off curve (Figure 2.10b) at each iteration defines the relative weight given to the two variance measures for that model. All models with moment-magnitude variance greater than 0.095 increase $\sigma^2_{M_o-M_L}$ by an amount greater than 30 times the reduction in σ_d^2. Based on this, we consider only models with moment-magnitude variance less than 0.095 in the selection of our "preferred model." The *Lg* inversion produced nine models that all have moment-magnitude variance near 0.09. Of these, the model that produced the lowest data variance was selected as our "preferred model." However, we emphasize that all of these *Lg* models have Q_0 within 3% of our preferred model. Therefore, although the choice is subjective, the *Lg* Q_0 is insensitive to it. The "preferred" *Pn* model is chosen by requiring the $S_0(Lg)/S_0(Pn)$ ratio to be range-independent. Based on this, our "preferred models" are Q_0 = 560 and η = 0.26 for *Lg* and Q_0 = 325 and η = 0.48 for *Pn*.

Source assumptions. All of the results of this study were obtained using a source function that decays as f^{-2} beyond a corner frequency that is inversely proportional to the cube root of the long period level. However, most of the events considered have local magnitudes
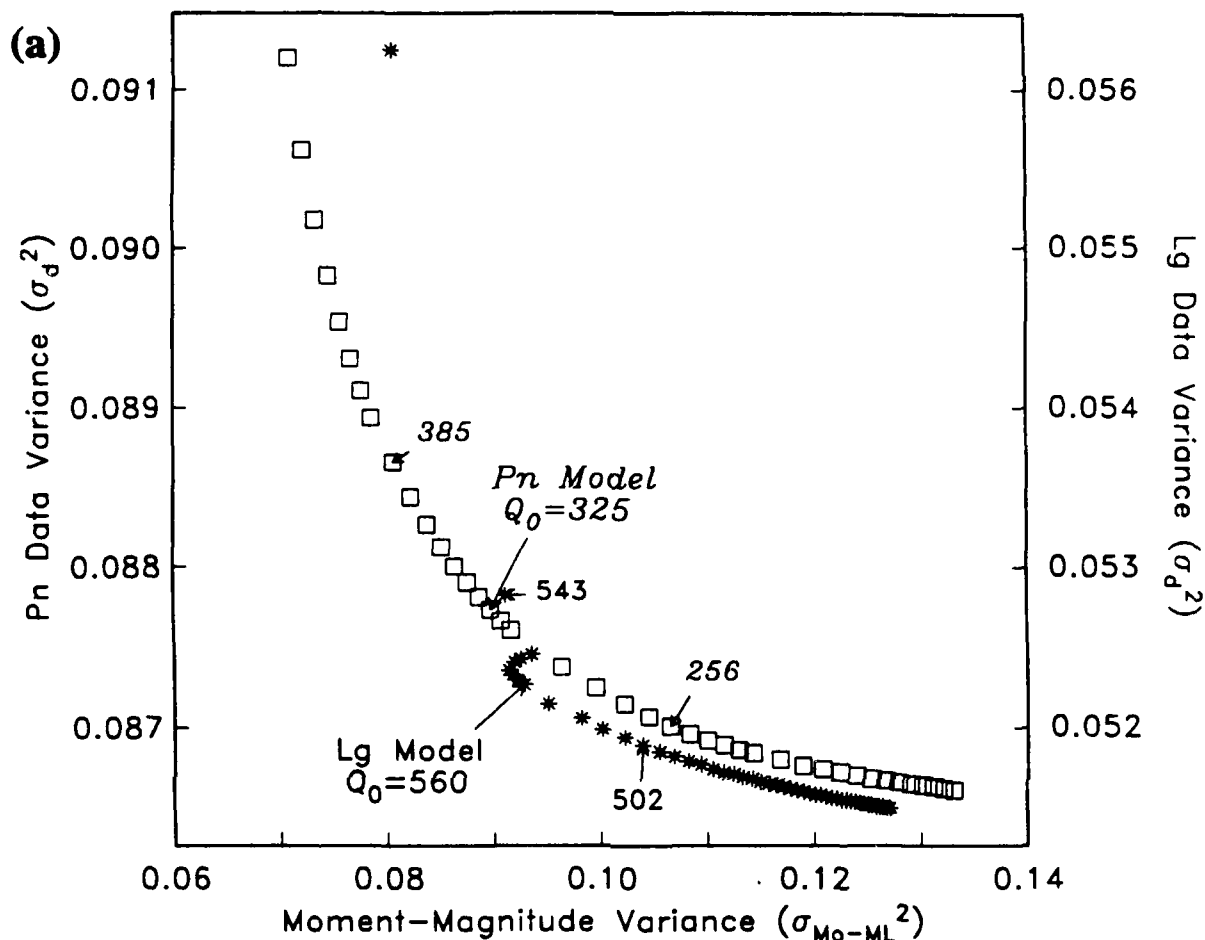
32

Figure 2.10. (a) Trade-off between data variance (σ_d^2) and variance of the moment-magnitude relation for *Pn* (squares) and *Lg* (asterisks). Symbols define models for different iterations of the inversion. Three of the *Pn* and *Lg* models are labeled by their Q_0 values. The *Lg* data variance scale is shown on the right, and the *Pn* scale is on the left. The "preferred" *Pn* and *Lg* models are identified. (b) The derivatives of the trade-off curves in Figure 2.10a.
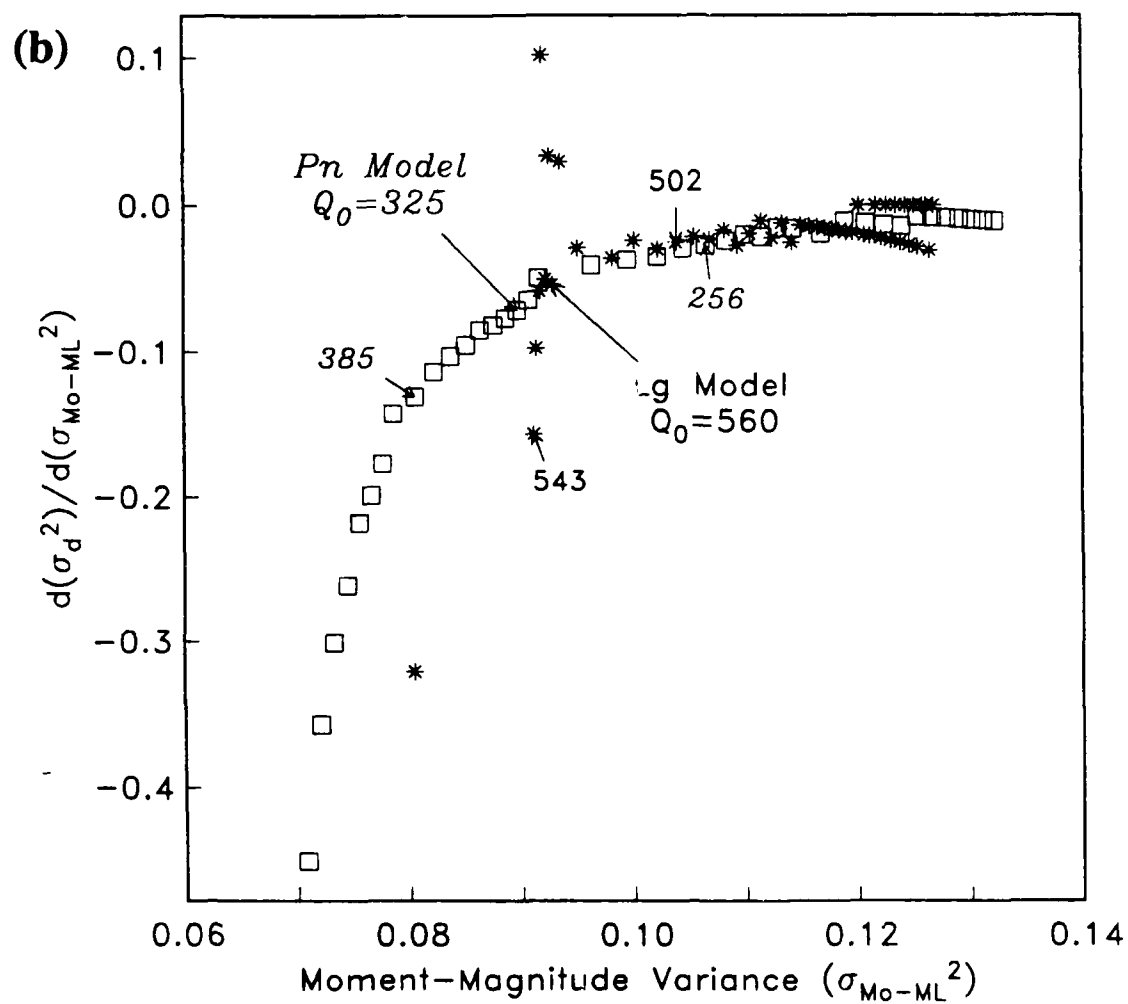
(b)

Figure 2.10. (Continued).

less than 3.0, so the corner frequencies are near or beyond the upper end of the frequency band inverted. The results are therefore not very sensitive to our source parameterization.

All of the results discussed previously were obtained using the simplified *Mueller and Murphy* [1971] explosion source function (2). We also inverted the *Lg* data assuming a *Brune* [1970] earthquake source model with cube root corner frequency scaling. For the same Q_0, the Brune source model leads to Q with slightly stronger frequency dependence. The reason for this difference is that the Brune model has a less abrupt corner frequency, and the reduced high-frequency source contribution is compensated for by a higher Q at high frequency. If we assume a flat source (no corner frequency), the results for *Lg* are nearly the same as those from the *Mueller and Murphy* [1971] model, with a slight increase in the data variance. In other words, the assumed character of the source above the corner frequency has little influence on the results. This merely reflects the fact that the corner frequencies are greater than 7 Hz for most of the events. We have not explored other alternative models for the source but are confident that the *Lg* attenuation results are not sensitive to the details of the source parameterization.

The *Pn* inversion is more sensitive to the source parameterization due to radiation pattern effects and the increased bandwidth of the data. We used the *Mueller and Murphy* [1971] model for all *Pn* inversions and expect similar results for other source models with f^{-2} high-frequency decay. It is obvious that an assumed source model with faster decay above the corner frequency would result in a model with a higher Q to preserve the fit at high frequency. Our results for *Pn* must therefore be considered relative to our assumption that the source has f^{-2} high-frequency falloff.

Geometric spreading assumptions. Assuming *Lg* is an Airy phase, its geometric spreading in the time domain is $r^{-5/6}$ [*Nuttli*, 1973]. For time windows long enough to include the entire dispersed wave train, the frequency domain spreading rate is $r^{-1/2}$ [*Street et al.*, 1975; *Herrmann and Kijko*, 1983]. We have approximated *Lg* geometric spreading using (8) with r_0 = 100 km and $m = 1/2$. All of the data used in this study are at ranges greater than 100 km. Therefore r_0 in (8) trades off directly with inverted moment and has no effect on the $Q_{Lg}(f)$ estimate.

The geometric spreading rate of *Pn* is difficult to estimate with confidence. So far, we have assumed $r^{-1.3}$ *Pn* spreading. In this section, we examine the results for the alternative assumptions, r^{-1} (spherical spreading) and $r^{-1.5}$. Table 2.6 describes the resulting *Pn* models. All are required to give a range-independent $S_0(Lg)/S_0(Pn)$ ratio for our "preferred" *Lg* Q model (model 2 in Table 2.4). As the *Pn* spreading rate increases, $Q_0(Pn)$ increases, η decreases, and M_0 increases. The range-independent value of the long-period source level ratio can be used to extract the relative *Lg* excitation of explosions and earthquakes (see equation (2.8)). The κ in Table 2.6 indicates the relative excitation of *Lg* for explosions and earthquakes. For r^{-1} *Pn* spreading κ > 1, which means that *Lg* for explosions is greater than for earthquakes of equal moment. This contradicts empirical observations and therefore indicates that the *Pn* spreading rate is greater than r^{-1}. On the other hand, a *Pn* spreading rate of $r^{-1.5}$ gives κ = 0.10, or 10 times greater *Lg* for earthquakes than explosions. This factor seems too large to be consistent with observations (for a review, see *Pomeroy et al.*, [1982]). However, the factor of 4 resulting from the $r^{-1.3}$ *Pn* spreading assumption is consistent with the empirical

observations. Also, $r^{-1.3}$ spreading is consistent with theoretical simulations of Pn propagation in realistic Earth models (T. C. Wallace, personal communication, 1987).

Table 2.6 Pn parameter trade-off as a function of spreading rate.

Spreading Rate	Q_0	η	c	$\log M_o^{exp}$	κ	σ_d^2
r^{-1}	243	0.55	17.3	$1.08 M_L + 16.93$	1.25	0.0868
$r^{-1.3}$	325	0.48	25.8	$1.08 M_L + 17.59$	0.27	0.0874
$r^{-1.5}$	409	0.44	32.4	$1.08 M_L + 18.01$	0.10	0.0890

2.9 Q for FTL and FGV spectra

Spectra computed for a fixed group velocity window may be different from those computed for a fixed time length. If the time window is not long enough to include the entire dispersed wave train, then the apparent attenuation will exceed that of combined anelastic absorption and geometric spreading. That is, loss of energy from the low group velocity modes as distance increases can introduce a bias in the Q estimated from spectra computed for a fixed time length. For example, Figure 2.11 displays vertical component recordings of a western USSR mine blast (event 44, Table 2.1). The length of the FGV window for this range is 52 s. It is obvious that neither 5- nor 17-s windows include all of the Lg energy at this distance. More importantly, spectra computed for a fixed time window that is sufficient to include the entire Lg wave train at long ranges will include much more noise at short ranges than spectra computed for a fixed group velocity window. In this section we determine the severity of the bias in $Q_{Lg}(f)$ introduced by using short time windows. We have chosen a 17-s window for comparison because this is a common window length used in other studies of Lg attenuation [*Hasegawa*, 1985; *Shin and Herrmann*, 1986; *Chun et al.*, 1987].

Table 2.7 lists our "preferred" $Q_{Lg}(f)$ values for the three time windows. The corresponding Pn models (those that produce a range-independent S_0 ratio) are also listed. Because the Pn models do not differ significantly, the Lg models can be compared directly. The difference between the FGV and FTL spectra is range-dependent. Therefore, the inversion results differ in the Q estimate rather than in the derived moments. Thus, all three Q models give approximately the same relationship between moment and local magnitude.

Table 2.7 Lg Inversion results for various time windows.

Lg Time Window	$Q_{Lg}(f)$		$Q_{Pn(f)}$		$\log M_o^{eq}$
	Q_0	η	Q_0	η	
FTL (5-s)	350	0.41	300	0.49	$1.04M_L + 17.10$
FTL (17-s)	470	0.32	335	0.48	$1.02M_L + 17.18$
FGV (3.6-3.0 km/s)	560	0.26	325	0.48	$1.03M_L + 17.10$

Figure 2.12 compares $\exp(-\pi f t/Q(f))$ at 300 and 1000 km for the $Q_{Lg}(f)$ models listed in Table 2.7. We interpret the large difference between the results for the 5-s and FGV windows as an indication that the short time window Q is biased by the exclusion of low group velocity modes. The 17-s window produces a result very similar to the FGV window at 300 km (the FGV window length is about 17 s at that distance), however the spectra are significantly different at longer ranges.

In a similar study, *Chun et al.* [1987] estimated vertical component Lg attenuation using both fixed window lengths and fixed group velocity windows on the same data set. Using Lg data from the Eastern Canada Telemetered Network (ECTN), they found $Q(f) = 800f^{0.26}$ for a fixed time window of 17.07 s. For a fixed group velocity window of 3.61-2.6 km/s, they
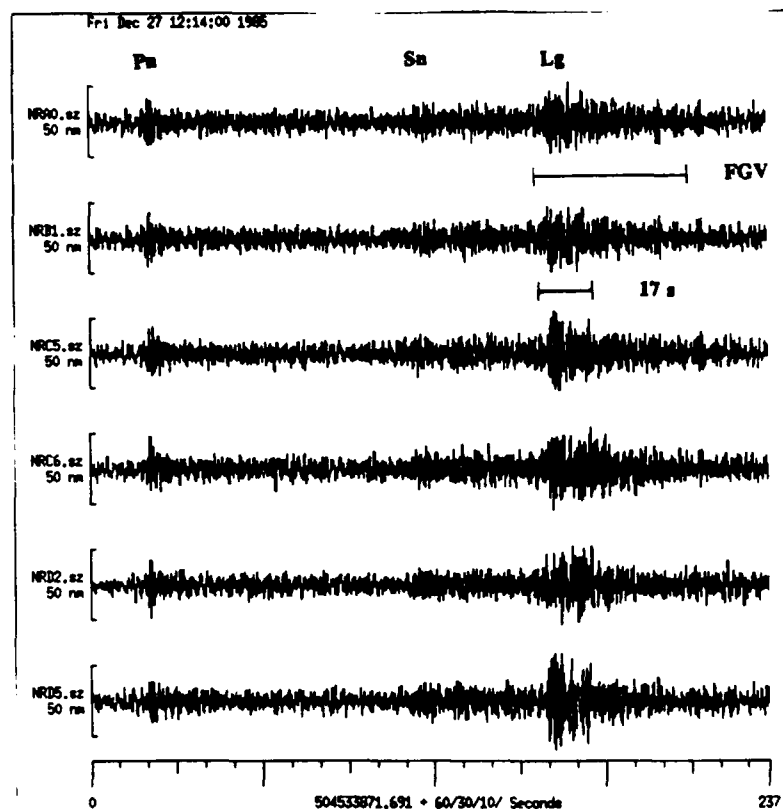
37

E8 Mine Blast (Event 44)

Figure 2.11. Vertical component recordings of an E8 mine blast recorded at six stations within the NORESS array. The *Pn*, *Sn*, and *Lg* phases are labeled on the top trace. The event magnitude is 3.3 and the range is 950 km. Window lengths of 17 s and 52 s (FGV window) are indicated for *Lg*.
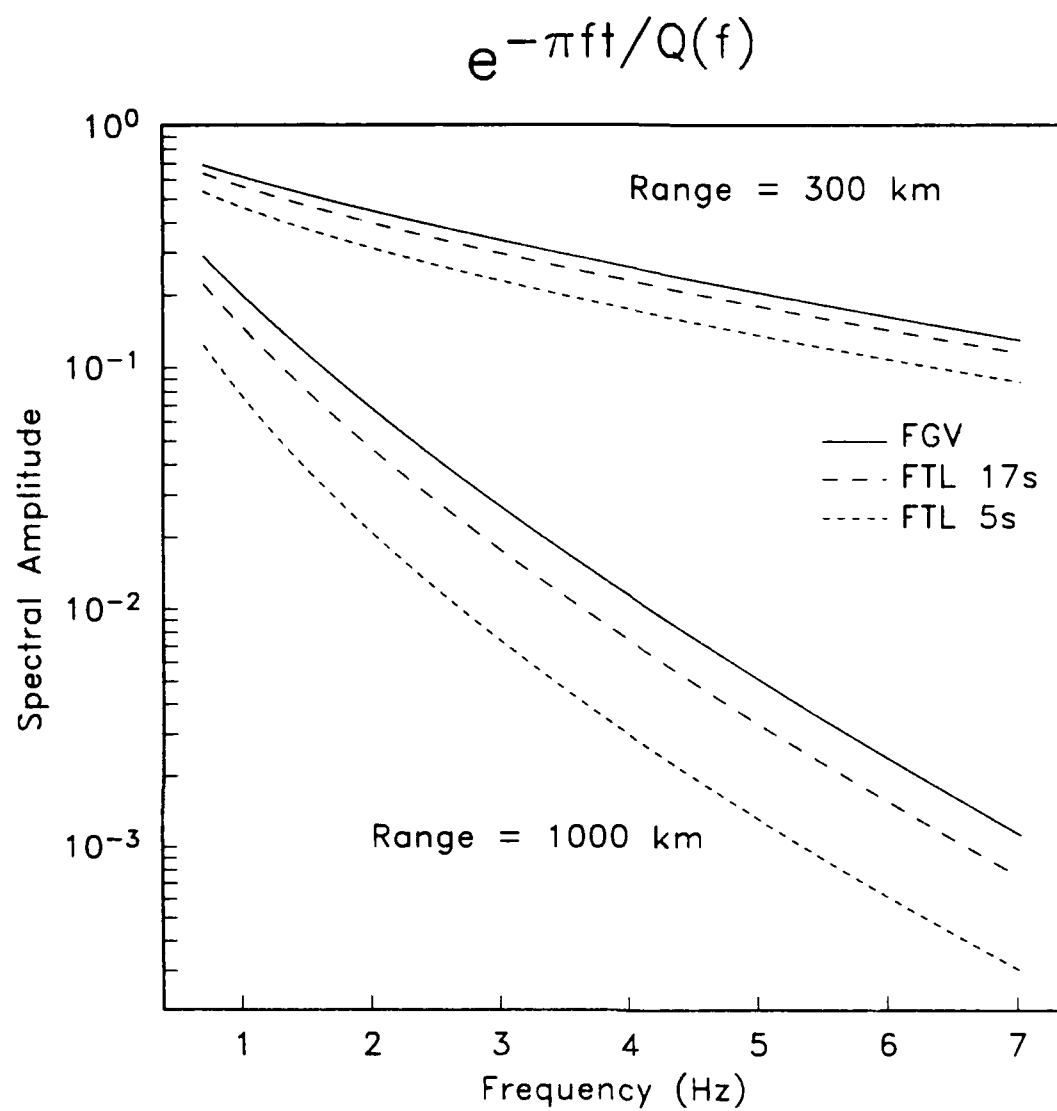
$$e^{-\pi ft/Q(f)}$$

Figure 2.12. Comparison of $\exp[-\pi ft/Q(f)]$ at 300 and 1000 km for the Q models obtained from the inversion of Lg spectra computed for 5-s, 17-s, and FGV windows.

found $Q(f) = 1100f^{0.19}$. Their data spanned distances of 90-867 km, so the time windows varied from 9.7 s to 93 s. Their results are generally consistent with ours (Table 2.7) although their fixed group velocity range was considerably larger.

2.10 Simulation of regional wave spectra

At the simplest level, we can view our results as an accurate parameterization of the observed spectra of regional events recorded at NORESS in terms of familiar seismological parameters characterizing the source and range dependence of these spectra. Using these parameters, we can "predict" the spectra for a chosen source and range and be confident that it is correct within the well-defined uncertainty of our parameters. Our confidence, of course, degrades if we choose a source or range outside the bounds of our experience, that is, if we attempt to extrapolate our results to situations not yet encountered.

Figure 2.13 displays predicted range-dependent Pn spectra, based on the inversion results, for a magnitude 3.0 explosion. The relevant parameters are $Q(f) = 325f^{0.48}$, $M_o = 6.8 \times 10^{20}$ dyn-cm ($S_0 = 17.2$), $f_c = 10.0$ Hz, and a spreading rate of $r^{-1.3}$. Note that these predicted spectra do not depend on this particular resolution of the parameter trade-offs; all models that produce essentially the same data variance give similar predictions. The Pn spectra approximately parallel the noise curve at a distance of 400–500 km, converging with it at longer ranges and diverging from it at shorter ranges. This behavior is also seen in average spectral density curves constructed by *Ringdal et al.* [1986] using the high-frequency element of the NORESS array.

Since our results accurately represent the observed Pn attenuation in this part of northern Europe, it is interesting to compare them to the attenuation results used by *Evernden et al.* [1986] to estimate P detection capability in the Soviet Union. Their estimates of Pn attenuation in tectonically stable areas in the Soviet Union are based primarily on 1–3 Hz amplitude data from paths in the eastern United States. They find that these data are consistent with a Pn spreading rate of r^{-2} and a constant Q_α of 9000. The only high-frequency data they cite to corroborate this estimate is a single Pn spectrum recorded at a range of 190 km. At such short distances, a large suite of Q models can predict the shape of the Pn spectrum, as acknowledged by *Evernden et al.* [1986], who note that the frequency-dependent model $Q(f) = 300f^{0.4}$ fits this spectrum as well as their $Q = 9000$ estimate. It happens that this frequency-dependent model is very similar to our NORESS model. *Evernden et al.* [1986, p.156] reject such a frequency-dependent Q model because "... a Q_0 value of about 300 introduces a sixfold departure of 1-Hz Pn amplitudes from a r^{-2} power law of distance between 150 and 2000 km." But this departure is a direct consequence of their assumption that Pn is a canonical head wave with r^{-2} geometric spreading. Our Q model combined with $r^{-1.3}$ geometric spreading gives Pn amplitude decay that does not deviate significantly from the r^{-2} amplitude falloff at 1 Hz that is commonly observed.

Figure 2.14 compares theoretical Pn spectra computed using the attenuation model of *Evernden et al.* [1986] to those computed with our results for an $M_L = 3.0$ explosion at ranges of 200, 500, and 1000 km. Flat source spectra were assumed. Therefore these curves provide upper bounds on the expected high-frequency content of Pn. While the two models yield
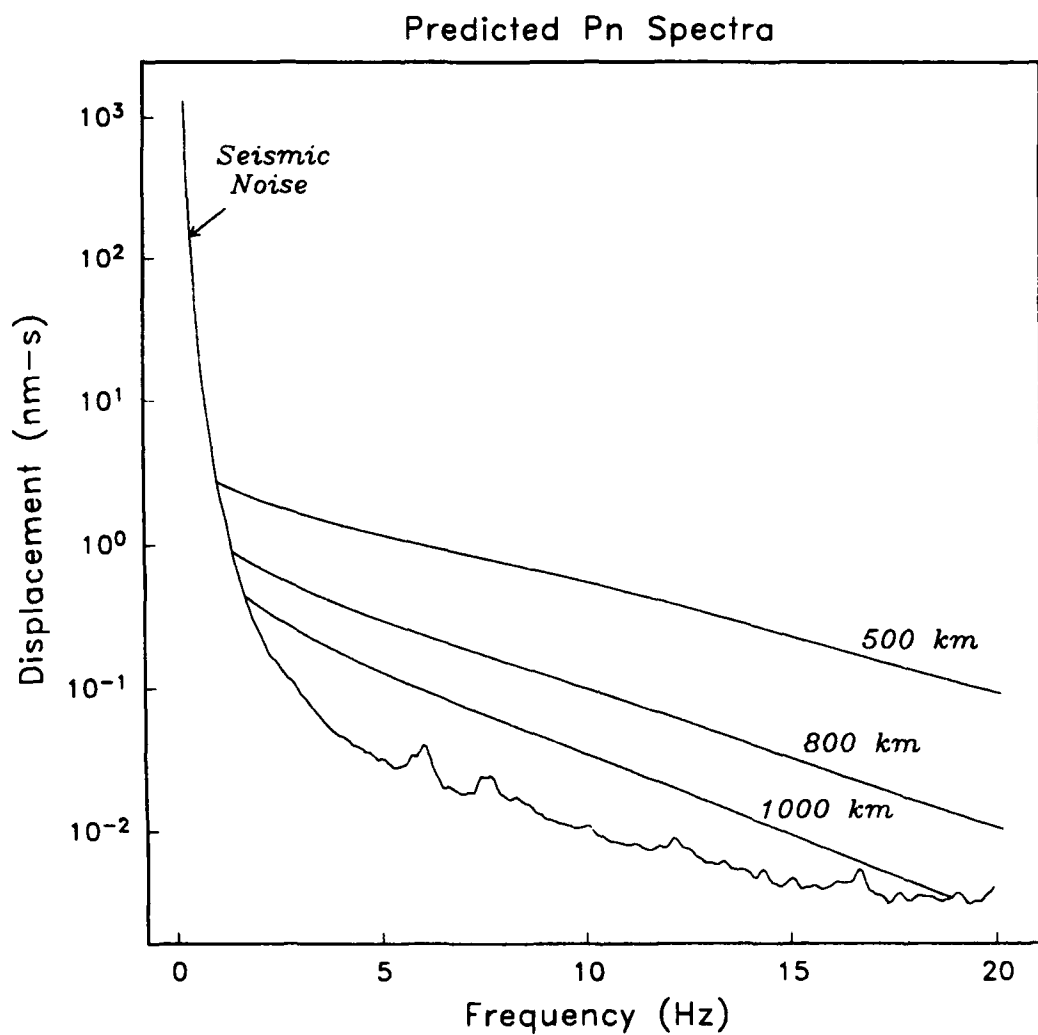
Predicted Pn Spectra

Figure 2.13. Predicted NORESS *Pn* displacement spectra at three epicentral distances for a magnitude 3.0 explosion, based on the inversion results. The average NORESS noise was estimated from samples taken prior to *Pn* for many events [*Henson and Bache*, 1988].
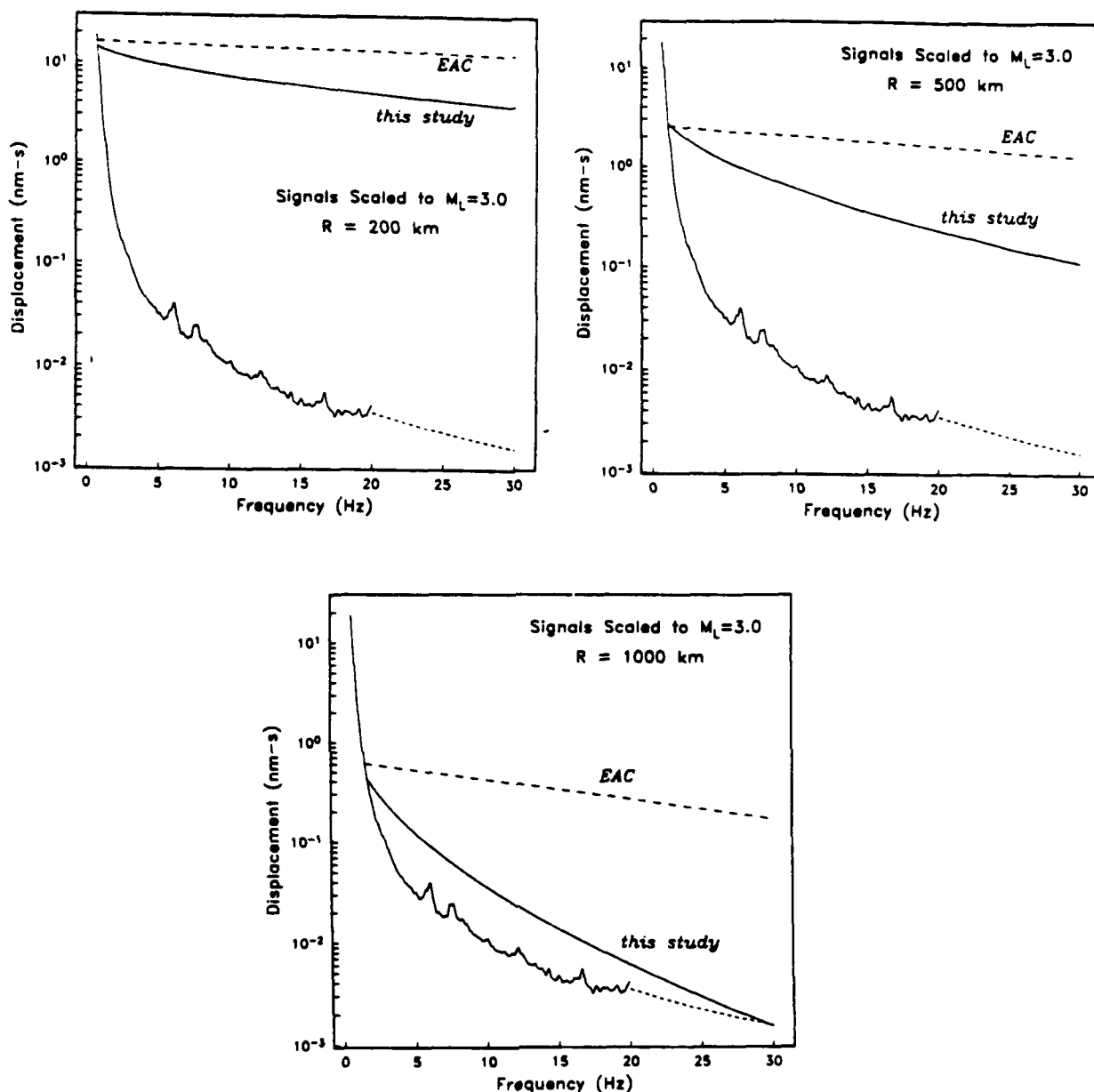
41

Figure 2.14. Predicted range-dependent *Pn* spectra, based on the *Evernden et al.* [1986] attenuation model (EAC) and the one presented in this study for a magnitude 3.0 explosion at 200, 500, and 1000 km. The EAC curve is scaled such that it equals ours at 1 Hz and 1000 km (equal m_b at 1000 km). The bottom curve in each diagram represents average NORESS noise. The noise curve is extrapolated beyond 20 Hz assuming f^{-2} falloff. All plots are for flat source spectra.

similar results for total attenuation (spreading and anelasticity) at 1 Hz, they suggest very different conclusions about the *Pn* detection capability at high frequency. For example, our model predicts the maximum signal/noise at slightly higher than 5 Hz for *Pn* at 1000 km, while the maximum signal/noise frequency for the *Evernden et al.* [1986] model is only bounded by source corner frequency. Since our model accurately represents the NORESS data, Figure 2.14 demonstrates that the results of *Evernden et al.* [1986] vastly overestimate observed NORESS *Pn* amplitudes for frequencies above a few hertz and distances greater than a few hundred kilometers. At 1000 km the *Evernden et al.* [1986] Q model overestimates the average observed 15 Hz *Pn* amplitude at NORESS by a factor of 25. Thus the major conclusion of *Evernden et al.* [1986] that detection capability would be enhanced at high frequency (> 20 Hz) is not supported by the NORESS observations. This conclusion is independent of assumptions about the source corner frequency or high-frequency falloff rate. That is, if the upper mantle structure of the Russian platform is at all similar to Scandinavia, regional network capability simulations produced by *Evernden et al.* [1986] are far too optimistic.

The capability to detect *Lg* is not accurately represented by spectra computed with fixed group velocity windows. Such spectra include energy distributed in time, while signal detection is based on amplitudes in the time domain on filtered beams. In Section 4 we show that spectra computed with short time windows at the detection time are more appropriate for estimating *Lg* detection capability. Such spectra are computed by the automated signal processing program SAIAP for 5-s windows. The Q_{Lg} resulting from the inversion of these spectra has $Q_0 = 350$ and $\eta = 0.41$ [*Sereno et al.*, 1987]. Figure 2.15 displays theoretical *Lg* spectra for the 5-s windows for an $M_L = 3.0$ explosion at ranges of 500, 800, and 1000 km. The relevant parameters are $Q(f) = 350f^{0.41}$, $M_o = 9.8 \times 10^{20}$ dyn cm ($S_0 = 20.7$), $f_c = 10.4$ Hz, and cylindrical spreading with $r_0 = 100$ km. The pre-*Pn* noise spectrum is plotted only for comparison to Figure 2.13. These are the relevant *Lg* spectra for estimating detection capability but must be referenced to pre-*Lg* noise spectra which are complicated to describe in a simple way. Here we simply note that the *Lg* spectrum reaches the noise level at a much lower frequency than the *Pn* spectrum, while at long periods the *Lg* amplitude exceeds the *Pn* amplitude by as much as a factor of 10. This is consistent with the well-known observation that regional seismograms are characterized by *Lg* being the largest-amplitude phase and *Pn* having a higher dominant frequency.

The uncertainty in the "predicted" spectra in Figures 2.13 and 2.15 is a combination of the uncertainty in the moment-magnitude relation and the uncertainty in the spectral estimate for fixed moment. Combining variances for these two contributions, we compute the standard deviation for our spectral estimate. This is illustrated in Figure 2.16 with the predicted *Pn* spectrum at 800 km from a magnitude 3.0 explosion. The uncertainty is larger for earthquakes due to radiation pattern effects. While the *Lg* spectral estimate has lower variance for fixed moment, the variance of the *Lg* explosion moment-magnitude relation is larger. The result is that the standard error in our predicted *Lg* spectra is about the same as the error for *Pn* illustrated in Figure 2.16.
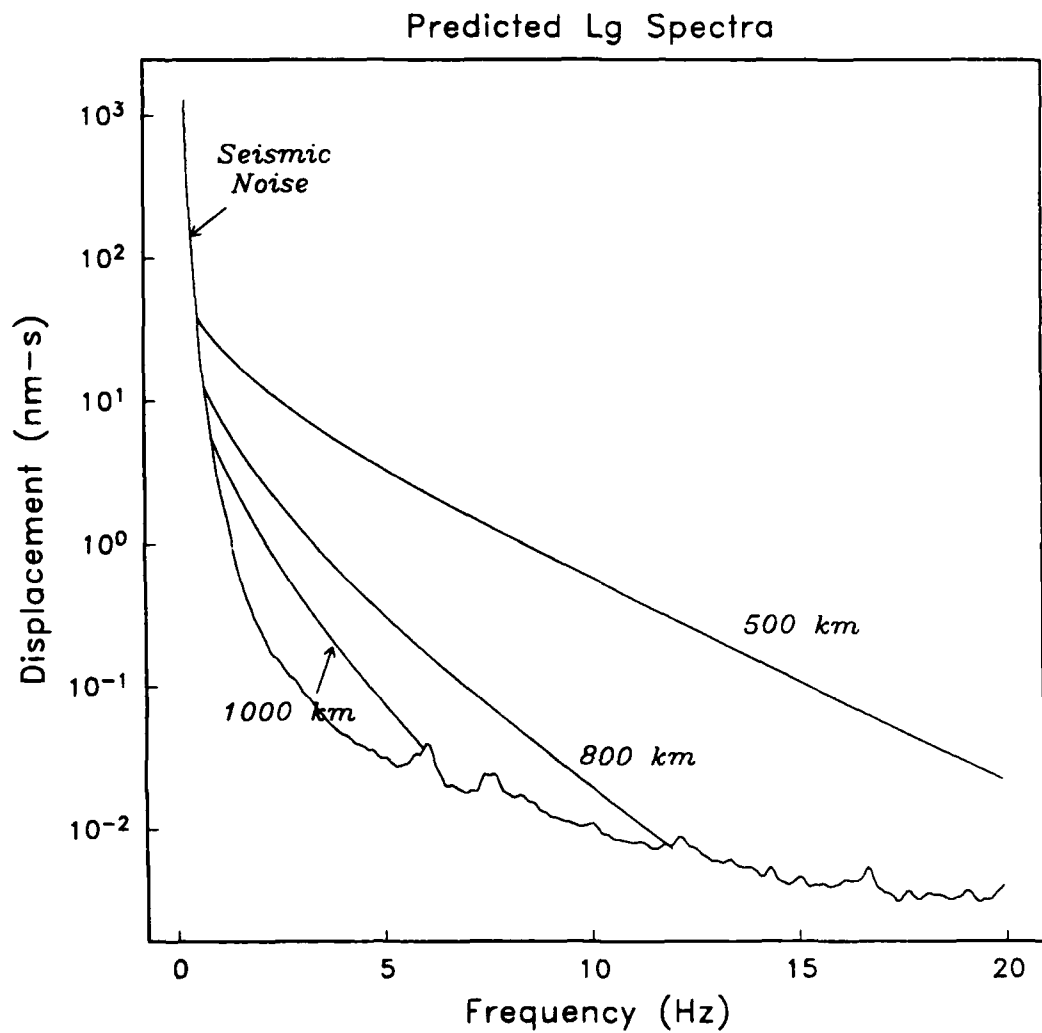
43

Figure 2.15. Predicted NORESS *Lg* displacement spectra at three epicentral distances for a magnitude 3.0 explosion, based on the inversion of *Lg* spectra computed for fixed 5-s windows. The average NORESS noise was estimated from samples taken prior to *Pn* for many events [*Henson and Bache*, 1988].
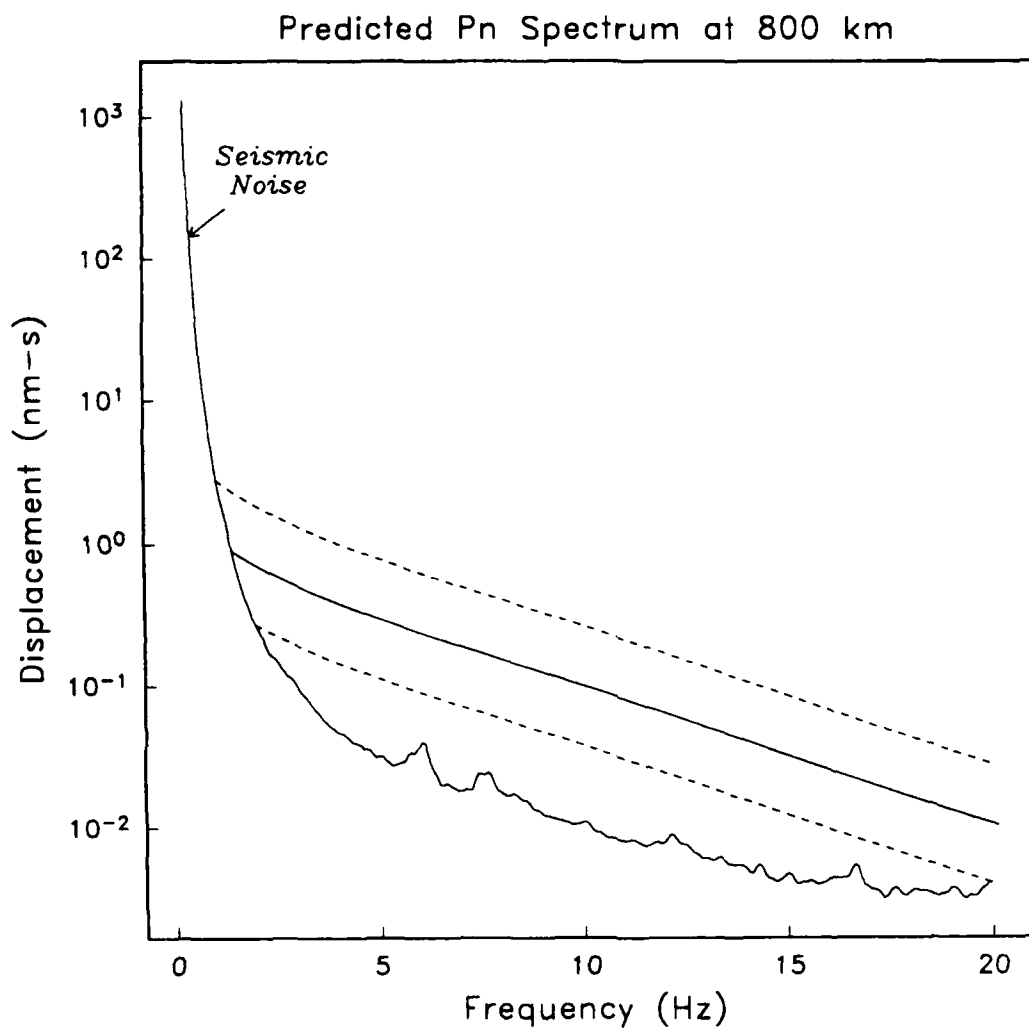
44

Predicted Pn Spectrum at 800 km

Figure 2.16. Predicted NORESS *Pn* displacement spectrum at 800 km for a magnitude 3.0 explosion, based on the inversion results. The dashed curves indicate one standard deviation uncertainty in the estimate. The average NORESS noise was estimated from samples taken prior to *Pn* for many events [*Henson and Bache,* 1988].

3. NOISE LEVELS FOR SECONDARY PHASES

Section 2 discussed Lg attenuation results obtained from the inversion of spectra over a 1 to 7 Hz band. Results for fixed group velocity and fixed time length spectra were compared. However, the inversion bandwidth was based on signal to pre-Pn (or ambient) noise. In fact, the appropriate noise spectrum to use is the pre-Lg or Sn coda spectrum. Sn is a higher frequency phase than Lg and therefore it is possible that our Q_{Lg} results are contaminated at high frequency by the presence of Sn coda [*Ringdal*, 1986; *Chun, et al.*, 1987; *Shin and Herrmann*, 1987]. For example, *Shin and Herrmann* [1987] found that for distances greater than about 600 km, Lg is dominated by coda arrivals above 7 Hz. In this section we compare Lg and pre-Lg spectra to determine the frequency at which Sn coda can be expected to influence the Lg attenuation estimate. The bias in $Q_{Lg}(f)$ is estimated by inverting a lower-frequency band over which we assume Sn coda does not affect the Lg spectra.

3.1 Pre-Lg spectra and Sn coda contamination

Predicting the Lg detection capability of a small regional network depends not only on a parameterization of Lg spectra, but also on a parameterization of Sn coda spectra. That is, even in the event that our Q results are not significantly biased by Sn coda, the detection capability must be based on a comparison of Lg signal to pre-Lg noise. However, Sn coda amplitude is a complicated function of magnitude, distance, azimuth, etc. In this section, we compare Lg, pre-Lg, and ambient noise spectra. In Section 4, we determine an empirical time-domain detection capability curve that accounts for Sn coda amplitudes.

We computed pre-Pn, pre-Lg, and Lg spectra for the 24 events listed in Table 3.1. The event locations are plotted in Figure 3.1. These events are a subset of the explosion data set used in the inversion. Only explosions were used because they have precise locations. Explosions were selected that covered a broad distance range to NORESS. The Lg spectra were computed for fixed 5-s windows starting 0.3 s before the automatic detection time (as described in the previous section). The pre-Lg spectra were computed in the same way with the onset taken 5.6 s prior to the Lg detection time. The pre-Pn spectra were computed for a 5-s window taken prior to the first P detection.

Figure 3.2 plots the frequency at which the Lg and pre-Lg spectra merge as a function of epicentral distance. In general, Lg spectra are contaminated by Sn coda for frequencies beyond about 10 Hz at distances between 300 and 400 km and beyond 3-6 Hz for distances greater than 700 km. Superimposed on Figure 3.2 are representative short and long range spectra. The top curve in each plot is the Lg spectrum, the dashed curve is pre-Lg and the bottom curve is the pre-Pn (ambient noise) spectrum. Based on typical coda decay rates, one might expect that Sn coda contamination would be more important at short ranges. However, the rate of decay of the Lg spectrum increases more rapidly with distance than does the rate of decay of the Sn spectrum (i.e., the apparent $Q_{Lg} < Q_{Sn}$). Thus, although the low frequency Lg to pre-Lg ratio is greater at large distances, the two curves merge at a lower frequency at long ranges than at short ranges. Since more than half of the events used in the 1-7 Hz inversion described

Table 3.1. Events used for secondary phase noise level analysis.

| Event	Date	Time	Location	Type	M_L
1	4-30-86	10:19	59.31N 6.95E	EX-BLA	2.2
2	8-14-86	14:40	59.31N 6.95E	EX-BLA	2.4
3	9- 9-86	17:56	59.31N 6.95E	EX-BLA	2.4
4	1-31-86	14:18	58.34N 6.43E	EX-TIT	1.9
5	7-31-86	15:06	59.40N 24.60E	EX-E2	3.0
6	8-13-86	15:32	67.10N 20.60E	EX-R1	2.6
7	7-16-86	11:27	59.30N 27.20E	EX-E4	3.0
8	3-24-86	11:18	59.30N 27.20E	EX-E4	2.5
9	7-18-86	13:42	59.30N 27.60E	EX-E6	3.0
10	7- 1-86	15:28	60.70N 28.70E	EX-V12	2.7
11	3-10-86	12:02	59.30N 28.10E	EX-E7	3.2
12	3-13-86	11:39	60.70N 29.00E	EX-V5	2.9
13	3-27-86	12:24	59.40N 28.50E	EX-E8	3.5
14	12-10-85	12:18	60.60N 29.20E	EX-V11	2.0
15	7-23-86	13:10	60.80N 29.30E	EX-V1B	2.8
16	7-14-86	14:30	61.10N 29.90E	EX-V8	3.2
17	4-19-86	10:59	61.10N 30.20E	EX-V2	2.5
18	6- 4-86	9:07	61.50N 30.40E	EX-V3	3.9
19	1- 3-86	14:59	61.90N 30.60E	EX-V7	2.9
20	2 -7-86	11:00	64.70N 30.70E	EX-V10	3.1
21	2-18-86	12:46	64.70N 30.70E	EX-V10	2.6
22	6-25-86	12:33	61.40N 31.60E	EX-V4	2.9
23	2-23-86	6:14	67.60N 34.00E	EX-K2	3.1
24	7-14-86	15:02	69.30N 34.40E	EX-K9	3.1
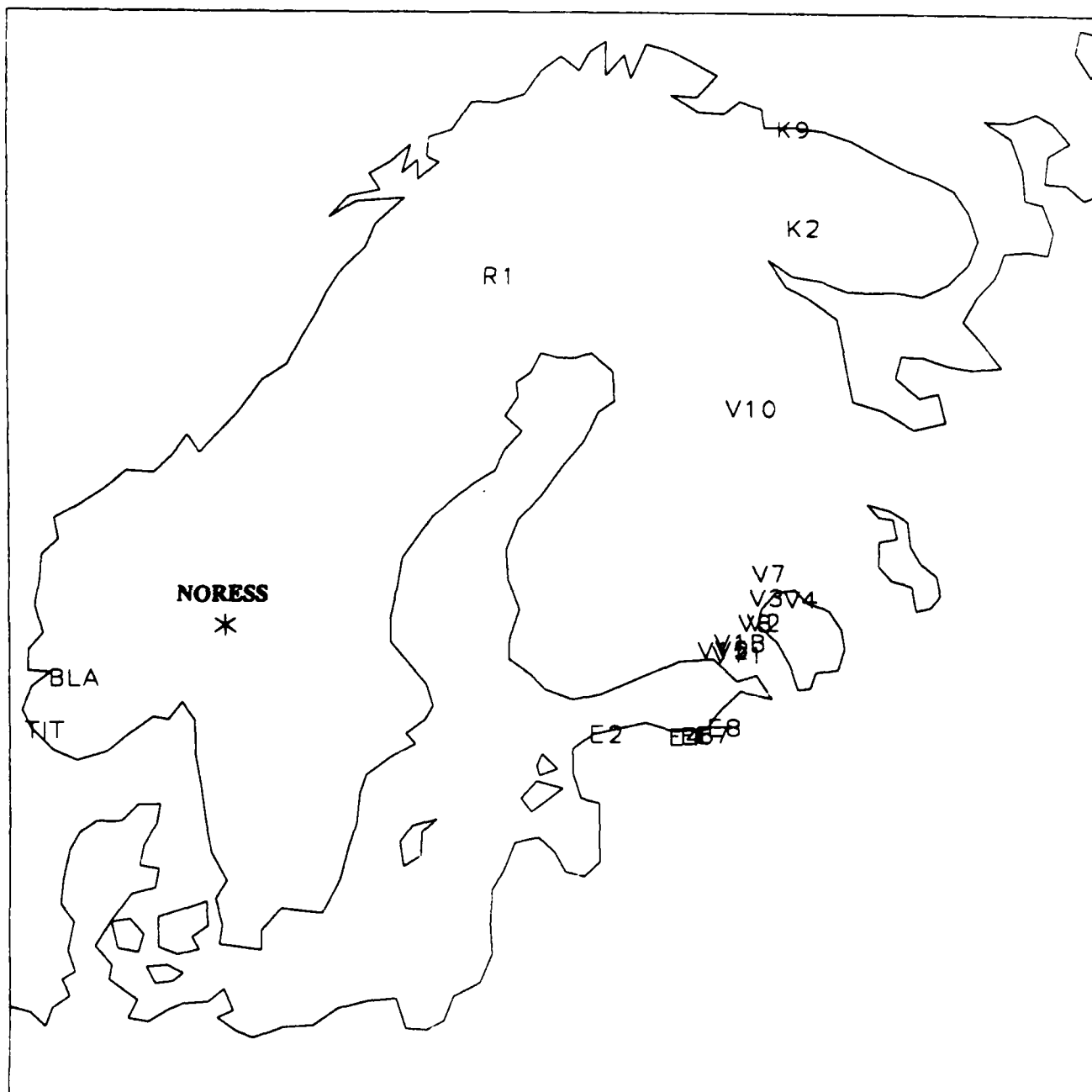
Figure 3.1. Map of the mine locations for explosions used to compute pre-Lg spectra. The events are listed in Table 3.1.
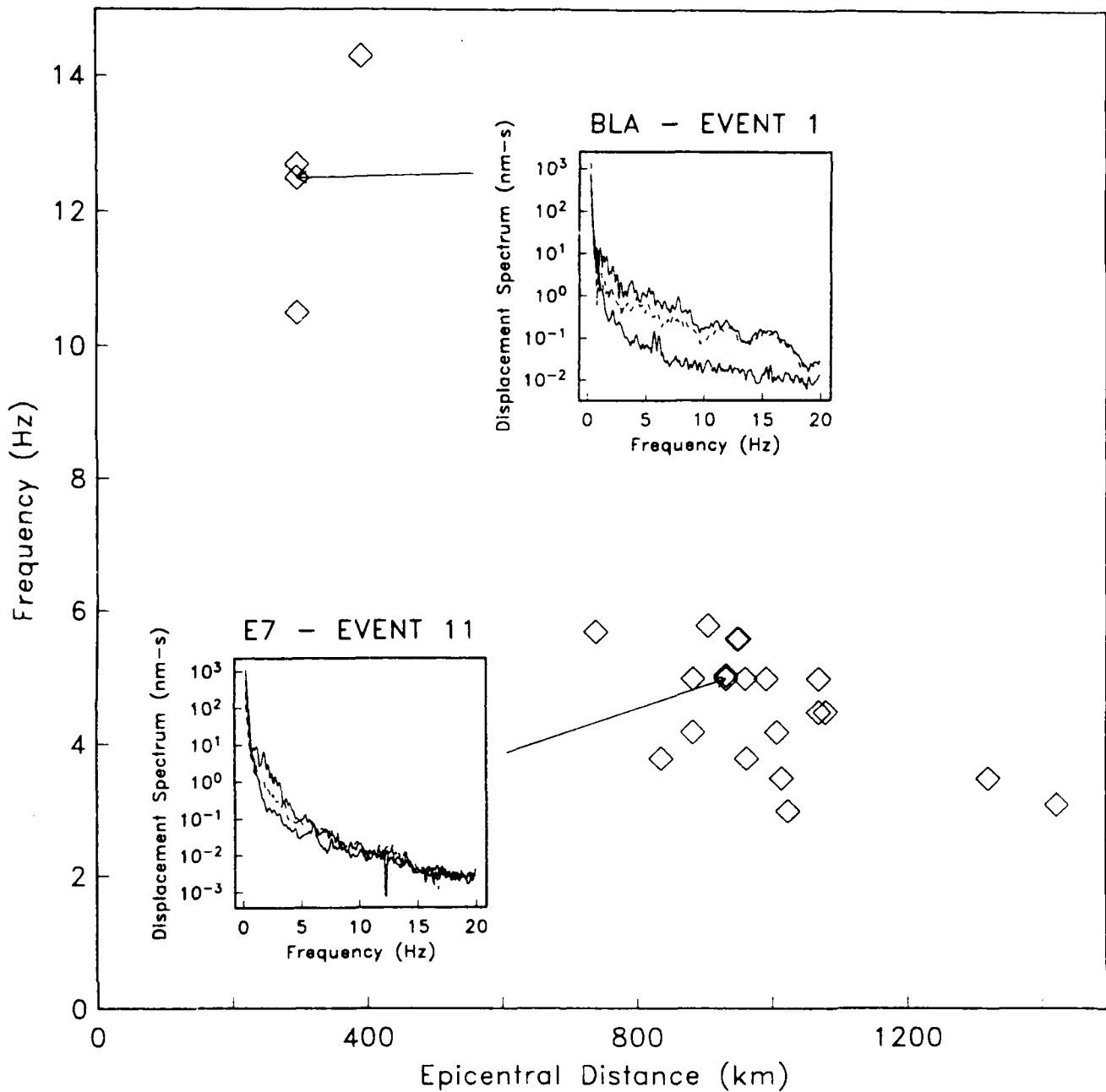
Figure 3.2. Frequency at which the *Lg* and pre-*Lg* spectra merge as a function of epicentral distance for the 24 events listed in Table 3.1. Representative short and long range spectra are plotted as insets. The top curve is the *Lg* spectrum, the dashed curve is the pre-*Lg* spectrum, and the lower curve is the pre-*Pn* noise. *Sn* coda contaminates the *Lg* spectrum above about 10 Hz at 400 km and above 3-6 Hz at 1000 km.

in Section 2 were at distances greater than 400 km, it is likely that the Lg Q results are affected by Sn.

3.2 Inversion results

From Figure 3.2, we expect our $Q_{Lg}(f)$ to be affected by Sn coda beyond about 3 Hz. To estimate this effect we inverted the FGV Lg spectra over 1-3, 1-5, and 1-7 Hz bands. Assuming that Sn coda does not significantly alter the Lg spectrum at frequencies less than 3 Hz, the difference between Q estimated over 1-3 and 1-7 Hz provides an upper bound on the bias due to Sn coda. Table 3.2 lists the inversion results for the different frequency bands.

Table 3.2 Lg inversion results over several frequency bands.

Frequency Band	Q_0	η	$\log M_o^{exp}$ ($\kappa = 0.27$)	σ_d^2
1–3 Hz	582	0.18	$1.05M_L + 17.70$	0.0555
1–5 Hz	561	0.24	$1.05M_L + 17.69$	0.0569
1–7 Hz	560	0.26	$1.04M_L + 17.69$	0.0523

In each case, the Lg model listed is consistent with our preferred Pn model, as discussed in Section 2. Figure 3.3 plots the predicted Lg spectra for a magnitude 3.0 explosion at a range of 1000 km based on the Q models in Table 3.2. The 1-5 and 1-7 Hz inversions give very similar results, while the 1-3 Hz inversion produced a lower Q at high frequency. This supports the contention that Sn coda affects the Lg attenuation estimate at frequencies greater than 3 Hz. Of course, the different Q models in Table 3.2 may reflect the contribution of effects in addition to those from the Sn coda. In Section 4 we show that Lg is rarely detected with maximum signal-to-noise above 2-3 Hz beyond about 1000 km. Therefore, the bias in Q_{Lg} due to Sn coda does not affect our estimates of Lg detectability at these ranges.
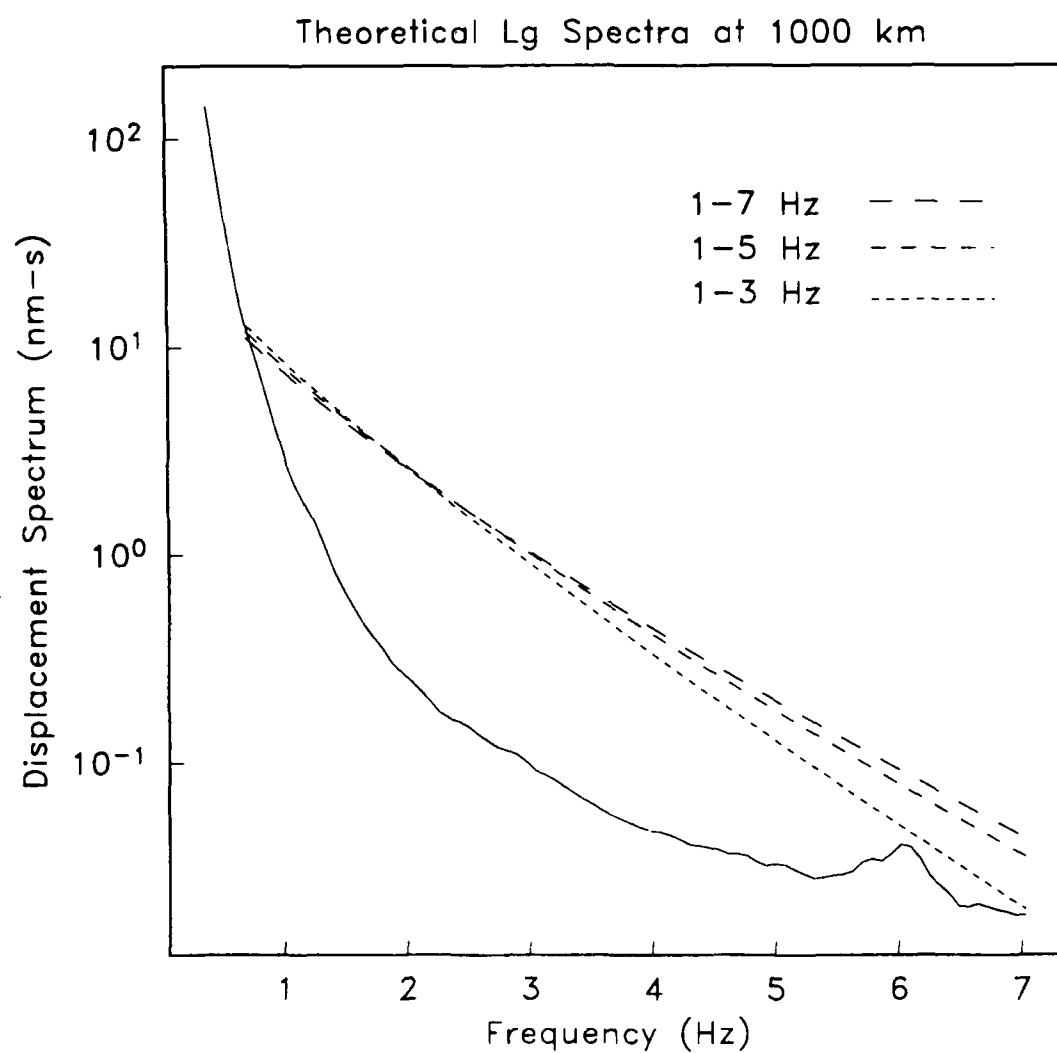
Figure 3.3. Comparison of theoretical *Lg* spectra for a magnitude 3.0 explosion at 1000 km based on the inversion results for 1-7, 1-5, and 1-3 Hz bandwidths. The lower curve is the pre-*Pn* noise. We interpret the difference between the 1-3 Hz and 1-7 Hz curves as the affect of *Sn* coda contamination.

51

4. NORESS DETECTION CAPABILITY

The detection and post-detection processing of events recorded at NORESS is incorporated into the automated array-processing package RONAPP [*Mykkeltveit and Bungum*, 1984]. *RONAPP* applies a conventional STA/LTA detection algorithm to a set of filtered beams. A detection occurs when the STA/LTA exceeds a predetermined threshold. Thus, regional event detection is based on time domain amplitudes observed on filtered beams. An important application of our inversion results is the simulation of range-dependent spectra of regional phases for events of arbitrary magnitude (Figures 2.13, 2.15-2.16). However, to use these to estimate detection capability, it is necessary to establish a connection between predicted signal-to-noise ratios based on the spectral modeling and the observed STA/LTA on filtered beams. In this section, we establish this connection based on the 186 regional events used in our inversion. We also attempt to separate the single-channel detectability from detectability specific to the NORESS array configuration and beamforming so we can extrapolate to other areas where the attenuation has been estimated. The following outlines our approach:

- Compare observed NORESS detection statistics to those predicted based on the inversion results.

- Express the temporal SNR used in signal detection in terms of the single channel spectral SNR and the beam gain. This factorization permits the extrapolation to other areas or to other station configurations. We find that we are able the express the *Pn* SNR in this way, but that the relationship for *Lg* is complicated by dispersion and the non-stationarity of pre-*Lg* noise.

- Parameterize pre-*Lg* noise as a function of frequency, epicentral distance, magnitude, and beam type. Express the *Lg* STA in terms of the array-averaged spectral amplitudes. Use these to predict the *Lg* detectability based on the results of the inversion.

- Compare the observed regional wave detection capability to predictions based on our parameterization of spectra recorded at NORESS. Their general agreement improves our confidence in extrapolating the results based on NORESS to other regions.

We begin with a description of the database (Section 4.1). Section 4.2 is a brief summary of detection statistics compiled for regional *Pn* and *Lg* phases recorded at NORESS. In Sections 4.3 and 4.4 we establish a relationship between the array-averaged spectral amplitudes used in the inversion and the time domain amplitudes recorded on the beam with maximum signal-to-noise. We compare the independent time and frequency domain measurements of signal-to-noise in Section 4.5 to estimate the average beam gain. In Section 4.6 we present the results of an empirical parameterization of the observed detectability. We compare the *Pn* and *Lg* detection capability derived from this parameterization to predictions based on our inversion results and to estimates obtained by *Ringdal* [1986] for the same region.

52

4.1 Data

Detection statistics for the 186 regional events used in the inversion (Table 2.1 and Figure 2.1) were compiled from the output of the array processing program *SAIAP*. Figure 4.1 plots the magnitude distribution of the events used in this study. The average M_L in the 250-700 km distance range is 2.3 and between 700-1450 km it is 2.9. Of these events, 152 were used in the *Pn* inversion and 160 were used for *Lg*. Events were excluded from one of the inversions if the phase was not detected or if it had low signal-to-noise over the bandwidth inverted. The second criterion does not apply to the analysis of time-domain amplitudes. Therefore, we were able to use all 186 of the events for *Pn* and 170 events for *Lg* in our time-domain study.

The output of *SAIAP* includes the STA and LTA for each detection measured on the standard beam with greatest signal-to-noise. Table 4.1 lists the standard beams used by *SAIAP*. The NORESS array includes 25 short period instruments in four concentric rings with a maximum diameter of 3.0 km (Figure 4.2). The weights given to each sensor in beamforming are given in Table 4.1. Beams 1-7 and 17-20 are infinite-velocity beams, 8-16 are steered beams, and 21-24 are horizontal beams. No more than three steering azimuths are used for a given frequency filter. Beams 1-17 are coherent beams and 18-24 are incoherent beams. Coherent beams are formed by delaying each channel by the proper amount determined from the steering azimuth and velocity, summing all channels, and band-pass filtering. Incoherent beams are formed by band-passing each channel, delaying and rectifying, and summing all channels. Incoherent beams are particularly well-suited for detection of signals with low coherency across the array [*Ringdal*, 1985b].

4.2 Detection statistics

In this section, we discuss *Pn* and *Lg* detection statistics for the events listed in Table 2.1. Table 4.2 lists the number of *Pn* and *Lg* detections on each of the beams. Since *SAIAP* only outputs information for the beam with the maximum signal-to-noise ratio (SNR), the detection statistics refer only to those beams. That is, a phase may be detected on many beams but it is only listed in Table 4.2 under the beam with the maximum SNR. All but one of the *Pn* detections are on coherent beams, whereas 68% of the *Lg* detections are on incoherent beams. Excluding the steered beams, the percentage of *Lg* detections on incoherent beams increases to 92%. This is consistent with the results of *Ringdal* [1985b] who found that for phase velocities less than 6.0 km/s (secondary phases), the maximum SNR is almost always on an incoherent beam.

Figure 4.3 groups the percentage of detections for each frequency filter into four distance ranges. That is, we combine detections on different beams with the same frequency filter. As expected for both *Pn* and *Lg*, detections from close events generally occur on a higher-frequency beam than those from events at larger distances. For example, the maximum SNR for *Pn* typically occurs at a frequency greater than 8 Hz at distances less than 400 km and between 3-5 Hz in the 700-1000 km distance range. This is consistent with the results of *Ringdal* [1985a] who found that the best SNR for *Pn* increased from 3-5 Hz at about 1000 km
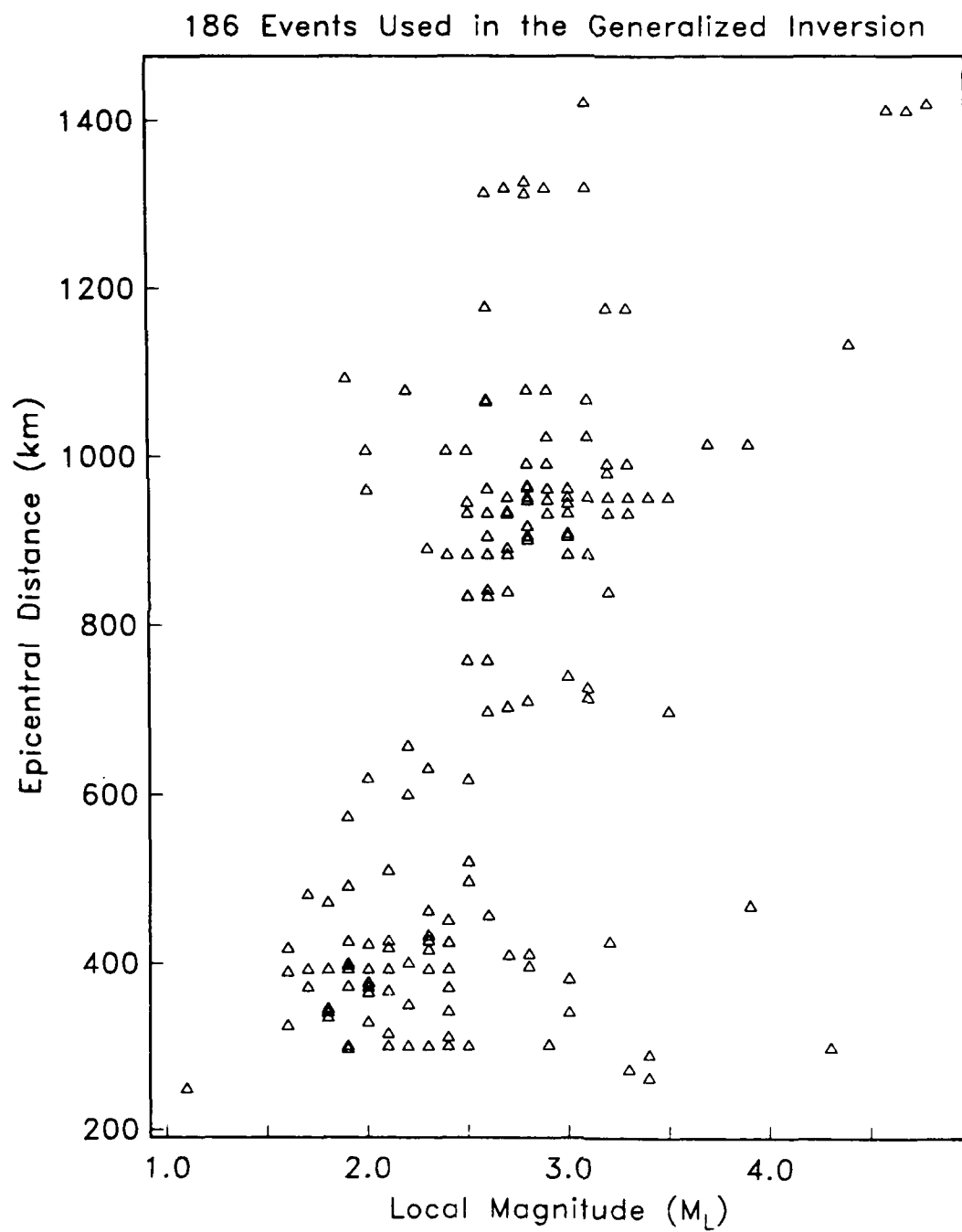
53

186 Events Used in the Generalized Inversion

Figure 4.1. Magnitude distribution of the 186 events used in the inversion.

54

Beam	Azi	Slow	Filter	Type	Weights	Threshold
					AAAAAABBBBBCCCCCCCCCCCCCCDDDDDDDDD	
					00012312345122234445677712345678	
					ZENZZZZZZZZZZZENZZENZZZENZZZZZZZZZ	
1	0.	0.00	1.0-3.0	C	10000000000110011001110011111111	4.0
2	0.	0.00	1.5-3.5	C	10000000000110011001110011111111	4.0
3	0.	0.00	2.0-4.0	C	10000011111110011001110011111111	4.0
4	0.	0.00	2.5-4.5	C	10000011111110011001110000000000	4.0
5	0.	0.00	3.0-5.0	C	10000011111110011001110000000000	4.0
6	0.	0.00	4.0-8.0	C	10011111111000000000000000000000	5.0
7	0.	0.00	8.0-16.0	C	10011111111000000000000000000000	5.0
8	0.	0.07	2.0-4.0	C	10000011111110011001110011111111	4.0
9	90.	0.07	2.0-4.0	C	10000011111110011001110011111111	4.0
10	180.	0.07	2.0-4.0	C	10000011111110011001110011111111	4.0
11	15.	0.07	2.5-4.5	C	10000011111110011001110011111111	4.0
12	75.	0.07	2.5-4.5	C	10000011111110011001110011111111	4.0
13	135.	0.07	2.5-4.5	C	10000011111110011001110011111111	4.0
14	25.	0.07	3.0-5.0	C	10000011111110011001110011111111	4.0
15	75.	0.07	3.0-5.0	C	10000011111110011001110011111111	4.0
16	125.	0.07	3.0-5.0	C	10000011111110011001110011111111	4.0
17	0.	0.00	2.0-4.0	C	10000011111110011001110000000000	4.0
18	0.	0.00	1.0-2.0	I	10000000000110011001110000000000	2.5
19	0.	0.00	2.0-3.0	I	10000000000110011001110000000000	2.5
20	0.	0.00	2.0-4.0	I	10000000000000000000000111111111	2.1
21	0.	0.00	2.0-4.0	I	01000000000001000100010000000000	6.0
22	0.	0.00	2.0-4.0	I	00100000000001000100001000000000	6.0
23	0.	0.00	4.0-8.0	I	01000000000001000100010000000000	6.0
24	0.	0.00	4.0-8.0	I	00100000000001000100001000000000	6.0

Table 4.1. Standard Beams used by *SAIAP*. Listed are beam number, steering azimuth and slowness, frequency filter, beam type (coherent or incoherent), sensor weights, and detection thresholds. The individual sensors are identified by ring (A-D), sensor number (0-9), and component (Z, N, or E). The thresholds were determined from false alarm statistics [*Kvaerna et al.*, 1988a].
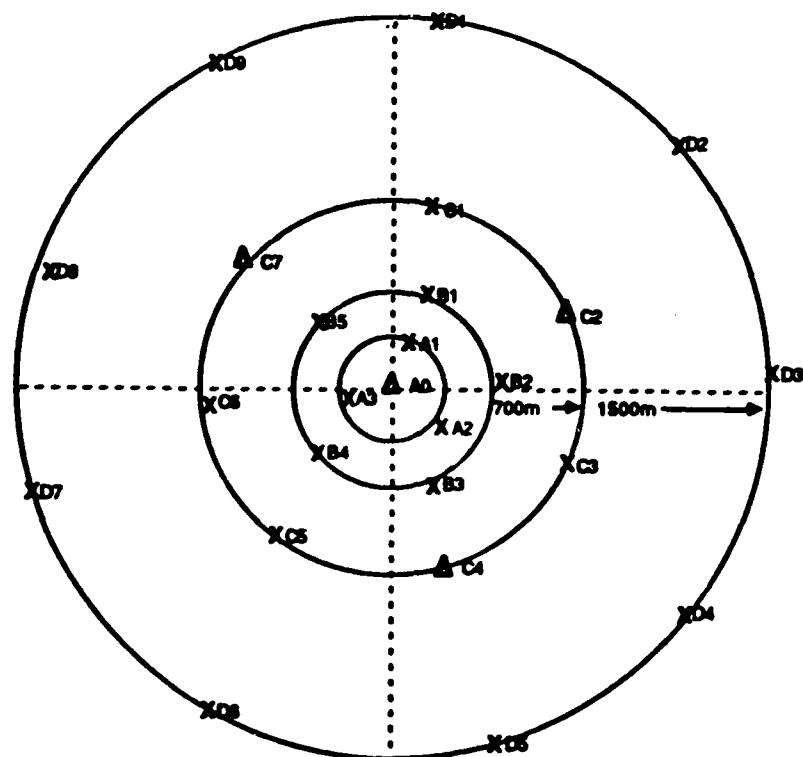
CENTER: 60.7353N, 11.5414E

X - SINGLE VERTICAL INSTRUMENT
△ - THREE COMPONENT INSTRUMENT

Figure 4.2. NORESS array configuration. The array consists of 25 short-period instruments in concentric rings with a maximum diameter of 3 km. The array was designed for the enhancement of frequencies between 1.5 and 5.0 Hz [*Mykkeltveit*, 1983].

56

Table 4.2. Beams with maximum SNR.

Beam	Pn Detections	Lg Detections
1	1	2
2	2	3
3	-	3
4	12	-
5	15	-
6	31	-
7	56	-
8	6	2
9	8	7
10	2	1
11	4	7
12	17	4
13	-	8
14	7	5
15	18	5
16	6	5
17	-	2
18	-	35
19	-	40
20	1	19
21	-	7
22	-	13
23	-	1
24	-	1

Pn

(a)

250 ≤ r < 400 Km
55 EVENTS

400 ≤ r < 700 Km
29 EVENTS

700 ≤ r < 1000 Km
69 EVENTS

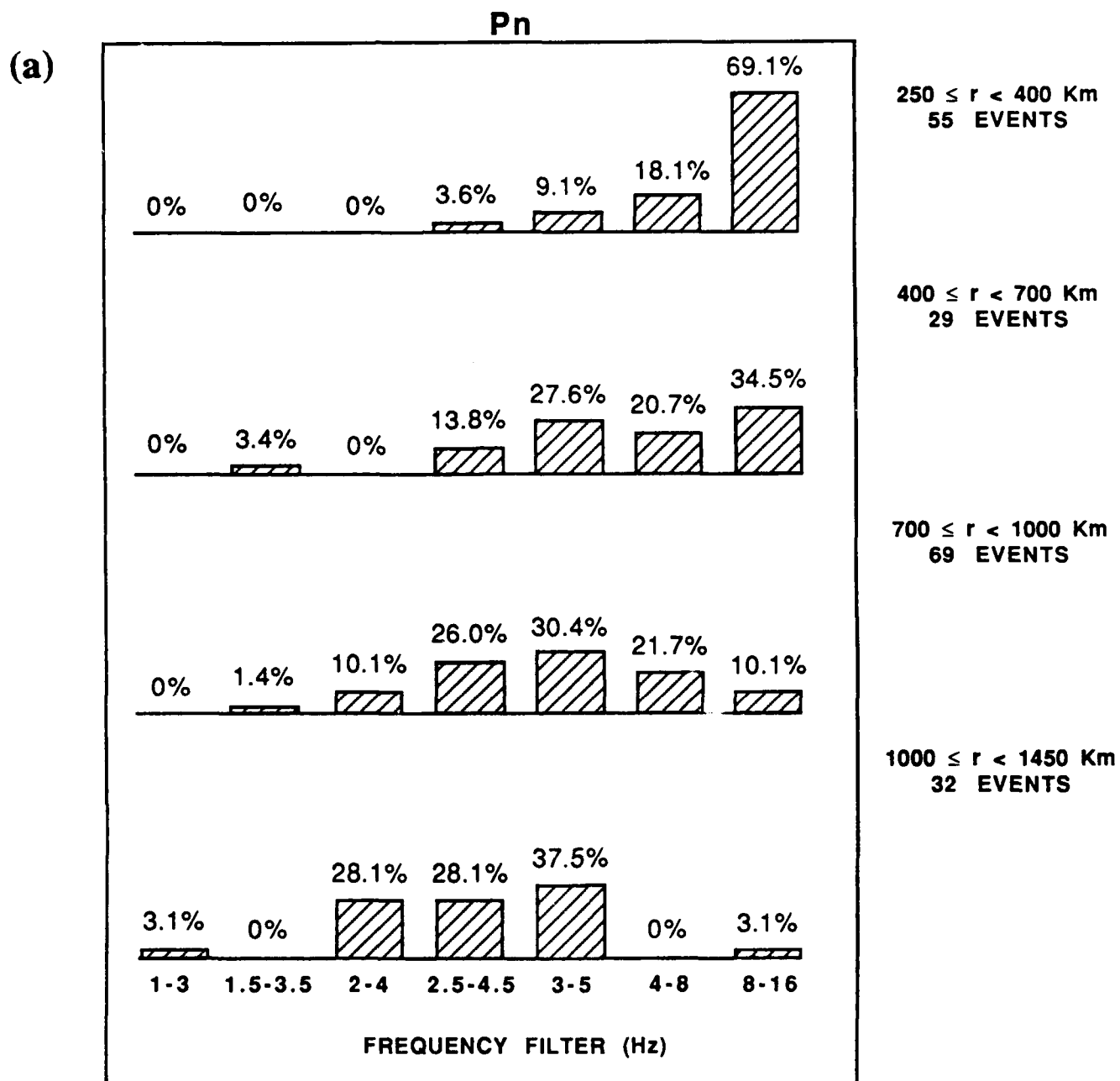1000 ≤ r < 1450 Km
32 EVENTS

FREQUENCY FILTER (Hz)

Figure 4.3. Percentage of detections with the maximum SNR for each frequency filter grouped into four distance ranges for (a) *Pn* and (b) *Lg*. The distance intervals and the number of events for each interval are indicated on the right.
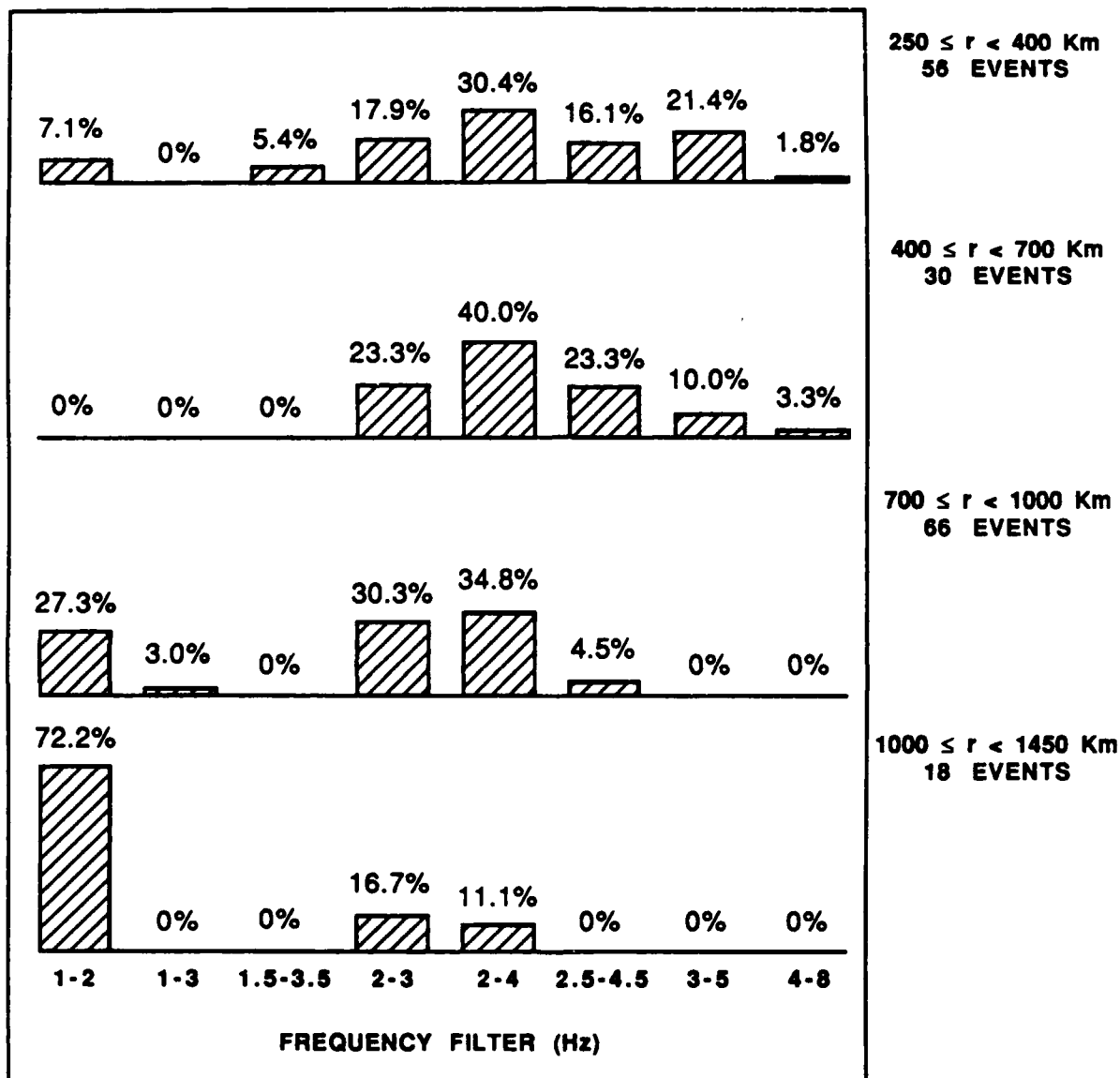
Lg

(b)

250 ≤ r < 400 Km
56 EVENTS

400 ≤ r < 700 Km
30 EVENTS

700 ≤ r < 1000 Km
66 EVENTS

1000 ≤ r < 1450 Km
18 EVENTS

Figure 4.3. (Continued).

59

to more than 8 Hz at local distances. On the other hand, the maximum SNR for Lg is rarely above 4 Hz. For distances less than 800 km, Lg is usually detected on beams with center frequencies between 2.5-4 Hz. At longer ranges, the maximum SNR is between 1-3 Hz.

It is possible to compare these statistics to predictions based on the results of our inversion. From our Q_{Pn} model and an average NORESS ambient noise spectrum [*Henson and Bache*, 1988], we can predict the frequency of the maximum SNR as a function of distance. Of course, the prediction also depends on our estimate of source corner frequency. Figure 4.4a plots the predicted frequency of the maximum SNR as a function of distance based on our Pn inversion results. Between 250-700 km, we use a value for seismic moment consistent with $M_L = 2.3$ (the average magnitude in this distance range) which gives a source corner frequency estimate of 17.7 Hz. For ranges between 700-1450 km we use $M_L = 2.9$ and $f_c = 10.8$ Hz. Overall, there is good agreement between the predictions and observations (compare Figures 4.3a and 4.4a). For example, at ranges less than 400 km the model predicts Pn detection on the highest-frequency beam, which is consistent with the observations. However, between 400-700 km more detections are observed between 3-5 Hz than would be suggested by the model. Since most of these detections are on steered beams, a likely explanation is that the SNR gain introduced by steering to the event azimuth exceeds the SNR advantage at higher frequency. Beyond 700 km there is adequate agreement between the observed and predicted frequency of the maximum SNR. Since at large distances the frequency of the maximum SNR (4-5 Hz) is considerably lower than the source corner frequency, it follows that it is controlled by path attenuation rather than characteristics of the source spectrum.

The corresponding analysis is not possible for Lg since we don't have a parameterization of the pre-Lg noise spectrum. However, because the Lg spectrum decays much more rapidly than the Pn spectrum, we expect the frequency of the maximum SNR to be lower for Lg than for Pn. Figure 4.4b plots the predicted frequency of the maximum SNR using the Lg inversion results for 5-s windows and the ambient noise spectrum. As long as the pre-Lg spectrum decays at a rate less than or equal to the rate of decay of the ambient noise spectrum, we can use the ambient noise to predict an upper bound on the frequency of the maximum SNR for Lg. At large distances this is only true for frequencies less than about 4 Hz (for example, see the lower inset in Figure 3.2), where the slope of the ambient noise spectrum is considerably steeper than at higher frequencies. Since the predicted frequency of the maximum SNR beyond about 800 km is less than 4 Hz, it is reasonable to consider it an upper bound. At these longer ranges there is satisfactory agreement between the predictions and observations (compare Figures 4.3b and 4.4b). However, at short ranges (< 300 km) the model predicts the maximum SNR at a higher frequency than is observed. This is not surprising since at these ranges the pre-Lg spectrum generally decays less rapidly than the ambient noise spectrum over the entire 0.5-20 Hz band (for example, see the upper inset in Figure 3.2) and Figure 4.4b is simply an upper bound on the frequency of the maximum SNR. Note that the predicted shift to lower frequencies between 600-800 km in Figure 4.4b is largely controlled by the curvature of the ambient noise spectrum and is therefore without much physical significance.

Steered beams. Table 4.3 lists the number of Pn and Lg detections as a function of beam center frequency. The number of detections on steered beams is shown in parentheses. Pn detections on steered beams constitute 70% of all Pn detections over the frequency band
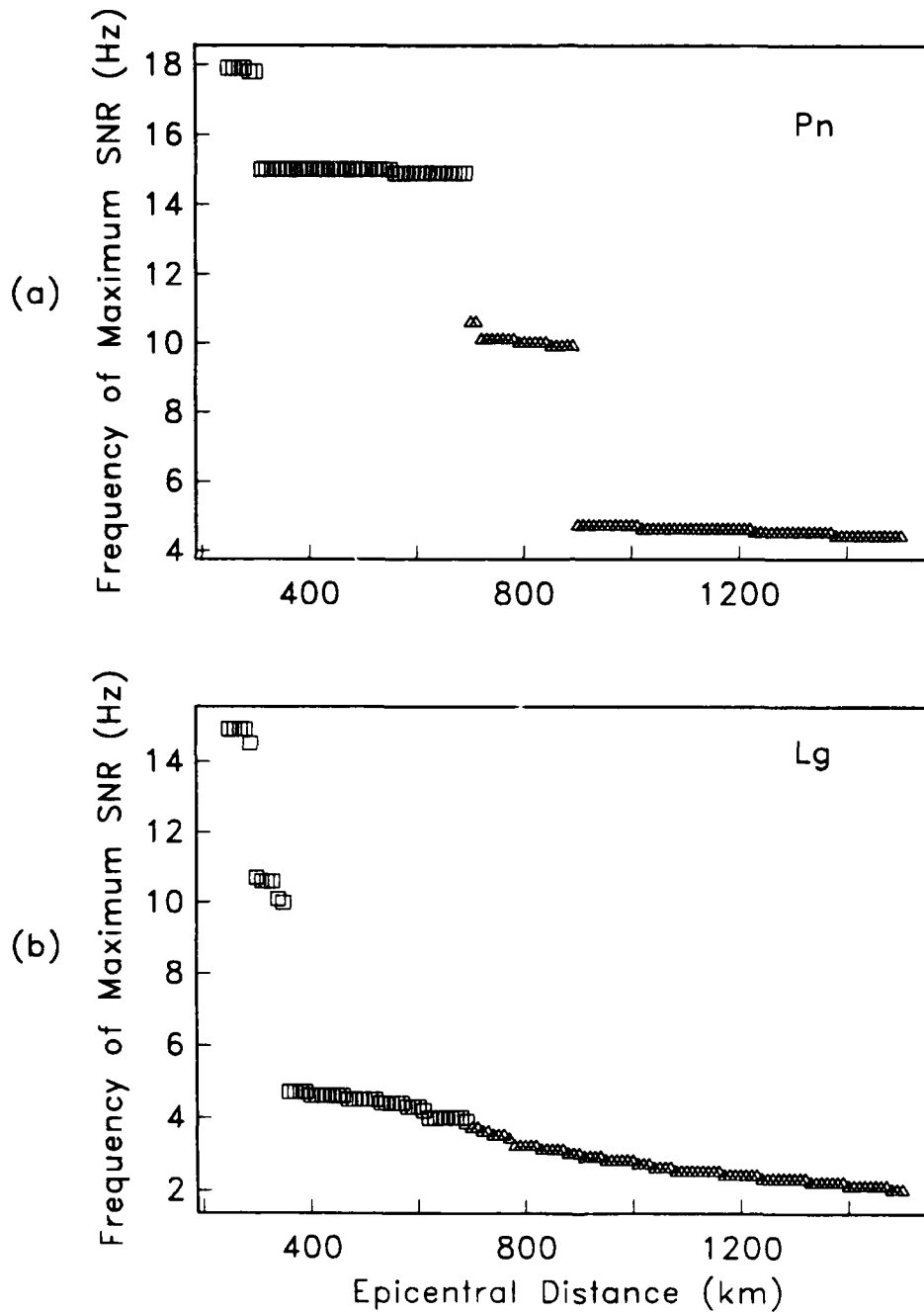
Figure 4.4. Predicted frequency of the maximum SNR as a function of range for (a) *Pn* and (b) *Lg* based on the results of our inversion. Between 250-700 km, the predictions are for a corner frequency consistent with $M_L = 2.3$ (squares) and at longer ranges with $M_L = 2.9$ (triangles). The frequency of the maximum SNR is an upper bound for *Lg* since it is based on the ambient noise spectrum (see text).

61

covered by the steered beams. This is consistent with the results of *Kvaerna and Mykkeltveit* [1986] who found significant improvement in beam gain for steered beams for frequencies greater than 2.5 Hz. Figure 4.5a plots beam number versus epicentral distance for *Pn*. There are very few *Pn* detections on steered beams at distances less than about 600 km. This is not surprising because there are no steered beams with center frequencies greater than 4 Hz, and at shorter ranges the frequency of the maximum SNR is considerably higher than this (Figure 4.4a). Figure 4.5b displays beam number versus event-to-station azimuth. The steering azimuths of beams 8-16 are shown as horizontal tic marks. Most of the *Pn* detections on steered beams were from events at azimuths close to the steering azimuth.

Table 4.3. Number of detections as a function of beam center frequency.
(Detections on steered beams in parenthesis)

Center Frequency	Pn Detections	Lg Detections
1.5	-	35
2.0	1	2
2.5	2	43
3.0	17(16)	54(10)
3.5	33(21)	19(19)
4.0	46(31)	15(15)
6.0	31	2
12.0	56	-

Lg is detected on steered beams (or coherent beams in general) only at short epicentral distances (Figure 4.6a). All of the *Lg* detections on coherent beams above a filter center frequency of 3.0 Hz are on steered beams. *SAIAP* does not include a high-frequency incoherent beam, so at distances where the maximum SNR is greater than 3 Hz, the *Lg* detection often occurs on a coherent beam. Note that the higher frequency *Lg* detections are nearly exclusively on steered beams even though the steering azimuth is not close to the event-to-station azimuth (Figure 4.6b). This is simply because the steered beams use a larger array aperture (A0, B, C, and D rings) than the infinite velocity coherent beams.
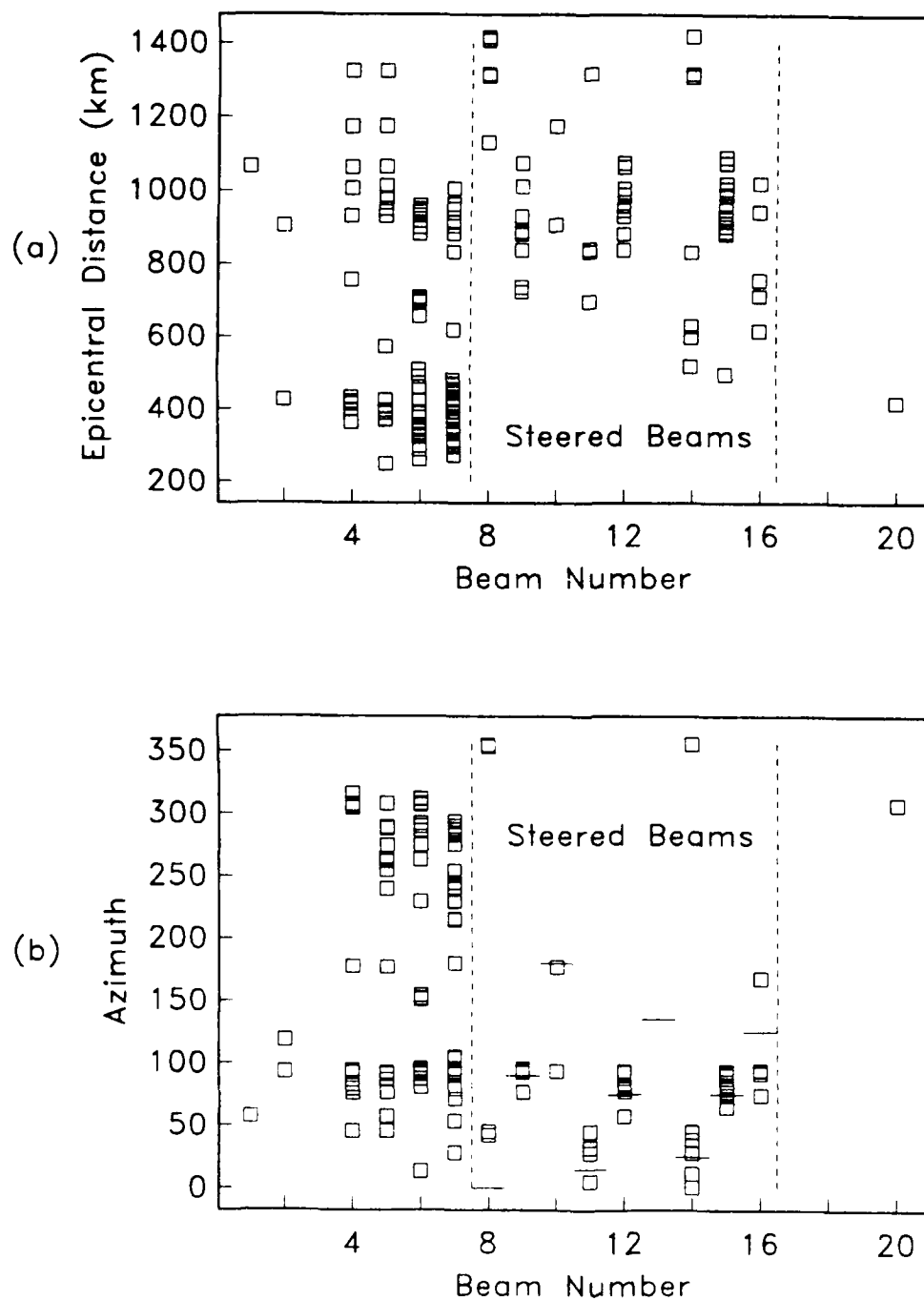
Figure 4.5. Beam with the maximum SNR for *Pn* as a function of (a) distance and (b) event-to-station azimuth. Beams 8-16 are steered beams, the other *Pn* detections are on infinite velocity beams (Table 4.1). The small tic marks in 4.5b are plotted at the beam steering azimuths.
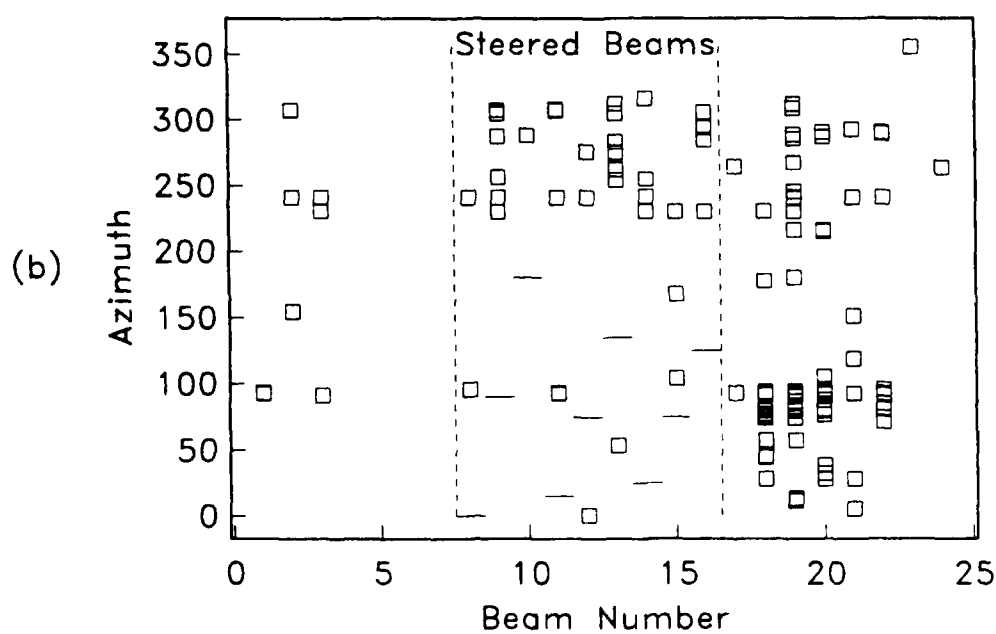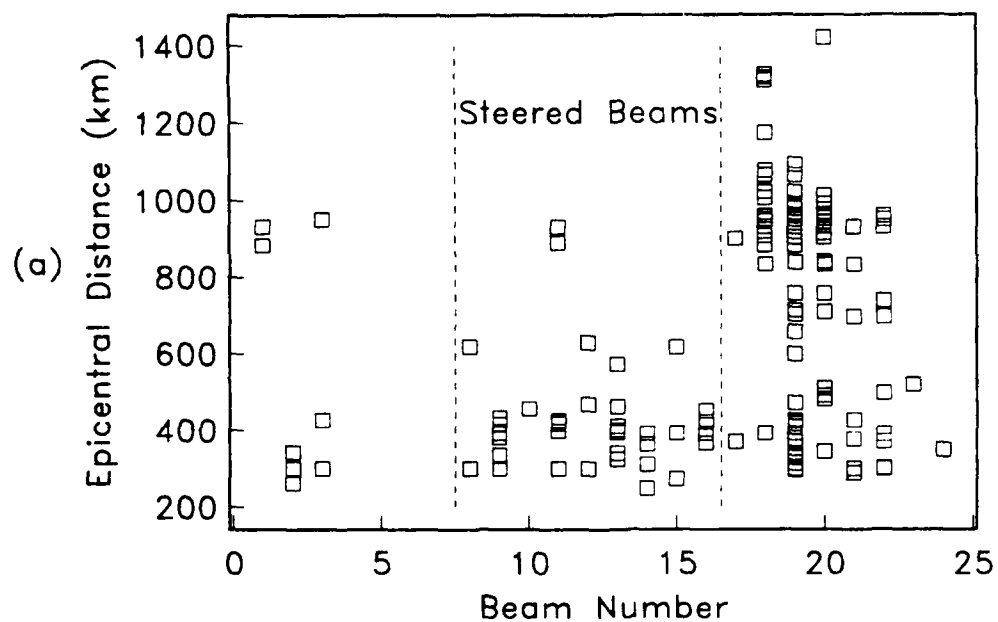
Figure 4.6. Beam with the maximum SNR for Lg as a function of (a) distance and (b) event-to-station azimuth. Beams 8-16 are steered beams. The small tic marks in 4.6b are plotted at the beam steering azimuths.

64

4.3 Noise spectra and LTA

Qualitatively, the LTA (long term average) is a measure of the rms amplitude on a filtered beam averaged over about 30 s prior to a detection. The LTA is updated every 0.5 s and at the ith 0.5 s interval is expressed as

$$LTA_i = (1 - 2^{-5})^{i-1} LTA_1 + \sum_{k=1}^{i-1} 2^{-5} (1 - 2^{-5})^{k-1} STA_{i-1-k} \qquad (4.1)$$

where STA (short term average) is the absolute amplitude averaged over a 1 s window and updated every sample. For large i, the first term goes to zero (e.g., after ~30 s the LTA is not sensitive to its starting value) and the LTA is simply expressed as a weighted sum of past STAs. The weighting function is shown in Figure 4.7.

There is a simple relationship between the rms amplitude of random noise and its power spectral density [e.g. *Aki and Richards*, 1980; p. 493]. From Parseval's theorem

$$A_{rms} \approx (2 \ PSD \ \Delta f)^{1/2} \qquad (4.2)$$

where Δf is the bandwidth and *PSD* is the power spectral density. This equation assumes that the *PSD* is flat over the bandwidth Δf. The LTA is an approximate measure of the rms noise amplitude on a filtered beam and should be approximately related to the *PSD* of the beam by (4.2) where Δf is the filter bandwidth.

4.3.1 Pn noise. To test the applicability of (4.2) to pre-*Pn* (or ambient) noise, we computed spectra of unfiltered beams over various sub-arrays. Figure 4.8 compares the average noise spectra recorded on unfiltered beams over the four sub-arrays used in the standard beams to the average single-channel noise spectrum [*Henson and Bache*, 1988]. For frequencies less than about 4 Hz the noise level is significantly reduced by including the two outer rings of the array. In particular, the beam including sensors on only the C and D rings gives better noise suppression than can be achieved using the whole array [*Kvaerna and Mykkeltveit*, 1986]. However, beyond 5-6 Hz only marginal improvement in noise suppression can be achieved by including the outer rings. Superimposed on the spectra are the squared LTAs divided by $2\Delta f$ for the 186 *Pn* detections. For all but the highest-frequency beam, the LTAs are corrected for the instrument response and plotted at the filter center frequency. For these beams, the *Pn*-LTAs are approximately related to the beam noise spectra via (4.2) at the beam center frequency. However, the LTAs measured on the 8-16 Hz beam are consistent with (4.2) at a frequency of about 10 Hz. This is an important distinction for detection capability assessment. This implies that the temporal SNR cannot be predicted based on a spectral parameterization of the signal and the noise at the same frequency unless narrow band filters are used in beamforming. Otherwise the dominant signal frequency may exceed the the dominant noise frequency within the filter bandwidth. This is discussed in more detail in Section 4.6.

Figure 4.9 plots the noise suppression spectrum defined as the ratio of the beam power spectrum to the array-averaged single-channel power spectrum [*Fyen*, 1986]. The dashed lines indicate a power ratio of 1/N where N is the number of elements used in beamforming. The four plots are for the different sub-arrays. In general, we find that at least 1/N noise

65

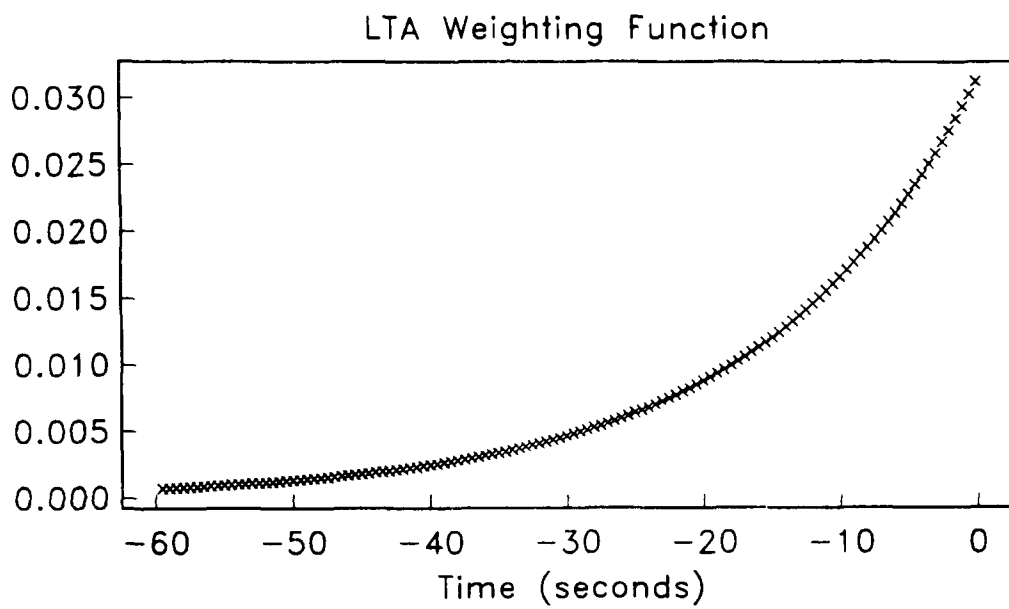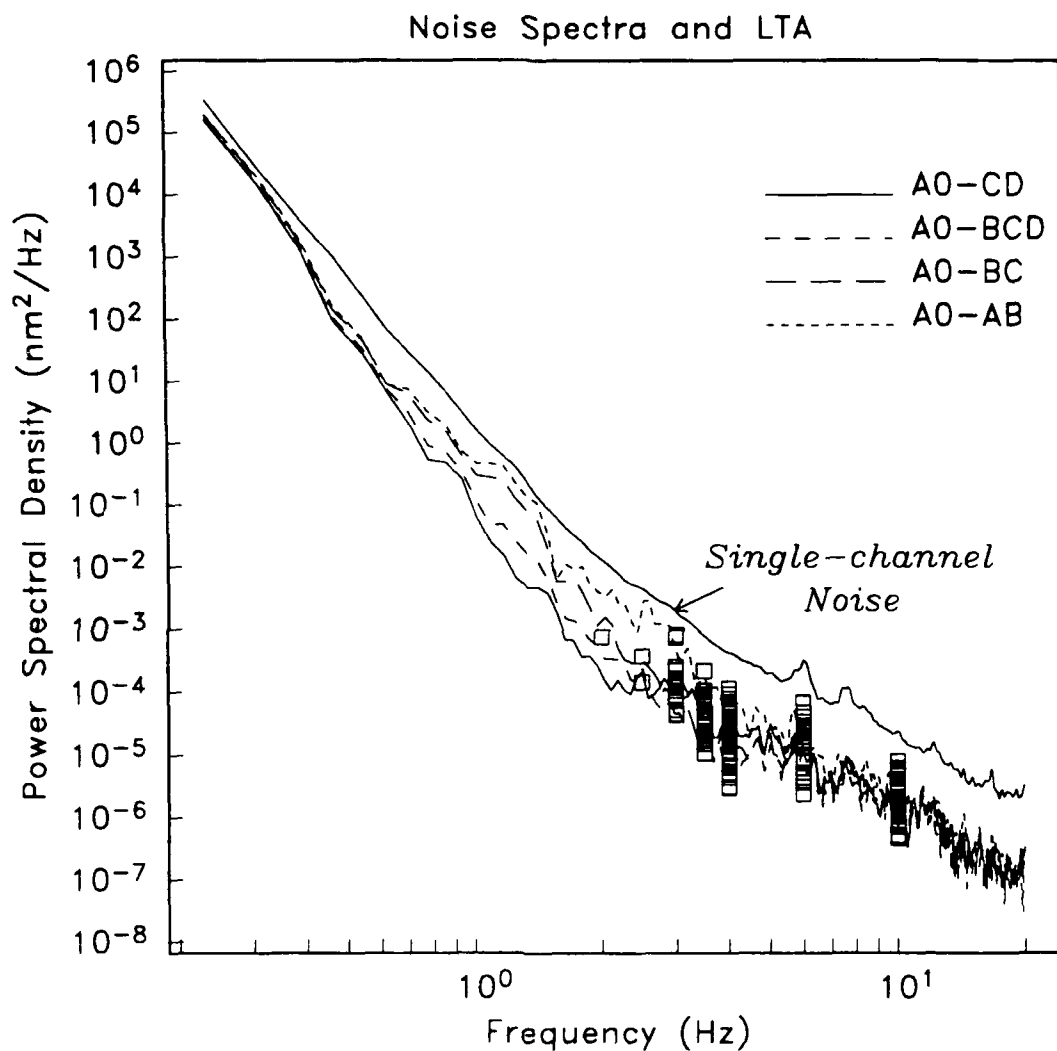Figure 4.7. Long term average (LTA) weighting function.

66

Figure 4.8. Average NORESS ambient noise power spectral density. The array-averaged single-channel spectrum is from *Henson and Bache* [1988]. The beam spectra are averages of 10 noise samples calculated for the various sub-arrays. All spectra are corrected for the instrument response. The squares are Pn-LTAs divided by $2\Delta f$ for 186 events.
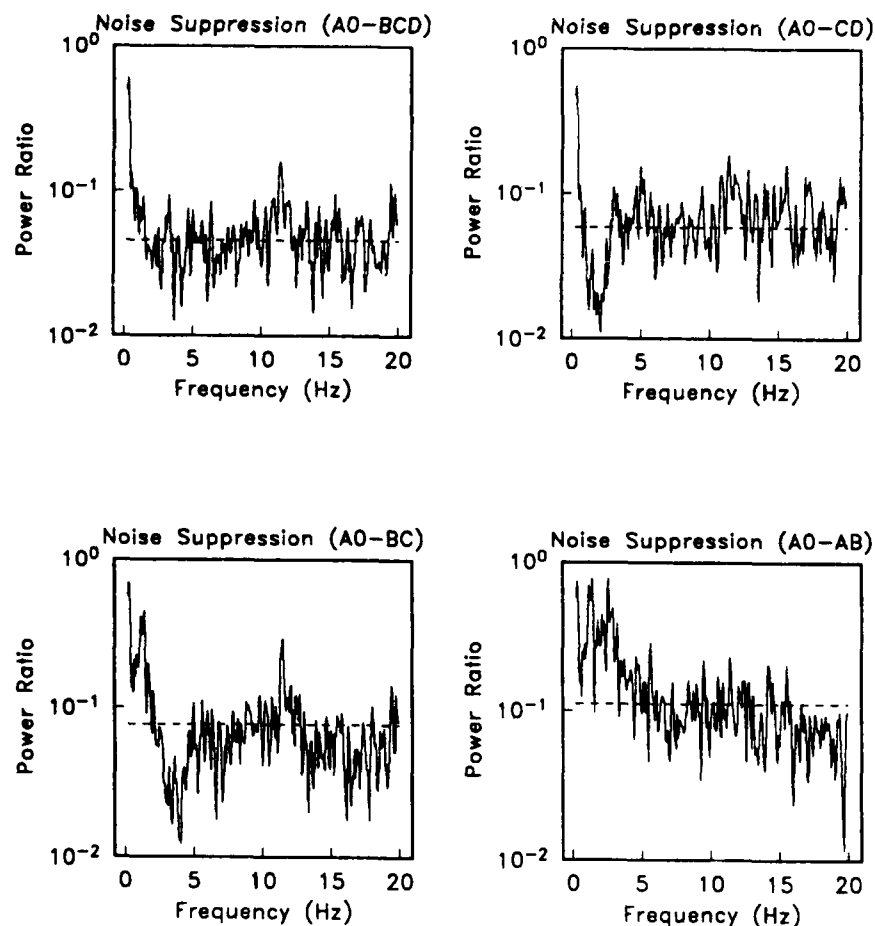
Figure 4.9. Noise suppression spectra for coherent beams formed over four sub-arrays. These spectra were computed as the ratio of the average beam spectra and the single-channel spectrum displayed in Figure 4.8. The dashed line is plotted at a power ratio of $1/N$ where N is the number of elements used in beamforming. Note that for the BC and CD rings considerably better than $1/N$ noise suppression is achieved over a limited frequency band [*Fyen*, 1986].

68

suppression ($1/\sqrt{N}$ in noise amplitude) is achieved over the frequency band used for each of the sub-arrays. However, the signals are also suppressed by beamforming, and this must also be considered in establishing the frequency-dependent beam gain.

4.3.2 Lg noise. The inversion results provide an accurate parameterization of single-channel *Lg* signal spectra as a function of magnitude, distance, and frequency. We also have a stable average for the single-channel ambient noise spectrum at NORESS. However, the pre-*Lg* noise consists of ambient noise, *Pn* coda, and *Sn* coda. Therefore, we do not expect a simple relationship between *Lg*-LTA and the ambient noise spectrum. For example, Figure 4.10 plots the squared LTAs for *Lg* divided by $2\Delta f$ and the average noise power spectral density of beams calculated over the sub-arrays appropriate for *Lg* detection. Of course, the time-domain noise levels for *Lg* are considerably higher than those predicted by (4.2) using the ambient noise power spectral density. The large scatter in the LTAs for a given frequency is caused by a magnitude dependence in the *Sn* coda amplitude, as will be discussed below.

Since we don't have a spectral parameterization of single-channel pre-*Lg* noise, it doesn't make sense to try to relate temporal and spectral amplitudes as was done for *Pn*. Therefore, in this section we simply parameterize the observed *Lg*-LTAs. The pre-*Lg* noise is dominated by *Sn* coda and, therefore, we expect that it may depend on magnitude, distance, frequency, and beamforming. Specifically,

- *Magnitude.* The *Sn* amplitude increases with increasing magnitude, therefore the *Lg*-LTA should also increase with increasing M_L. This is particularly true at short ranges (< 200 km) where the difference in travel time between the *Lg* and *Sn* phases is small.

- *Distance.* The *Lg*-LTA is expected to decrease with increasing epicentral distance as it emerges later in a decaying *Sn* coda.

- *Frequency.* The *Lg*-LTA decreases with increasing frequency because the *Sn* coda, *Pn* coda, and ambient noise spectra all decay with frequency.

- *Beamforming.* *Lg* is detected on both coherent and incoherent beams (Table 4.2). The noise suppression on incoherent beams is less than that on coherent beams due partly to the number of array elements used in beamforming, and partly to the correlation lengths of the *Sn* coda. Therefore, we expect the *Lg*-LTAs on coherent beams to be lower than those on incoherent beams.

Considering these factors, we parameterize the *Lg*-LTA as

$$\log(LTA) = A_0 + \gamma(r)M_L + d(r) + F(f) + b \qquad (4.3)$$

where the functions $\gamma(r)$, $d(r)$, $F(f)$, and b are empirically determined using LTA measurements from 170 events. The function $\gamma(r)$ describes the magnitude dependence of the *Lg*-LTA. At close ranges it is expected to have a value near one and it should decrease with increasing distance since the time separation between *Lg* and *Sn* increases. The function $d(r)$ describes the reduction in the *Lg*-LTA with distance due to the decay of the *Sn* coda amplitude. The fre-
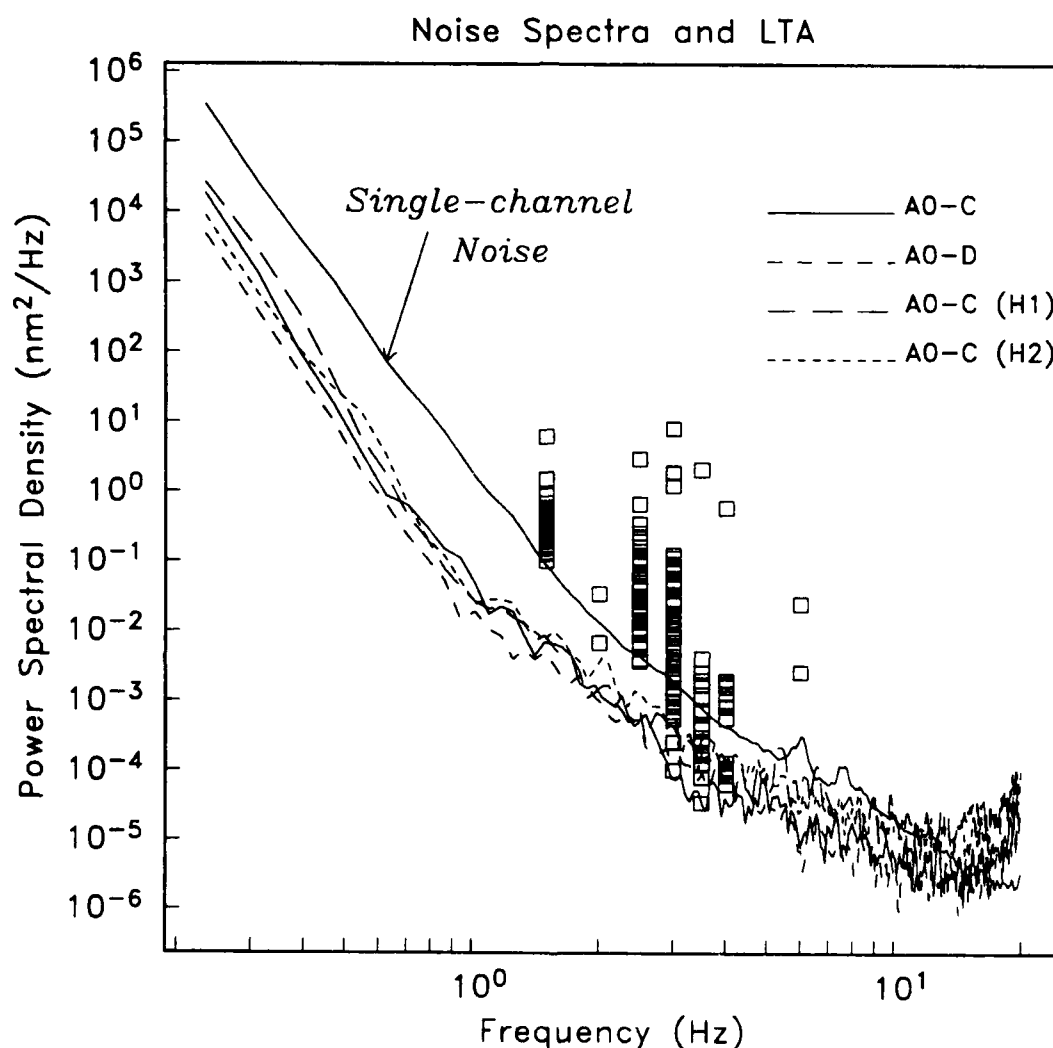
Figure 4.10. Average NORESS ambient noise power spectral density for incoherent beams. The array-averaged single-channel spectrum is from *Henson and Bache* [1988]. The beam spectra are averages of 10 noise samples calculated for the sub-arrays used for incoherent beamforming. The A0-C spectrum is for beams 18-19, A0-D is for beam 20, and A0-C (H1) and (H2) are for horizontal beams 21-24. All spectra are corrected for the instrument response. The squares are Lg-LTAs divided by $2\Delta f$ and plotted at the filter center frequency.

quency dependence of the LTA is represented by the term $F(f)$, and b is a constant that depends on beam type (coherent or incoherent).

Figure 4.11 plots Lg-LTA versus NORESS local magnitude in two separate distance ranges. Since Lg is most frequently detected on incoherent vertical beams, we will reference all quantities in (4.3) to measurements made on that beam type. For ranges less than 700 km, the best-fitting straight line to log(LTA) as a function of magnitude has a slope near 0.8 for both incoherent vertical beams (circles) and coherent beams (squares). For incoherent beams at ranges less than 700 km the best-fitting straight line is

$$\log(LTA) = 0.8M_L - 2.27 \qquad (4.4)$$

The incoherent vertical beams used in (4.4) have frequency filters between 2-4 Hz. Comparing to (4.3) we set $A_0 = -2.27$, $\gamma = 0.8$, $d(<700$ km$) = 0$, $F(2-4$ Hz$) = 0$, and b(incoherent beams) $= 0$. Since the slopes for coherent and incoherent beams are nearly the same and the center frequencies are all greater than 2 Hz, the difference in their intercepts gives b(coherent beams) $= -.78$.

At larger distances, γ was found to be only slightly less than 0.8. Therefore, for this distance range we simply use 0.8 but note that at ranges greater than about 1200 km the magnitude dependence is expected to decrease. For ranges greater than 700 km, almost all of the Lg detections are on incoherent beams. The triangles in the lower plot of Figure 4.11 are for Lg detections on the lowest-frequency beam (1-2 Hz) and the circles are for detections on higher-frequency beams (2-4 Hz). For fixed magnitude, distance, and beam type, the lower-frequency log(LTA) is greater than than that at higher frequency by 0.62. Since we set $F(2-4$ Hz$) = 0$, this implies $F(1-2$ Hz$) = 0.62$. Considering only the 2-4 Hz incoherent beam measurements at fixed magnitude, there is a vertical offset of 0.65 in log(LTA) between measurements made at ranges less than 700 km and those made at ranges greater than 700 km. Thus, using $d(<700$ km$) = 0$ gives $d(>700$ km$) = -0.65$.

In summary, we express log(LTA) as a function of magnitude, distance, frequency, and beam type using (4.3) with:

$$
\begin{aligned}
A_0 &= -2.27 \\
\gamma(r) &= 0.8 \\
d(r) &= 0 \quad\quad r < 700 \text{ km} \\
&= -0.65 \quad r > 700 \text{ km} \\
F(f) &= 0 \quad\quad f > 2 \text{ Hz} \\
&= 0.62 \quad f < 2 \text{ Hz} \\
b &= 0 \quad\quad \text{Incoherent Beams} \\
&= -0.78 \quad \text{Coherent Beams}
\end{aligned}
\qquad (4.5)
$$

where the LTA is measured in nanometers. We note that γ is expected to decrease with distance beyond about 1200 km and that $d(r)$ should vary smoothly with distance. However, the data used in this analysis do not permit finer resolution of these parameters.

71
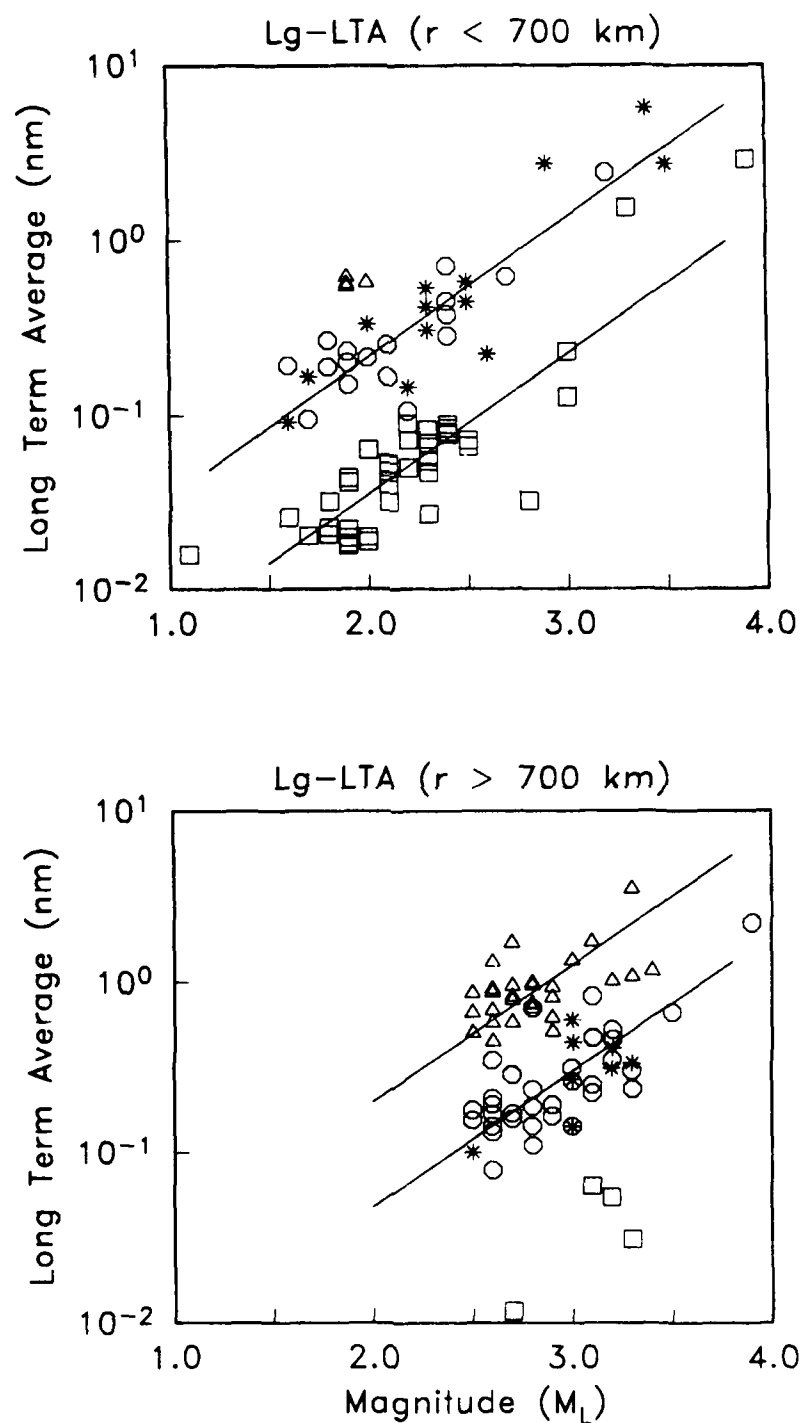
Figure 4.11. *Lg*-LTA versus NORESS local magnitude for distances < 700 km (top) and > 700 km (bottom). The triangles are detections on the lowest-frequency incoherent beam (18). The circles are detections on higher-frequency incoherent beams (19-20). Asterisks denote detections on horizontal beams (21-24) and the squares are *Lg* detections on coherent beams. The LTAs have been corrected for the instrument response at the filter center frequency.

4.4 Signal spectra and STA

The spectra used in this study are those automatically computed by *SAIAP* for each detected phase. They are computed for a 5-s window starting 0.3 s before the detection time on the vertical component and are noise-corrected and averaged across the array. In this section, we examine the relationship between these spectral amplitudes and the time-domain STA (short term average) amplitude on a filtered beam. The STA is defined as the average absolute amplitude in a 1-s window measured on the beam with the maximum SNR and is updated every sample.

4.4.1 Pn signal. As a rough approximation, the amplitude of a wavelet is the product of the amplitude spectral density and the bandwidth [*Aki and Richards*, 1980; p. 492]. That is, if the spectral density is purely real and equal to a constant F over Δf, then the peak time-domain amplitude is equal to $2 \Delta f F$. Since the STA is a measure of the average amplitude, we express it in terms of the amplitude spectral density of the beam as

$$STA = A_B(f_0) \, \Delta f \, \delta(f_0) \qquad (4.6)$$

where f_0 is the filter center frequency, Δf is the filter bandwidth, A_B is the amplitude spectrum of the beam, and δ is a correction term to account for dispersion. If all of the energy in the bandwidth Δf arrives at the same time then $\delta = 1$, otherwise $\delta < 1$. Since Pn is not strongly dispersed, we expect δ to be close to 1.

To estimate the function δ, we compare Pn beam spectra to the STAs for 10 events with various magnitudes and epicentral distances (Table 4.4). The STA is corrected for the instrument response at the filter center frequency of the detecting beam.

Table 4.4. Events used to calculate beam spectra.

Event	Date	Time	Location	Type	M_L
1	10-31-85	14:11	60.70N 29.00E	EX-V5	2.8
2	11-14-85	10:44	62.70N 17.76E	EQ	2.5
3	11-14-85	12:52	60.70N 28.70E	EX-V12	2.9
4	1-31-86	14:17	58.34N 6.43E	EX-TIT	1.9
5	3- 5-86	13:02	57.20N 7.00E	EQ	1.8
6	4- 4-86	22:42	70.86N 8.91E	EQ	3.4
7	4-30-86	10:19	59.31N 6.95E	EX-BLA	2.2
8	7- 1-86	15:28	60.70N 28.70E	EX-V12	2.7
9	7- 8-86	13:09	59.30N 27.20E	EX-E4	2.7
10	11-13-86	8:00	58.17N 8.10E	EQ	1.8

Comparing the STAs to the beam spectra at f_0 gives an average value for δ of 0.7. For example, Figure 4.12 shows the beam spectra for the events listed in Table 4.4. Each spectrum is labeled by the sub-array used in beamforming. The small dot on each spectrum is the quantity $STA/(\Delta f\, \delta)$ for $\delta = 0.7$, plotted at the center frequency of the beam. Although this analysis is restricted to a small data set, it indicates that for Pn there is a consistent value of δ that relates the time-domain amplitudes and the amplitude spectral density (equation 4.6).

Equation (4.6) relates the STA and the beam spectrum. However, the inversion was applied to array-averaged single-channel spectra. Therefore, to use the derived attenuation model we need a relationship between the beam spectra and single-channel spectra. While beamforming produces close to $\sqrt{N}$ noise suppression (Figure 4.9), it also suppresses uncorrelated high-frequency signal energy. In Section 4.5 we will estimate the beam gain (defined as the ratio of the signal loss and noise suppression) to convert from single-channel to array detection capability.

4.4.2 Lg signal. Since Lg is a dispersed signal with a rapidly decaying spectrum, the assumptions involved in deriving (4.6) are invalid for this phase. Furthermore, Lg is detected on both coherent and incoherent beams, and these have quite different relationships between temporal and spectral amplitudes. Therefore, for Lg we will simply determine an empirical relationship between the array-averaged spectral amplitudes and the STAs.

Figure 4.13 plots the ratio of the STA and the array-averaged spectral amplitude at the filter center frequency. The mean value of the ratio is 0.32 for coherent beams, 1.02 for the lowest-frequency incoherent beam (1-2 Hz), and 1.13 for the higher-frequency incoherent beams (2-4 Hz). Since Lg is rarely detected with the maximum SNR on a horizontal beam, we only consider vertical beams in this section. Note that we do not observe any magnitude or range dependence in this ratio. This implies that the inversion results for the 5-s window Lg spectra adequately account for the magnitude and range dependence of the STAs.

Figure 4.13 suggests that we can predict the STA for an event of arbitrary distance and magnitude by simply dividing the predicted Lg spectrum for a 5-s window by a constant that depends only on the detecting beam. To verify this, we define the function

$$B(r) = \log A_{Lg}(f,r) - 1.16 M_L = 17.51 + \log\left[\frac{\kappa}{4\pi\rho_c\beta_c^3}G(r,r_0)\exp(-\pi f t/Q(f))\right] \qquad (4.7)$$

using (2.1) and (2.4)-(2.7). $A_{Lg}(f,r)$ is the array-averaged Lg spectrum computed for 5-s windows. The moment-magnitude relationship ($\log M_o = 1.16 M_L + 17.51$) is that derived from the inversion of these spectra [*Sereno et al.*, 1987]. $B(r)$ is plotted in Figure 4.14 for frequencies between 1 and 5 Hz. The individual points are the STAs corrected for beam type. The STAs were divided by the ratios determined from Figure 4.13 (listed in the previous paragraph). In general, there is good agreement between the array-averaged spectral amplitudes and the beam-corrected STAs.
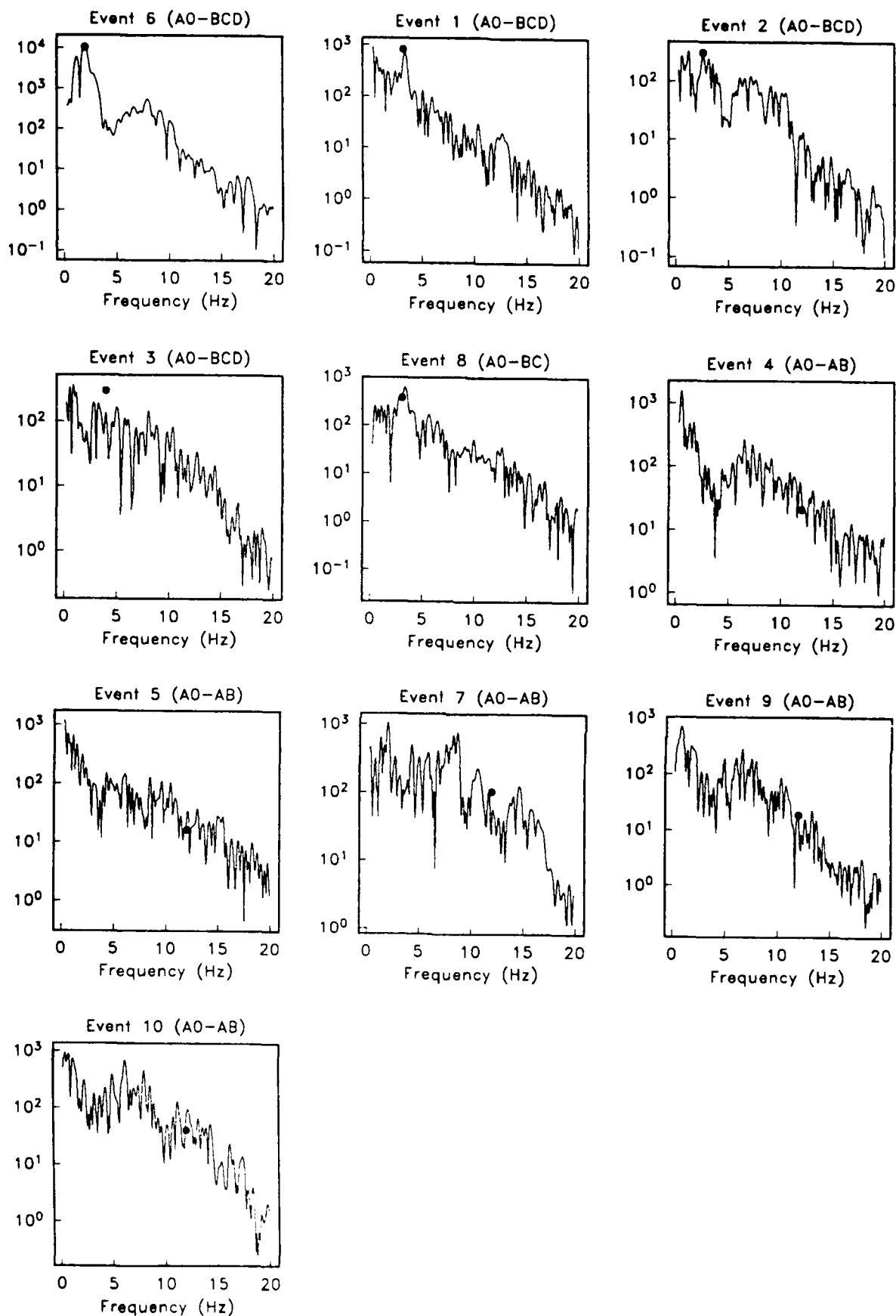
Figure 4.12. *Pn* beam spectra for the 10 events listed in Table 4.4. Each spectrum is labeled by event number and the sub-array used in beamforming. The small dot on each spectrum is STA/($\Delta f \delta$) for $\delta = 0.7$.

75

STA_Lg/(Array-Averaged Spectrum)
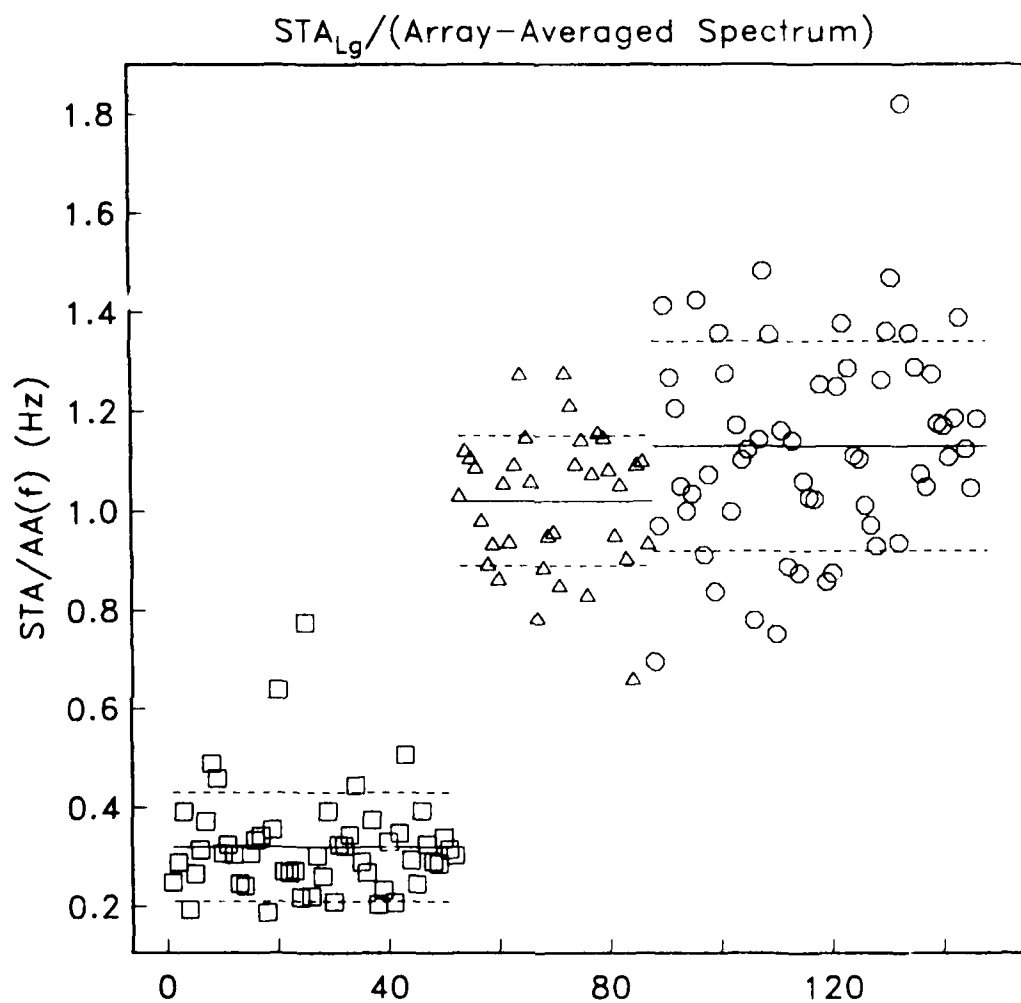
Figure 4.13. Ratio of Lg-STA and the array-averaged spectral amplitude at the filter center frequency of the beam with the maximum SNR. The spectra were computed for 5-s windows. The squares are detections on coherent beams and the triangles and circles are detections on incoherent beams. The triangles are detections on beam 18 (1-2 Hz), and the circles are detections on beams 19-20 (2-4 Hz). The mean ratio bounded by one standard deviation is plotted for each beam type.

Figure 4.14. The solid curves plot the Lg amplitude-distance function $B(r)$ defined by (4.7) at frequencies between 1 and 5 Hz. Each curve is labeled by frequency. The symbols are the Lg-ST/... corrected for the beam type. Note that there is good agreement between the amplitude-distance curves derived from the inversion and the observed time-domain amplitudes.

77

4.5 Beam Gain

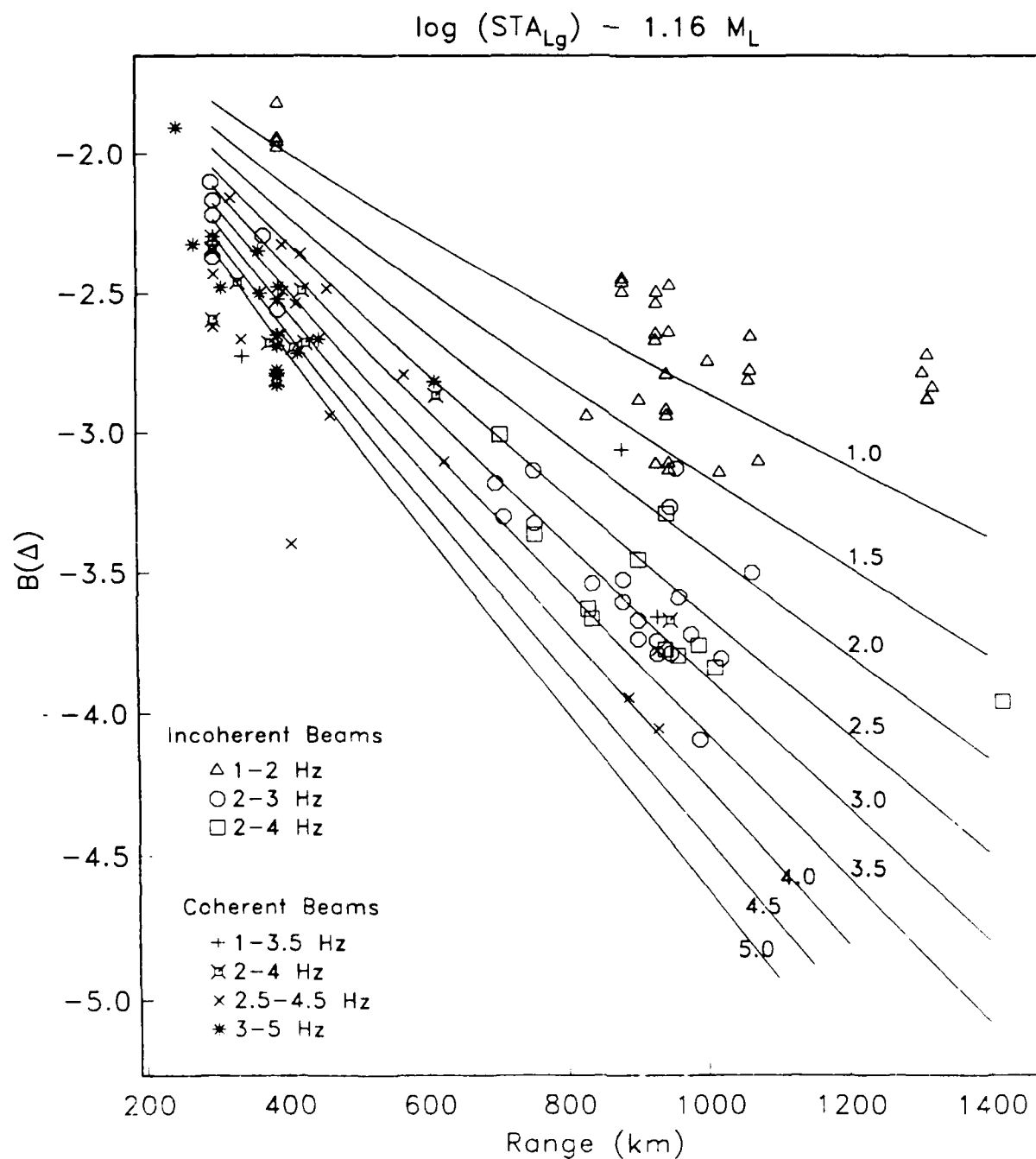Our primary objective here is to determine the relationship between the single-channel spectral amplitudes and the time domain amplitudes measured on filtered beams. In particular, we want to predict the STA/LTA as a function of distance, magnitude and frequency based on a parameterization of array-averaged spectra. To do this, we must address two separate issues. One is the relation between temporal and spectral amplitudes on filtered beams, and the other is the relation between beam spectra and single-channel spectra. In Sections 4.3.1 and 4.4.1 we addressed the first issue by expressing the Pn LTAs and STAs in terms of the beam spectral amplitudes. In this section we investigate the second issue which involves the determination of the frequency-dependent beam gain.

Using (4.2) and (4.6), the temporal SNR measured on a filtered beam can be expressed as

$$SNR_t = \frac{STA}{LTA} = \frac{A_B(f)}{N_B(f)} \, \delta \left[\frac{T\Delta f}{2} \right]^{1/2} \tag{4.8}$$

where the subscript B identifies beam spectra, A is the signal spectrum, N is the noise amplitude spectrum, and T is the time length used in the noise spectrum estimate (in this case, 5 s). We define the frequency-dependent beam gain as the ratio of the spectral SNR on the beam and the single-channel SNR. Specifically,

$$G(f) = \frac{A_B(f)/N_B(f)}{A(f)/N(f)} \tag{4.9}$$

where $A(f)$ and $N(f)$ are single-channel signal and noise spectra. Combining (4.8) and (4.9) we can express the time-domain SNR measured on a filtered beam in terms of the SNR of array-averaged single-channel spectra. Specifically,

$$SNR_t = \frac{STA}{LTA} = \frac{A(f)}{N(f)} \, \delta \, G(f) \left[\frac{T\Delta f}{2} \right]^{1/2} \tag{4.10}$$

The only term in (4.10) that we have not estimated is the beam gain, $G(f)$. From the observed SNR_t and our value for δ of 0.7 we can determine the average beam gain by rearranging (4.10)

$$G(f) = SNR_t \, \frac{N(f)}{A(f)} \, \delta \left[\frac{2}{T\Delta f} \right]^{1/2} \tag{4.11}$$

The frequency used in (4.9) is the filter center frequency, except for the highest-frequency beam where we use 10 Hz to calculate the noise spectra (Section 4.3.1) and the filter center frequency to calculate the signal spectra. Figure 4.15 plots the $G(f)$ for the four combinations of sub-array and filter bandwidth typical for Pn detections. The mean gain for each beam type is shown as the solid horizontal line. Table 4.5 summarizes the beam gain results.
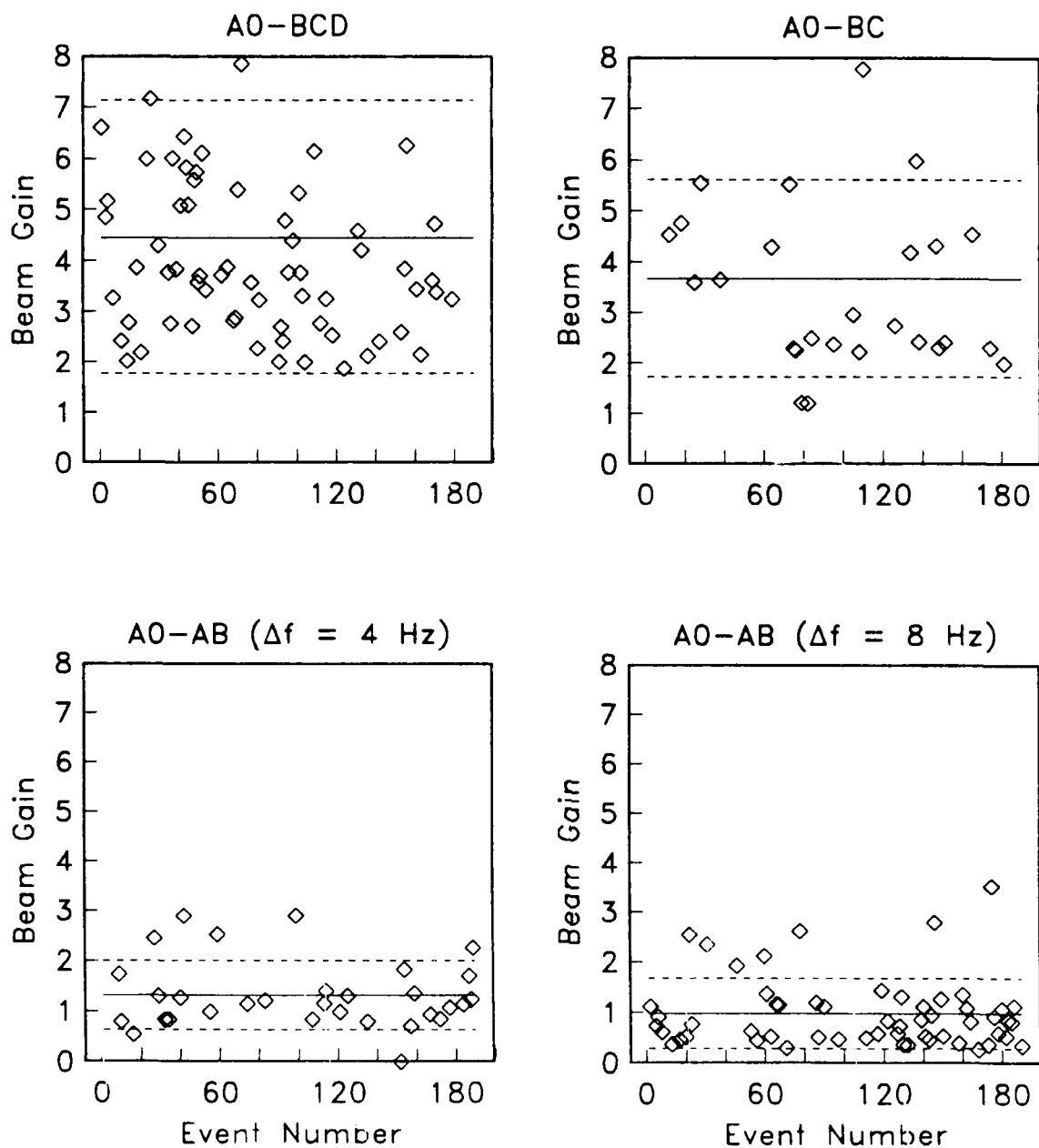
78

Figure 4.15. Beam gain defined by (4.11) with $\delta = 0.7$ for the four combinations of sub-array and frequency filter typical for *Pn* detection. The means are plotted bounded by one standard deviation. Note that the same axes scaling is used for all plots and that not all of the points used to determine the mean and standard deviation are shown.

79

Table 4.5. Beam gain.

Sub-array	Beam Numbers	Frequency	Δf	Detections	$\sqrt{N}$	$<G>$	σ^2
A0-BCD	8-16	2.0-5.0	2.0	68	4.7	4.45	7.18
A0-BC	4-5	2.5-5.0	2.0	27	3.6	3.68	3.82
A0-AB	6	4.0-8.0	4.0	31	3.0	1.31	0.46
A0-AB	7	8.0-16.0	8.0	56	3.0	0.98	0.48

For beams with center frequencies below 5 Hz, the beam gain is close to $\sqrt{N}$. However, the gains at higher frequency are near unity. This is consistent with regional beam gain spectra displayed by *Mykkeltveit et al.* [1985]. Note that the NORESS array was designed to enhance signal frequencies in the range 1.5-5.0 Hz [*Mykkeltveit*, 1983]. Thus, it is not surprising that the array does not offer enhanced SNR at higher frequencies. This simply means that the signal and the noise are both uncorrelated over the sub-array used in beamforming.

The gains listed in Table 4.5 depend on the value of δ, which is constrained by a relatively small dataset. To provide independent support for our gain estimates, we calculated beam gain spectra using (4.9) for the 10 events listed in Table 4.4. These are plotted in Figure 4.16. The solid horizontal line indicates a gain of one and the dashed horizontal line is plotted at $\sqrt{N}$. In general, the beam gain approaches $\sqrt{N}$ for frequencies less than 5 Hz, but for frequencies greater than 8 Hz the array offers very little improvement in signal-to-noise. The consistency of the beam gains listed in Table 4.5 with those in shown Figure 4.16 and those given by *Mykkeltveit et al.* [1985] provides independent support for our estimate of δ.
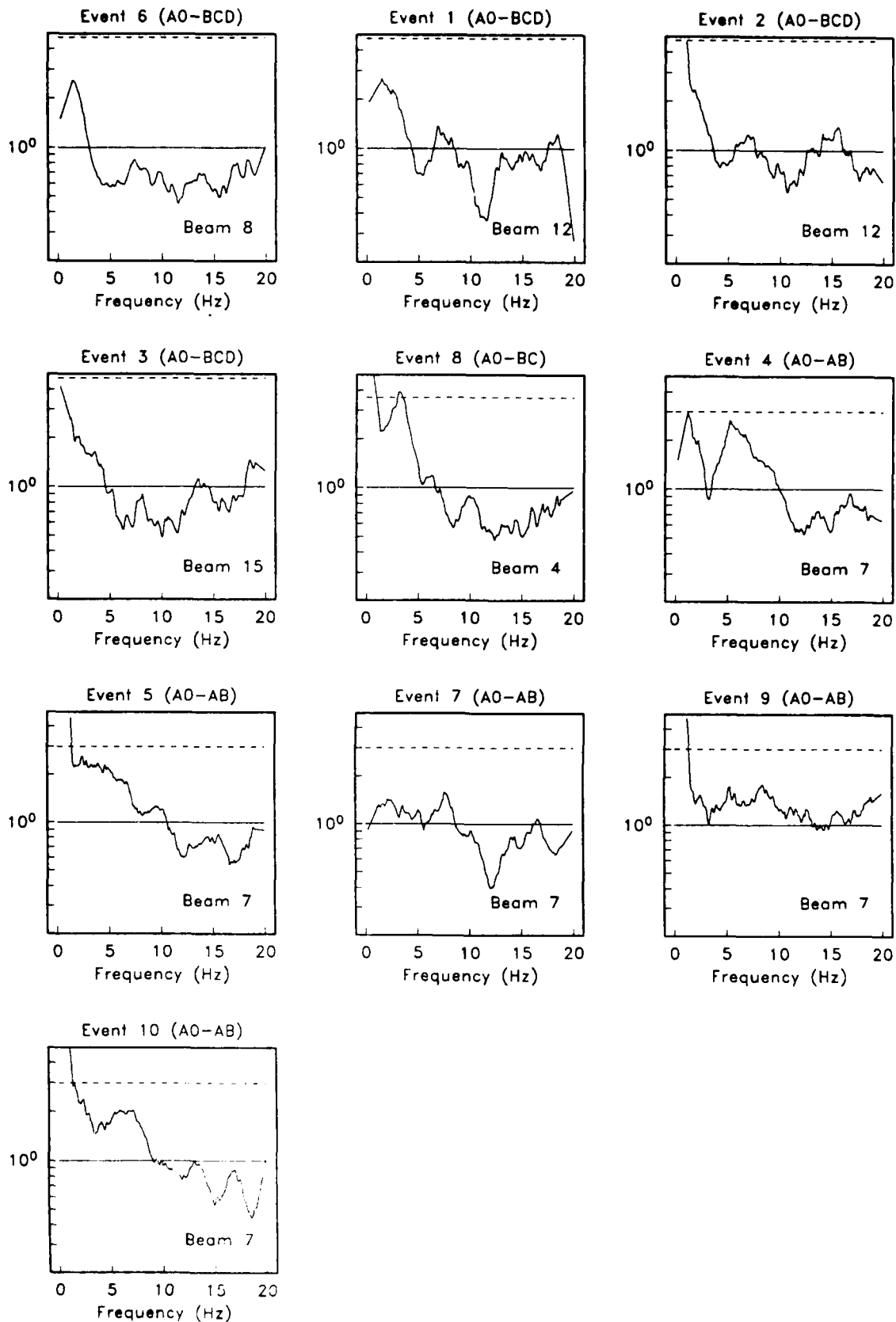
Figure 4.16. Beam gain spectra for *Pn* defined by (4.9) for the 10 events listed in Table 4.4. Solid horizontal lines indicate a gain of one and the dashed lines are plotted at $\sqrt{N}$. The signal and noise spectra were smoothed over 2 Hz prior to taking their ratio. The event numbers refer to Table 4.4 and each event is labeled by the sub-array used in beamforming.

4.6 Detectability

In the previous section we derived an expression for the SNR measured on a filtered beam in terms of the array-averaged spectral amplitudes used in our Pn inversion. In Section 4.4.2 we found a relationship between the STA and the array-averaged spectral amplitudes for Lg, and in section 4.3.2 we developed an empirical parameterization of Lg-LTA. Therefore, for a given magnitude and distance we can predict the frequency-dependent SNR for Pn and Lg based on our inversion results. In this section we estimate the NORESS detection capability directly from time-domain amplitudes and compare the results to the predictions based on our Q model.

The automatic detection of a seismic signal occurs when the STA/LTA exceeds a predetermined threshold. Since the beam thresholds are determined from false alarm statistics, dividing by the threshold provides a common basis for comparing the SNR measured on different beams [Kvaerna et al., 1988a]. We define the detectability, $D(r)$, as

$$D(r) = \log \left[\frac{SNR_t}{th} \right] - \alpha\, M_L \qquad (4.12)$$

where SNR_t is the maximum STA/LTA for all detecting beams, th is the beam threshold, and α is chosen such that $D(r)$ does not depend on the source. The value of α is close to one for Pn but much less than one for Lg because both the STA and the LTA depend on M_L. Assuming that both signal and noise are log normally distributed, the probability of detecting wave k from source j is

$$P_{jk} = \phi \left[\frac{D_k(r_j) + \alpha_k\, M_{Lj}}{\sigma_k} \right] \qquad (4.13)$$

where $\phi(x)$ is the Gaussian cumulative distribution function [e.g., Abramowitz and Segun, 1964; p. 931] and σ_k is the standard deviation of the detectability function. Of course, this is only a valid interpretation of (4.13) if $\alpha\, M_L$ adequately represents the source contribution to the SNR. That is, if α is frequency-independent then (4.13) represents the probability of detection below the source corner frequency.

4.6.1 Pn Detectability. Figure 4.17 plots the observed Pn detectability defined by (4.12) with $\alpha = 1.0$. Only explosions are used because the earthquake detectability can be biased by the unknown radiation pattern. That is, it is not possible to determine an α for earthquakes that effectively removes the source contribution to the SNR. We also excluded events with $M_L \geq 3.0$ that were detected on one of the two highest-frequency beams (beams 6 and 7, Table 4.1) because their corner frequencies are expected to be within the filter bandwidth. The logarithmic decay of the Pn detectability is approximated by

$$D(r) = 3.42 - 1.93 \log r \qquad (4.14)$$

where the coefficients were obtained by least-squares. This is plotted in Figure 4.17 bounded by one standard deviation ($\sigma = 0.31$). The observations are plotted with different symbols

82
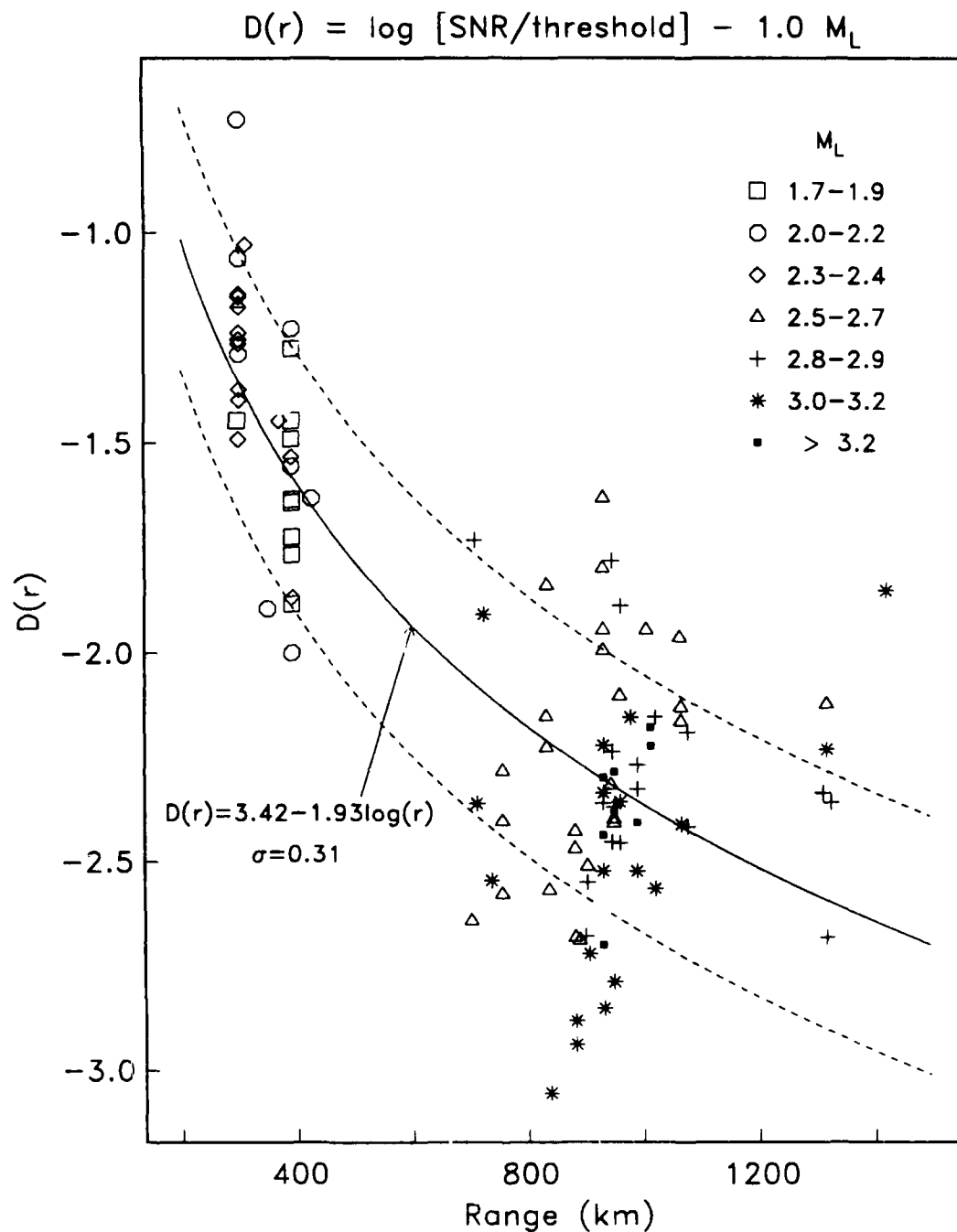
Figure 4.17. *Pn* detectability defined by (4.12) with α = 1.0 for 102 explosions. Seven events were excluded with $M_L \geq 3.0$ because their corner frequencies are expected to be within the filter bandwidth. Different symbols are used depending on event magnitude. The curve is the logarithmic parameterization of $D(r)$ bounded by one standard deviation. Since the event magnitudes are well-distributed about the parameterized detectability, we conclude that α = 1.0 adequately represents the source scaling for these events.

according the event magnitude. If the source contribution is effectively removed then the detectability should not depend on magnitude, provided the measurements are taken below the corner frequency. However, if α is too large then the detectability will decrease with increasing magnitude and a value that it is too small will produce the opposite magnitude-dependence. Table 4.6 examines the magnitude-dependence of the detectability as a function of α. Listed are the average magnitudes of events above and below the logarithmic parameterization of $D(r)$ in each of two distance ranges. The number of events in each category is given under the column heading N. The explosion moment-magnitude relation derived from the inversion gives $\alpha = 1.08$. However, Table 4.6 shows that this α gives an average magnitude above $D(r)$ that is about 0.1 lower than that below $D(r)$ for ranges greater than 700 km (suggesting that α = 1.08 is too large). Setting $\alpha = 1.0$ reduces the magnitude-dependence of $D(r)$ at long ranges without increasing it at shorter ranges. Since this value of α is consistent with theoretical explosion source scaling models and only slight improvement in reducing the magnitude-dependence of $D(r)$ at long ranges is offered by $\alpha = 0.9$, we use $\alpha = 1.0$ for the Pn detectability.

Table 4.6. Pn detectability.

| α | $D(r)$ | σ | < 700 km | | | | > 700 km | | | |
| | | | above $D(r)$ | | below $D(r)$ | | above $D(r)$ | | below $D(r)$ | |
			N	$<M_L>$	N	$<M_L>$	N	$<M_L>$	N	$<M_L>$
1.08	3.55-2.05log(r)	.32	19	2.20	12	2.09	32	2.83	39	2.94
1.00	3.42-1.93log(r)	.31	19	2.20	12	2.09	34	2.88	37	2.91
0.90	3.26-1.78log(r)	.31	19	2.21	12	2.08	34	2.90	37	2.89
0.80	3.09-1.62log(r)	.31	18	2.26	13	2.02	35	2.93	36	2.86

The 50% magnitude detection threshold for Pn based on (4.14) with $\alpha = 1.0$ is 1.6 at 400 km and 2.4 at 1000 km. Our results compare favorably to those of Ringdal [1986] who estimated Pn detection capability by comparing the NORESS detections to bulletins produced by local seismic networks in Fennoscandia. He obtained a 50% detection threshold of $M_L = 2.3$ between 700 and 1400 km. Since the two methods differ markedly, their agreement provides support to our parameterization of Pn detectability.

The method described above provides simple and accurate estimates of the Pn detectability of regional arrays equipped with automatic array-processing software. Another question is how to extrapolate these results to other areas of estimated attenuation. For example, how would the NORESS array performance change if it were placed in a region of lower Pn attenuation? To answer this question it is necessary to relate the observed temporal SNRs to the single-channel spectral SNR for which we have a parameterization in terms of Pn attenuation. In section 4.5, we derived such a relation. That is, using our spectral parameterization of the single-channel spectrum $A(f)$ and the average noise spectrum $N(f)$, we can predict the

detection capability of specific beams using (4.10). In this section we compare these predicted values with the observed detection capability.

The predicted SNR is computed using (4.10) with $\delta = 0.7$, the beam gains listed in Table 4.5, a noise window length $T = 5$ s, and the filter bandwidths listed in Table 4.1. The detectability is estimated by dividing the predicted SNR by the beam threshold and subtracting αM_L. For frequencies less than the source corner frequency the logarithm of the array-averaged signal spectrum, $A(f)$, can be expressed as

$$\log A(f,r) = \alpha M_L + B(r) \tag{4.15}$$

where

$$\log M_0 = \alpha M_L + I$$
$$B(r) = I + \log \left[\frac{1}{4\pi\rho_s\alpha_s^3} \ G(r,r_0) \ \exp(-\pi f t/Q(f)) \right] \tag{4.16}$$

As discussed in Section 2, a suite of Pn models produce data variances that differ by only a few percent. In this section we found that $\alpha = 1.0$ effectively removed the magnitude-dependence of the detectability function. Therefore, rather than using the "preferred model" of Section 2, for comparative purposes we select the Pn attenuation model consistent with $\alpha = 1.0$. Note, however, that nearly equivalent results for detection capability are obtained using the "preferred model" and $\alpha = 1.08$. The relevant Pn parameters for $\alpha = 1.0$ are $I = 17.64$ and $Q(f) = 435f^{0.42}$. The other terms in (4.16) are the same as those discussed in Section 2. Combining (4.10), (4.12), and (4.15), the predicted detectability can be written as

$$D(r) = B(r) - \log N(f) + \log \left[G \ (T\Delta f /2)^{1/2} \ \delta \right] - \log th \tag{4.17}$$

where the amplitude-distance function $B(r)$ is calculated at the filter center frequency and $N(f)$ is obtained from the average NORESS ambient noise computed for a 5 s window [Henson and Bache, 1988]. The noise is evaluated at the filter center frequency, except for the highest-frequency beam (beam 7) for which we use 10 Hz (Section 4.3.1). Note that the predicted Pn spectrum at ranges less than 700 km decays less rapidly than the noise spectrum beyond 8 Hz. This suggests that the Pn detection capability of beam 7 could be improved by filtering at higher frequency. This is confirmed by Kvaerna et al. [1988b] who compiled detection statistics for events in western Norway. Most of their events were at ranges less than 450 km. They found that 60% of their Pn detections occurred with the maximum SNR on a 10-16 Hz beam while only 4% occurred on the 8-16 Hz beam.

Figure 4.18 compares the predicted and observed Pn detectability for events with the maximum SNR on beams 4, 5, 6 and 7. Although the predicted frequency of the maximum SNR is greater than 10 Hz for distances less than 800 km (Figure 4.4), the predicted frequency of optimal detectability is much less than this. This is because the SNR advantage at high frequency is erased by a lower beam gain. As a result, our model predicts greater detection capability on beams 4 and 5 (2.5-5 Hz) than on the higher-frequency beams for ranges greater than about 400 km. Considering uncertainties in beam gain, δ, and the appropriate dominant
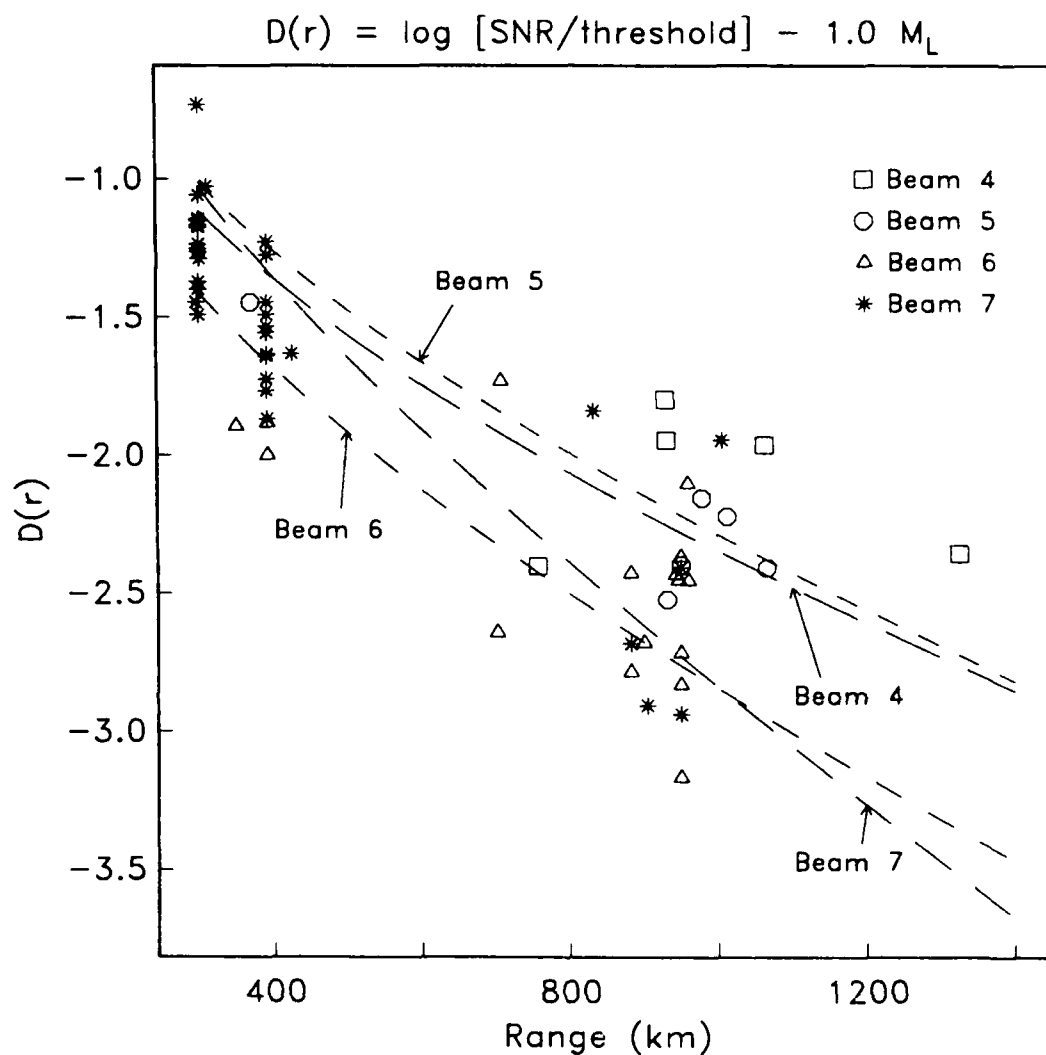
Figure 4.18. Comparison of predicted and observed *Pn* detectability for beams 4-7. The observations are plotted with different symbols depending on beam number. Beams 4 and 5 are formed over the A0-BC sub-array and beams 6 and 7 are formed over AB (Figure 4.2). The frequency filters applied to beams 4-7 are 2.5-4.5 Hz, 3.0-5.0 Hz, 4.0-8.0 Hz, and 8.0-16.0 Hz respectively. The predicted detectability curves are labeled by beam number.

frequency for a given detection, the model does an adequate job of predicting the detectability of specific beams. However, the model is inadequate for predicting which beam should provide the greatest SNR at a given distance. For example, the predicted detectability of beam 4 exceeds that of beams 6 and 7 by a factor of 3 between 800-1000 km. However, the observations show that there are as many Pn detections on beams 6-7 as there are on beams 4-5 in this distance range, even though the SNRs are consistent with the model. A likely explanation for the inconsistency is that spectral modulation caused by ripple-firing with delays between 150-250 ms consistently suppresses amplitudes less than 4-5 Hz for mine blasts [*Baumgardt and Zeigler*, 1987]. In many cases our Q model correctly predicts the high frequency (> 5 Hz) Pn amplitude of these events, but overestimates the spectral level between 2-5 Hz (Appendix A). Since the time lags that produce 4-5 Hz spectral modulations are consistent with the destructive interference of multiple explosions, we interpret this as an unmodeled source complexity rather than a path effect. This would argue that the Pn detection capability of mine blasts at long ranges is overestimated by our model. If this interpretation is correct, it also implies that our empirical $D(r)$ underestimates the detection capability for sources with uncomplicated time histories.

4.6.2 Lg detectability. Both the signal and noise levels for Lg depend on magnitude. Therefore, the α that removes the M_L dependence from the detectability is equal to the difference in slopes of the log moment-magnitude and log LTA-magnitude relations. From the results of Section 4.3.2, we expect that the appropriate value of α is close to 0.2. Figure 4.19 plots the observed Lg detectability for $\alpha = 0.2$. We include both earthquakes and explosions since Lg amplitude is relatively insensitive to source radiation pattern. The logarithmic decay of the Lg detectability for $\alpha = 0.2$ is approximated by

$$D(r) = 1.42 - 0.64 \log r \qquad (4.18)$$

where the coefficients were obtained by least-squares. This is plotted in Figure 4.19 bounded by one standard deviation curves ($\sigma = 0.12$). The observations are plotted with different symbols depending on the event magnitude. Note that for this value of α there is no obvious magnitude dependence in $D(r)$.

Figure 4.20 plots the Lg detectability assuming $\alpha = 1.0$. The obvious magnitude-dependence in $D(r)$ confirms our assertion of a magnitude-dependence in the Lg-LTA. Table 4.7 identifies the magnitude-dependence of the Lg detectability as a function of α. The slope of the explosion moment-magnitude relation derived from the inversion of the Lg spectra computed for fixed 5-s windows is 1.16. Combined with the M_L dependence of the LTA, this suggests $\alpha = 0.36$. However, this value of α gives a bias in the average M_L above and below the parameterization of $D(r)$ of 0.3-0.4. Smaller values of α reduce both the magnitude-dependence and variance of $D(r)$. We use $\alpha = 0.20$ to describe Lg detectability because it is consistent with the log moment-magnitude relation used for Pn and the observed magnitude dependence of the LTA.
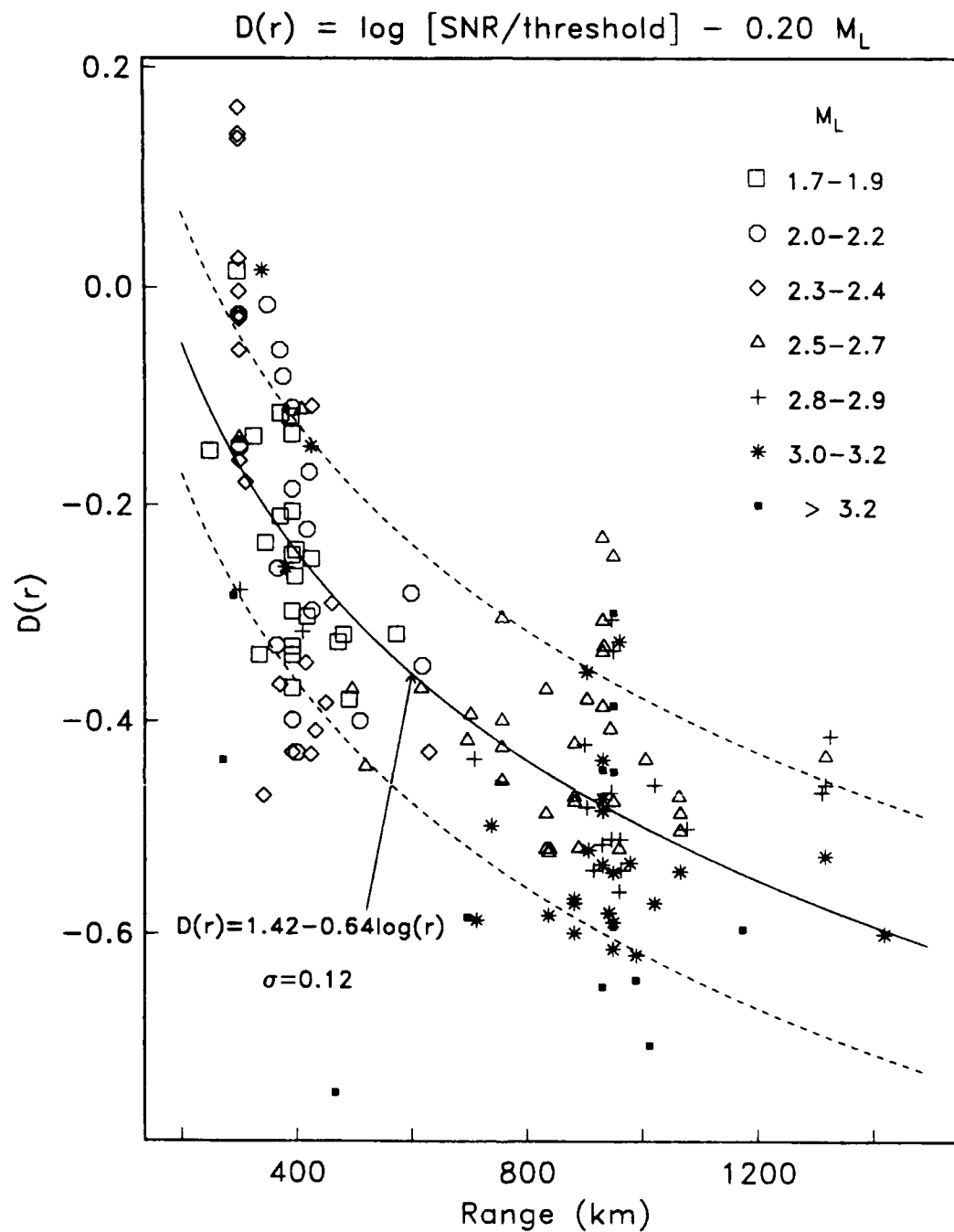
Figure 4.19. *Lg* detectability defined by (4.12) with $\alpha = 0.2$ for 157 events. Events were excluded only if a NORESS M_L was not available. Both earthquakes and explosions are included. Different symbols are used depending on event magnitude. The curve is the logarithmic parameterization of $D(r)$ bounded by one standard deviation. Note that there is no obvious magnitude dependence of $D(r)$.
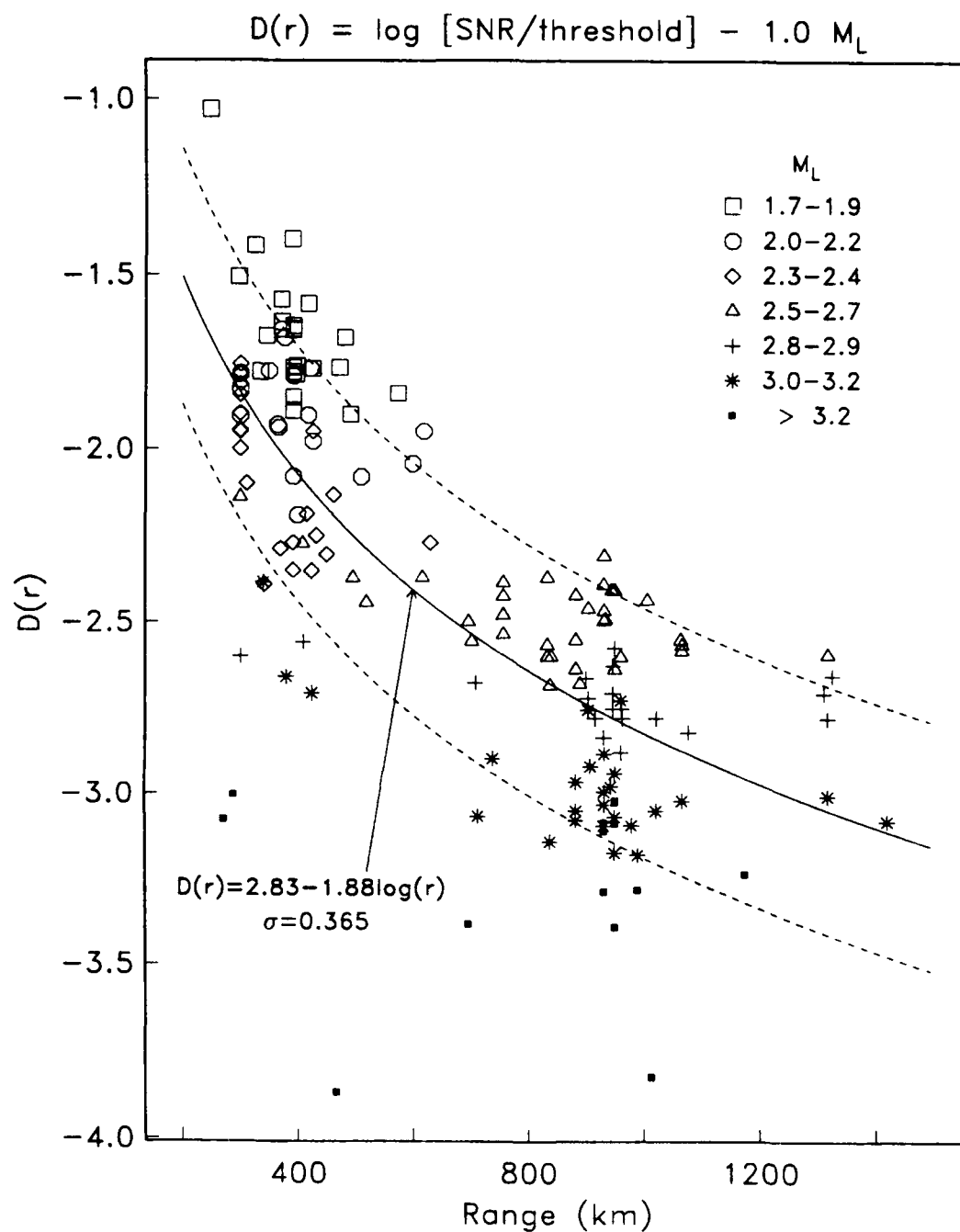
88

Figure 4.20. *Lg* detectability defined by (4.12) with $\alpha = 1.0$ for 157 events. Different symbols are used depending on event magnitude. The curve is the logarithmic parameterization of $D(r)$ bounded by one standard deviation. The obvious magnitude dependence of $D(r)$ indicates that $\alpha = 1.0$ is too large.

89

Table 4.7. *Lg* detectability.

α	D(r)	σ	< 700 km				> 700 km			
			above D(r)		below D(r)		above D(r)		below D(r)	
			N	$<M_L>$	N	$<M_L>$	N	$<M_L>$	N	$<M_L>$
1.00	2.83-1.88log(r)	.37	48	1.99	30	2.62	43	2.71	36	3.13
0.36	1.70-0.89log(r)	.15	45	2.05	33	2.48	38	2.75	41	3.04
0.20	1.42-0.64log(r)	.12	36	2.17	42	2.29	38	2.82	41	2.97
0.10	1.25-0.49log(r)	.12	32	2.31	46	2.18	36	2.84	43	2.95

The 50% magnitude detection thresholds for *Lg* with α = 0.2 at 400 and 1000 km are 1.2 and 2.5 respectively. We are unaware of independent studies to use as a basis for comparison. However, *Ringdal* [1986] estimated 50% and 90% magnitude detection thresholds in the distance range 700-1400 km for *P* waves only and for at least one of the phases *P*, *Sn*, or *Lg*. We have not studied the detectability of *Sn*, so we cannot directly compare our secondary phase results to his. However, we can calc late the 50% and 90% thresholds for detection of either *P* or *Lg*. Since the addition of *Sn* can only improve the detectability, this gives an upper bound on the detection thresholds considered by *Ringdal*. Table 4.8 summarizes the results. In general, the two methods produce consistent results for the regional wave detection capability of the NORESS array.

Table 4.8. Regional wave detection capability at NORESS.

Phase	50% Threshold		90% Threshold	
	this study	*Ringdal* [1986]	this study	*Ringdal* [1986]
P only	2.4	2.3	2.8	2.7
Lg only	2.5	---	3.3	---
P or Secondary Phases	2.2†	1.9	2.6†	2.5

† This study uses *Lg* as the only secondary phase, *Ringdal* [1986] used *Sn* or *Lg*.

The problem of extrapolating the NORESS results to other regions is more complicated for *Lg* than for *Pn* for several reasons. First, we don't have a single-channel parameterization of the pre-*Lg* noise spectrum. As demonstrated earlier, the pre-*Lg* noise is a complicated function of distance, magnitude and frequency. Second, the relation between time and frequency domain amplitudes is complicated by dispersion. If we were to parameterize the *Lg* SNR as in

(4.10), the function δ could be both range- and frequency-dependent. Third, the inversion results are sensitive to the window length used to compute the Lg spectra (Table 2.7). Therefore, it is important to know how the Q_{Lg} was obtained for other areas of interest and its relationship to the Lg spectra used in the inversion. For example, in Section 4.4.2 we showed that the Lg-STA can be expressed in terms of the array-averaged spectrum computed for 5-s windows as

$$\log STA = \log K_B + \log A(f,r) \qquad (4.19)$$

were K_B is a constant that depends only on beam type. This implies that the relationship between the STA and FGV spectra must be range-dependent, since the difference between the 5-s and FGV spectra is range-dependent. Of course, this is anticipated because the time and frequency domain geometric spreading rates are not equal for dispersed phases. In this section we demonstrate that the observed Lg detectability can be predicted from the inversion results for spectra computed for 5-s windows. However, we note that Q_{Lg} estimated in this way is not available for other regions. Table 2.7 can be used as a guide to determine Q_{Lg} for 5-s windows from estimates based on longer time windows, but clearly it would more desirable to parameterize the Lg SNR in a form similar to that used for Pn. This is a topic that will require further study.

Combining (4.19) and (4.3), we can express the time domain SNR for Lg as

$$\log SNR = (\log K_B - b) + (a - \gamma)M_L + B(r) - (A_0 + d(r) + F(f)) \qquad (4.20)$$

where

$$\log M_0 = aM_L + I$$

$$B(r) = I + \log\left[\frac{\kappa}{4\pi\rho_c\beta_c^3} G(r,r_0) \exp(-\pi ft/Q(f))\right] \qquad (4.21)$$

To calculate $B(r)$ we use the model within the Lg parameter trade-off that gives $a = 1$. The relevant parameters are $I = 17.78$, $Q(f) = 430f^{0.34}$, and $a - \gamma = 0.2$. The other terms are the same as those defined in Section 2. From (4.21) and (4.12), the predicted Lg detectability is

$$D(r) = \log(K_B/th) - b + B(r) - (A_0 + d(r) + F(f)) \qquad (4.22)$$

The first two terms depend only on beam type, the third term is the amplitude-distance curve for the single-channel Lg spectrum, and the last term is the magnitude-independent part of the Lg noise. The constants in (4.22) as a function of beam number are given in Table 4.9 for the beams that most frequently detect Lg with the maximum SNR. Note that the first two terms in (4.22) combine to nearly a constant value for all beams. This means that the relationships we have derived between coherent and incoherent beam amplitudes are consistent with the detection thresholds determined from false alarm statistics [Kvaerna et al., 1988a].

91

Table 4.9. Constants for the predicted *Lg* detectability.

Beam	K_B	*th*	*b*	Frequency	A_0	$F(f)$
18	1.02	2.5	0.0	1.0-2.0	-2.27	0.62
19	1.13	2.5	0.0	2.0-3.0	-2.27	0.0
20	1.13	2.1	0.0	2.0-4.0	-2.27	0.0
8-10	0.32	4.0	-0.78	2.0-4.0	-2.27	0.0
11-13	0.32	4.0	-0.78	2.5-4.5	-2.27	0.0
14-16	0.32	4.0	-0.78	3.0-5.0	-2.27	0.0

To calculate the predicted detectability at fixed frequency it is necessary to have a continuous function $d(r)$ describing the *Sn* coda decay rate. We assume that the *Sn* coda decays exponentially and associate the two estimates of $d(r)$ given in Section 4.3.2 with ranges of 400 and 1000 km. The result is

$$d(r) = 0.43 - 0.0025 \log(e) \, r \tag{4.23}$$

which is approximately valid over the distance range of our data. Figure 4.21 plots the predicted and observed *Lg* detectability for beams 18-20 and for coherent beams. For beam 18 we find that a frequency of 1.0 Hz is consistent with the observed detectability. For the other incoherent beams we use the filter center frequency. Since the constants are the same for all of the coherent beams, we simply plot the predicted $D(r)$ for three frequencies spanning the band covered by the steered beams. The overall agreement between the observed and predicted detectability is quite good. However, to a large extent the "model" is based on an empirical relationship for the LTA which cannot be extrapolated with confidence to other regions or to distances greater than about 1400 km.

$$D(r) = \log [SNR/threshold] - 0.20\ M_L$$

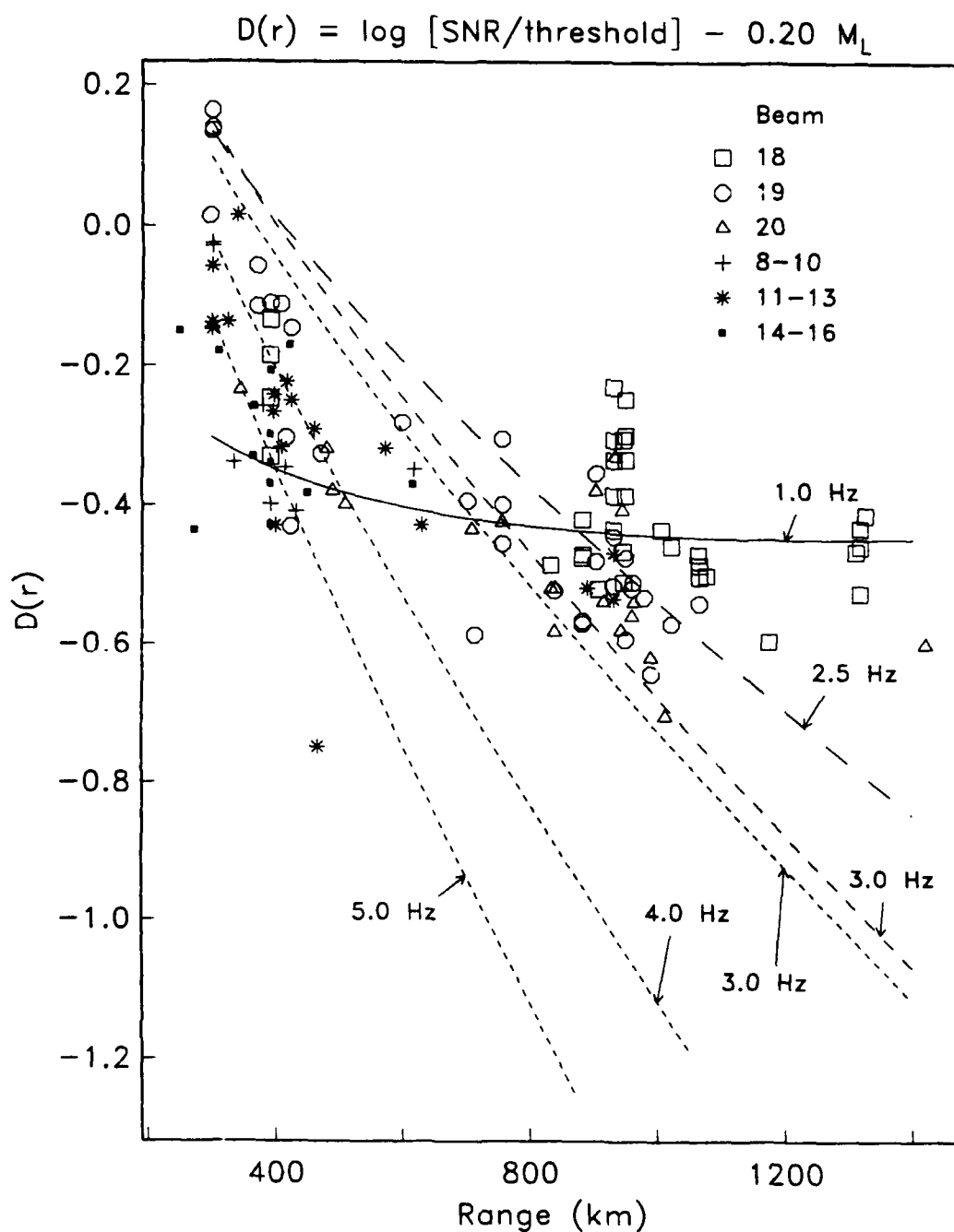Figure 4.21. Comparison of predicted and observed *Lg* detectability for beams 18-20 (incoherent vertical beams) and 8-16 (coherent beams formed over the full array). Different symbols are used depending on beam number. The predicted detectability for the coherent beams at 3.0, 4.0, and 5.0 Hz are plotted as finely dashed curves. The other curves represent the *Lg* detectability of beams 18 (1.0 Hz), 19 (2.5 Hz), and 20 (3.0 Hz).

5. SUMMARY

The objectives of this research are to (1) determine an accurate parameterization of single-channel regional wave spectra recorded at NORESS and, (2) determine the relationship between these spectral amplitudes and the time domain amplitudes measured on filtered beams used in signal detection. From this relationship, it is possible to extrapolate the NORESS detection capability to other areas of estimated attenuation and/or to other array performance enhancement capabilities.

The primary conclusions of our spectral analysis
are as follows:

1. Data from all 186 regional events are adequately represented by a single frequency-dependent Q model. However, we note that no events with travel paths crossing the Central Graben of the North Sea are included. Severe Lg blockage has been noted for these paths by other investigators [e.g., *Kennett and Mykkeltveit*, 1984]. Theoretical spectra derived from our simple parameterization were compared to 312 observed regional wave spectra, and good agreement was seen. The ability of the model to reproduce the important spectral characteristics of such a large number and variety of observed data provides the primary support for our methodology and results.

2. We have found that regional Pn spectra of 152 events are consistent with $r^{-1.3}$ geometric spreading and $Q_{Pn}(f) = 325f^{0.48}$. We do not attempt to distinguish intrinsic absorption from scattering and explicitly acknowledge that our $Q(f)$ is an empirical parameterization of the data. The Pn spectra are not sensitive to window length.

3. Regional Lg spectra are adequately represented from 1 to 7 Hz by a power law frequency dependence of apparent attenuation given by $Q(f) = 560f^{0.26}$. These spectra are computed over a fixed group velocity range of 3.6–3.0 km/s. Our $Q_{Lg}(f)$ is an approximation to the average Q_β of the crust, although it includes the effects of apparent attenuation due to scattering. These results were obtained assuming cylindrical spreading beyond a transition distance of 100 km.

4. The inversion results for Q_{Lg} are sensitive to window length. The inversion of spectra for fixed time windows of 5-s and 17-s gives $Q_{Lg}(f) = 350f^{0.41}$ and $Q_{Lg}(f) = 470f^{0.32}$, respectively. We interpret this higher apparent attenuation as a result of selectively excluding lower group modes at long ranges from the fixed time windows.

5. Since Lg is a secondary phase, the pre-Lg noise includes the coda of all previously arriving phases. Based on a comparison of pre-Lg and Lg spectra, we find that the Lg spectra are contaminated by Sn coda for frequencies greater than about 10 Hz for distances between 300–400 km and for frequencies greater than 3-6 Hz at ranges greater than 700 km. Therefore, we inverted the Lg spectra over a 1–3 Hz band to estimate the upward bias in Q_{Lg}

introduced by *Sn* coda. The result is $Q_{Lg}(f) = 582f^{0.18}$ compared to $560f^{0.26}$ for the 1–7 Hz bandwidth. Assuming that *Sn* coda does not affect the *Lg* spectrum for frequencies less than 3 Hz, the difference between Q estimated over 1–3 Hz and 1–7 Hz is an upper bound on the *Sn* coda bias.

6. We plot our estimated seismic moments versus local magnitude and obtain results that are generally consistent with those from near-field studies. Since magnitude does not enter the inversion, this lends considerable support to the derived Q model. Our corner frequency estimates also agree with those from near-field studies, although they are not clearly resolved by our data.

7. For a fixed set of source and spreading assumptions the inversion defines a broad minimum in the data residuals corresponding to a suite of models that fit the data equally well in a least squares sense. However, an important constraint on the attenuation estimates is the consistency of the derived source parameters from the independently inverted *Pn* and *Lg* spectra. This provides a good internal consistency check on our attenuation results and reduces the trade-offs among model parameters to trade-offs among sets of model pairs. That is, for fixed $Q_{Lg}(f)$ the source constraint places tight bounds on $Q_{Pn}(f)$. A trade-off between M_0-M_L variance and data variance is used to define the range of acceptable model pairs. The "preferred model" was selected from the midrange of these acceptable solutions. The range of acceptable Q_{Lg} models consistent with the data has Q_0 between 420 and 570 and η between 0.36 and 0.26. Similarly, for Q_{Pn} (assuming $r^{-1.3}$ spreading), the range has Q_0 between 200 and 500 with η between 0.59 and 0.40.

8. The $Q_{Lg}(f)$ results are insensitive to the details of our source parameterization because most inverted events have apparent corner frequencies outside the bandwidth considered. The $Q_{Pn}(f)$ trades off with the source parameterization. For example, a spectral decay faster than f^{-2} above the corner frequency must be accompanied by a higher Q_{Pn} to preserve the fit at high frequency. Therefore the derived Q_{Pn} function must be considered relative to our assumed source model.

9. *Pn* geometric spreading rates of r^{-1}, $r^{-1.3}$, and $r^{-1.5}$ were explicitly investigated, and for each there is a Q model that can adequately reproduce the *Pn* spectra. However, geometric spreading rates much different from $r^{-1.3}$ give earthquake to explosion *Lg* excitation ratios which are inconsistent with well-supported empirical observations.

10. The *Lg* and *Pn* attenuation models are used to predict range-dependent spectral amplitudes for events of arbitrary magnitude. The NORESS *Pn* observations are inconsistent with the $Q_\alpha = 9000$ proposed by *Evernden et al.* [1986] for the Russian platform and do not support their contention of enhanced detection capability at high frequency.

The primary conclusions of our temporal analysis
are as follows:

1. The maximum SNR for *Pn* occurs at a frequency greater than 8 Hz for distances less than 400 km and between 3-5 Hz in the 700-1000 km distance range. *Lg* is rarely detected with the maximum SNR above 4 Hz. At ranges less than 800 km, the *Lg* maximum SNR is between 2.5-4 Hz and at longer ranges it is between 1-3 Hz. These observations compare favorably with predictions based on the Q_{P_n} and Q_{L_g} models derived from the inversion.

2. The *Pn* SNR measured in the time domain on a filtered beam can be expressed in terms of the array-averaged single-channel spectra used in the inversion as

$$SNR_t = \frac{STA}{LTA} = \frac{A(f)}{N(f)} \, \delta \, G(f) \left[\frac{T\Delta f}{2} \right]^{1/2} \tag{5.1}$$

where $A(f)$ is the single-channel signal spectrum, $N(f)$ is the single-channel noise spectrum computed for window length T, $\delta \approx 0.7$, $G(f)$ is the beam gain, and Δf is the filter bandwidth. This equation can be used to predict the *Pn* detection capability based on a parameterization of single-channel spectra and to extrapolate the NORESS results to other areas of estimated attenuation.

3. Coherent beam gains are close to $\sqrt{N}$ (N is the number of array elements used in beam-forming) between 2-5 Hz but are close to one at higher frequency for the NORESS standard beams. This simply means that at high frequency both signal and noise are uncorrelated over the sub-array used in beamforming. Thus, although the frequency of the maximum SNR for single channels is greater than 8 Hz at distances less than about 400 km, the frequency of optimal detection is considerably less than this.

4. In general, the SNR cannot be predicted with (5.1) and a spectral parameterization of the signal and noise at the same frequency unless narrow band filters are used in beamforming. For example, we find that for the 8-16 Hz beam, the STA is consistent with the single-channel spectrum at 12 Hz, but the LTA is consistent with the noise spectrum at 10 Hz. This implies that the detectability of that beam could be improved at short ranges by filtering at higher frequency. This is confirmed by the recent work of *Kvaerna et al.* [1988b].

5. Comparison of observed and predicted detectability verifies that (5.1) can be used to predict the detection capability of specific beams. However, the model is inadequate in predicting which beam should provide the best SNR for mine blasts recorded at long ranges. We interpret this as an indication that our parameterization does not account for spectral modulation due to ripple-firing. The destructive interference of multiple explosions with approximately 150 ms time lags reduces the 4-5 Hz amplitudes, causing an upward shift in the frequency of the maximum SNR. If this interpretation is correct, our *Pn* inversion results overestimate the detection capability for ripple-fired mine blasts.

6. The relationship between the single-channel Lg spectrum and the STA is obscured by dispersion and Sn coda. For example, the relationship between time and frequency domain amplitudes depends on the window length used in Fourier analysis. In addition, we don't have a simple parameterization for single-channel pre-Lg noise. Therefore, we have not parameterized the Lg SNR in the same form as that used for Pn (5.1). Rather, we determined empirical relationships for the STA in terms of the array-averaged spectral amplitudes computed for 5-s windows, and the LTA as a function of magnitude, distance, and frequency. Using these relations, we can predict the temporal SNR on a filtered beam given the spectral parameterization of Lg. We note, however, that this is of limited practical use since Q_{Lg} estimates from spectra computed in this way are not available for other regions. This is an area that will require more research.

7. The Lg-LTA is a complicated function of magnitude, distance, frequency, and beam type. We have empirically parameterized the Lg-LTA in terms of these variables. The Lg-LTA decreases with both frequency and epicentral distance. The logarithm of the Lg-LTA increases with increasing M_L at an approximate rate of $0.8M_L$. As a result, the Lg SNR is not as strongly dependent on magnitude as the Pn SNR. We note, however, that this parameterization is preliminary and cannot be extrapolated with confidence to other regions or to distances beyond about 1400 km.

8. We define the regional wave detectability as the temporal SNR normalized by the beam threshold and corrected for the source amplitude. We parameterize the observed detectability by a simple logarithmic decay. Our results indicate that the 50% and 90% magnitude detection thresholds for Pn are 1.6 and 2.0 at 400 km and 2.4 and 2.8 at 1000 km. For Lg the 50% and 90% detection thresholds are 1.2 and 2.0 at 400 km and 2.5 and 3.3 at 1000 km. To the extent comparisons are possible, our results agree with those of *Ringdal* [1986] who used a considerably different method to estimate the regional wave detection capability of NORESS.

ACKNOWLEDGEMENTS

REFERENCES

Aki, K., and P. Richards, *Quantitative Seismology: Theory and Methods*, W. H. Freeman, San Francisco, Calif., 1980.

Abramowitz, M., and I. Segun, *Handbook of Mathematical Functions*, U.S. National Bureau of Standards, Washington, D. C., 1964.

Bache, T., P. Marshall, and L. Bache, Q for teleseismic P waves from central Asia, *J. Geophys. Res., 90*, 3575–3587, 1985.

Baumgardt, D., and K. Ziegler, Spectral evidence for source multiplicity in explosions, ENSCO, Inc. *Semi-Annual Technical Report SAS-TR-87-01*, AFGL-TR-87-0045, ADA187363, January 1987.

Bennett, T., J. Murphy, H. Shah, and B. Barker, Theoretical analysis of regional phase behavior, *Tech. Rep. SSS-R-87-8113*, Sys., Sci. and Software, La Jolla, Calif., 1987.

Brune, J., Tectonic stress and the spectra of seismic shear waves from earthquakes, *J. Geophys. Res., 75*, 4997–5009, 1970. (Correction, *J. Geophys. Res., 76*, 5002, 1971.)

Bungum, H., S. Vaage, and E. Husebye, The Meløy earthquake sequence, northern Norway; Source parameters and their moment scaling relations, *Bull. Seismol. Soc. Am., 72*, 197–206, 1982.

Campillo, M., J. Plantet, and M. Bouchon, Frequency-dependent attenuation in the crust beneath central France from Lg waves: Data analysis and numerical modeling, *Bull. Seismol. Soc. Am., 75*, 1395–1411, 1985.

Chavez, D., and K. Priestley, Measurement of frequency dependent Lg attenuation in the Great Basin, *Geophys. Res. Lett., 13*, 551–554, 1986.

Chavez, D., and K. Priestley, Apparent Q of Pg and Lg in the Great Basin, paper presented at Seismic Research Symposium, Def. Adv. Res. Proj. Agency/Air Force Geophys. Lab., Nantucket, Ma., June 15-18, 1987.

Chun, K.-Y., G. West, R. Kokoski and C. Samson, A novel technique for measuring Lg attenuation—Results from eastern Canada between 1 to 10 Hz, *Bull. Seismol. Soc. Am., 77*, 398–419, 1987.

Dwyer, J., R. Herrmann, and O. Nuttli, Spatial attenuation of the *Lg* wave in the central United States, *Bull. Seismol. Soc. Am.*, *73*, 781–796, 1983.

Evernden, J., C. Archambeau, and E. Cranswick, An evaluation of seismic decoupling and underground nuclear test monitoring using high-frequency seismic data, *Rev. Geophys.*, *24*, 143–215, 1986.

Fyen, J., NORESS noise spectral studies - beam suppression, *Sci. Rep. 1-86/87*, NTNF/NORSAR, Kjeller, Norway, 1986.

Goncz, J., W. Dean, Z. Der, A. Lees, K. McLaughlin, T. McElfresh, and M. Marshall, Propagation and excitation of *Lg*, *Sn*, and *P–Pn* waves from eastern United States earthquakes by regression analysis of RSTN data, *Final Tech. Rep. TGAL-86-7*, Teledyne Geotech Alexandria Lab., Alexandria, Va., Contract: MDA903-85-C-0086, 1987.

Gupta, I., and K. McLaughlin, Attenuation of ground motion in the eastern United States, *Bull. Seismol. Soc. Am.*, *77*, 366–383, 1987.

Hasegawa, H., *Lg* spectra of local earthquakes recorded by the Eastern Canada Telemetered Network and spectral scaling, *Bull. Seismol. Soc. Am.*, *73*, 1041–1061, 1983.

Hasegawa, H., Attenuation of *Lg* waves in the Canadian Shield, *Bull. Seismol. Soc. Am.*, *75*, 1569–1582, 1985.

Henson, A., and T. Bache, Spectral characteristics of regional phases recorded at NORESS, *Bull. Seismol. Soc. Am.*, *78,*, 708-725, 1988.

Herrmann, R., and A. Kijko, Modeling some empirical vertical component *Lg* relations, *Bull. Seismol. Soc. Am.*, *73*, 157–171, 1983.

Kennett, B., and S. Mykkeltveit, Guided wave propagation in laterally varying media, II, *Lg* waves in northwestern Europe, *Geophys. J. R. Astron. Soc.*, *79*, 257–267, 1984.

Kvaerna, T., and S. Mykkeltveit, Optimum beam deployment for NORESS P-wave detection, *Sci. Rep. 1-86/87*, NTNF/NORSAR, Kjeller, Norway, 1986.

Kvaerna, T., and F. Ringdal, Stability of various f-k estimation methods, *Sci. Rep. 1-86/87*, NTNF/NORSAR, Kjeller, Norway, 1986.

Kvaerna, T., S. Kibsgaard, F. Ringdal, False alarm statistics and threshold determination for regional event detection, *Sci. Rep. 1-87/88*, NTNF/NORSAR, Kjeller, Norway, 1988a.

100

K.aerna, T., S. Kibsgaard, S. Mykkeltveit, F. Ringdal, Towards an optimum beam deployment for NORESS; experiments with a North Sea / western Norway data base, *Sci. Rep. 1-87/88*, NTNF/NORSAR, Kjeller, Norway, 1988b.

Kvamme, L., and J. Havskov, Attenuation of seismic energy from local events in southern Norway, *Sci. Rep. 1-85/86*, NTNF/NORSAR, Kjeller, Norway, 1985.

Langston, C., Aspects of *Pn* and *Pg* propagation at regional distances, *Bull. Seismol. Soc. Am.*, 72, 457–471, 1982.

Mitchell, B., J.-K. Xie, and O. Nuttli, Seismic attenuation and yield estimates: New results using the *Lg* phase, paper presented at Seismic Research Symposium, Def. Adv. Res. Proj. Agency/Air Force Geophys. Lab., Nantucket, Ma., June 15-18, 1987.

Mueller, C., and E. Cranswick, Source parameters from locally recorded aftershocks of the 9 January 1982 Miramichi, New Brunswick, earthquake, *Bull. Seismol. Soc. Am.*, 75, 337–360, 1985.

Mueller, R., and J. Murphy, Seismic characteristics of underground nuclear detonations, *Bull. Seismol. Soc. Am.*, 61, 1675–1692, 1971.

Murphy, J., and T. Bennett, A discrimination analysis of short-period regional seismic data recorded at Tonto Forest observatory, *Bull. Seismol. Soc. Am.*, 72, 1351–1366, 1982.

Mykkeltveit, S., A new regional array in Norway: Design work, *Sci. Rep. 2-82/83*, NTNF/NORSAR, Kjeller, Norway, 1983.

Mykkeltveit, S., and H. Bungum, Processing of regional seismic events using data from small-aperture arrays, *Bull. Seismol. Soc. Am.*, 74, 2313–2333, 1984.

Mykkeltveit, S., K. Astebol, D. Doornbos, and E. Husebye, Seismic array configuration optimization, *Bull. Seismol. Soc. Am.*, 73, 173–186, 1983.

Mykkeltveit, S., D. Harris, and T. Kvaerna, Preliminary evaluation of the event detection and location capability of the small-aperture NORESS array, *Sci. Rep. 2-84/85*, NTNF/NORSAR, Kjeller, Norway, 1985.

Nuttli, O., Seismic wave attenuation and magnitude relations for eastern North America, *J. Geophys. Res.*, 78, 876–885, 1973.

Nuttli, O., On the attenuation of *Lg* waves in western and central Asia and their use as a discriminant between earthquakes and explosions, *Bull. Seismol. Soc. Am., 71*, 249–261, 1981.

Nuttli, O., Yield estimates of Nevada test site explosions obtained from seismic *Lg* waves, *J. Geophys. Res., 91*, 2137–2151, 1986.

Peseckis, L., and P. Pomeroy, Determination of *Q* using *Lg* waves and its implications for nuclear yield estimation, *Eos Trans. AGU, 45*, 995, 1984.

Pomeroy, P., Aspects of seismic wave propagation in eastern North America—A preliminary report, Rondout Associates, Inc., Stone Ridge, N. Y., 1977.

Pomeroy, P., W. Best, and T. McEvilly, Test ban treaty verification with regional data—A review, *Bull. Seismol. Soc. Am., 72*, S89–S129, 1982.

Ringdal, F., Real time event detection using the small-aperture NORESS array, *Sci. Rep. 2-84/85*, NTNF/NORSAR, Kjeller, Norway, 1985a.

Ringdal, F., Initial results from NORESS detection processing, *Sci. Rep. 1-85/86*, NTNF/NORSAR, Kjeller, Norway, 1985b.

Ringdal, F., Regional event detection using the NORESS array, *Sci. Rep. 2-85/86*, NTNF/NORSAR, Kjeller, Norway, 1986.

Ringdal, F., B. Hokland, and T. Kvaerna, Initial results from the NORESS high frequency seismic element (HFSE), *Sci. Rep. 2-85/86*, NTNF/NORSAR, Kjeller, Norway, 1986.

Sereno, T., S. Bratt, and T. Bache, Regional wave attenuation and seismic moment from the inversion of NORESS spectra, *Semi-Annu. Tech. Rep. SAIC 87/1736*, Sci. Appl. Int. Corp., San Diego, Calif., 1987.

Sereno, T., S. Bratt, and T. Bache, Simultaneous inversion of regional wave spectra for attenuation and seismic moment in Scandinavia, *J. Geophys. Res., 93*, 2019-2035, 1988.

Shin, T.-C., and R. Herrmann, *Lg* attenuation and source studies using 1982 Miramichi data, *Bull. Seismol. Soc. Am., 77*, 384–397, 1987.

Singh, S., and R. Herrmann, Regionalization of crustal coda *Q* in the continental United States, *J. Geophys. Res., 88*, 527–538, 1983.

Stevens, J., and S. Day, The physical basis of $m_b:M_s$ and variable frequency magnitude methods for earthquake/explosion discrimination, *J. Geophys. Res., 90,* 3009–3020, 1985.

Street, R., R. Herrmann, and O. Nuttli, Spectral characteristics of the *Lg* wave generated by central United States earthquakes, *Geophys. J. R. Astron. Soc., 41,* 51–63, 1975.

von Seggem, D., and R. Blandford, Source time functions and spectra for underground nuclear explosions, *Geophys. J. R. Astron. Soc., 31,* 83–97, 1972.

Willis, D., Comparison of seismic waves generated by different types of sources, *Bull. Seismol. Soc. Am., 53,* 965–978, 1963.

APPENDIX A. INVERSION RESULTS

Regional Pn and Lg spectra of 186 events (Table 2.1) were inverted for $Q(f)$, seismic moment, and the parameter, c, relating corner frequency to long period source level. The source was parameterized by the Mueller-Murphy explosion model and geometric spreading was modeled by (2.6) with $m = 1/2$ and $r_0 = 100$ km for Lg and $m = 1.3$ with $r_0 = 1$ km for Pn. The Pn spectra were computed for 5-s windows and the Lg spectra were computed for the group velocity range 3.6-3.0 km/s. In terms of a power-law frequency dependence, the path result for Pn is $Q(f) = 325f^{0.48}$ and for Lg is $Q(f) = 560f^{0.26}$. The parameter, c, derived from Pn spectra is 25.8 and from Lg spectra is 19.9.

Table A.1 lists the results of the inversion for source parameters. The event numbers correspond to those of Table 2.1. Corner frequencies were not parameters of the inversion for each event, but were calculated from (2.2) using the inversion results for c and S_0. For the explosions, seismic moment was estimated from $S_0(Pn)$ using (2.3) assuming a surface compressional velocity of 5 km/s and a density of 2.5 gm/cm^3. The earthquake moments were estimated from $S_0(Lg)$ using (2.4) with an average crustal shear wave velocity of 3.5 km/s and a crustal density of 2.7 gm/cm^3. Because the radiation patterns are unknown, moments were not estimated for earthquakes for which only Pn spectra were included in the inversion or for events of unknown source type. Similarly, moments were not estimated for explosions without Pn spectra because of the uncertainty in the relative Lg to Pn source excitation (2.5).

Figure A.1 displays theoretical and data spectra for all of the events used in the inversion. The theoretical spectra were computed using (2.1) with the results of the inversion for $Q(f)$ and $S(f)$. Each spectrum is identified by the event number in Table 2.1. The spectra have been vertically offset for display purposes.

Table A.1. Inverted source parameters

Event	Magnitude		Type	$S_0(Pn)$	$f_c(Pn)$	$S_0(Lg)$	$f_c(Lg)$	M_o (10^{18} dyne-cm)
1	3.0		EX-E7	21.42	9.3	11.18	8.9	841.0
2	2.8	(B)	EQ	2.86	18.2	4.36	12.2	63.4
3	2.3		EQ	1.45	22.8	2.93	13.9	42.6
4	2.2		EQ	0.79	27.9	1.98	15.8	28.7
5	1.9	(R)	EX-BLA	1.53	22.4	0.85	20.9	60.1
6	2.8		EQ	1.06	25.3	3.77	12.8	54.9
7	2.8		EX-V5	20.73	9.4	13.71	8.3	814.0
8	2.4		EX-BLA	1.84	21.0	1.26	18.4	72.2
9	2.1		EX-TTT	0.60	30.6	1.36	18.0	23.5
10	2.0	(R)	--	1.13	24.8	0.65	22.9	---
11	2.6		EX-E3	----	---	3.39	13.2	---
12	2.7		EX-E7	12.73	11.0	9.98	9.2	499.9
13	1.9		EX-TTT	0.86	27.1	0.87	20.8	33.9
14	2.9		EX-V12	27.71	8.5	8.36	9.8	1088.0
15	2.9		EX-V8	25.96	8.7	----	---	1019.5
16	2.4	(H)	EX-E4	----	---	9.55	9.4	---
17	1.9		--	1.03	25.6	0.52	24.7	---
18	2.5		EX-E3	----	---	3.22	13.5	---
19	3.0		EX-E8	----	---	7.18	10.3	---
20	3.0		EQ	0.76	28.3	7.10	10.3	103.3
21	2.8		EX-V4	34.50	7.9	----	---	1354.7
22	2.1	(R)	EQ	0.55	31.5	0.53	24.6	7.6
23	3.0		EQ	2.06	20.3	10.38	9.1	150.9
24	2.8		EX-K1	----	---	21.72	7.1	---
25	<2.0	(H)	EX-V2	13.70	10.8	----	---	537.9
26	3.1		EX-E4	----	---	8.15	9.9	---
27	2.2		--	0.40	34.9	1.53	17.3	---
28	1.9		EQ	0.38	35.4	0.68	22.6	9.9
29	3.2		EX-E8	----	---	7.52	10.1	---
30	2.0	(R)	EX-V11	12.61	11.1	7.56	10.1	495.1
31	2.0		EQ	2.40	19.2	----	---	---
32	3.3		EX-E8	32.10	8.1	16.86	7.8	1260.7
33	2.8		EX-E6	----	---	4.56	12.0	---
34	2.8		EX-E8	24.40	8.9	12.96	8.5	958.3
35	2.4	(H)	EX-V2	28.25	8.5	----	---	1109.5
36	2.5	(H)	EX-V2	35.04	7.9	----	---	1375.9
37	3.2	(R)	EQ	13.88	10.7	----	---	---

Event	Magnitude		Type	$S_0(Pn)$	$f_c(Pn)$	$S_0(Lg)$	$f_c(Lg)$	M_o (10^{18} dyne-cm)
38	2.6	(R)	EQ	15.27	10.4	----	---	---
39	2.6		EX-E3	----	---	2.46	14.7	---
40	2.9		EX-V1C	15.09	10.4	9.24	9.5	592.5
41	2.6		EX-E6	----	---	3.63	12.9	---
42	2.7		EQ	7.37	13.2	5.46	11.3	79.4
43	2.2	(H)	EX-V4	16.01	10.2	----	---	628.6
44	3.3		EX-E8	27.54	8.5	14.52	8.1	1081.5
45	2.4	(H)	EX-V2	33.78	8.0	----	---	1326.6
46	2.8		EQ	4.74	15.4	3.75	12.8	54.5
47	4.7	(P)	EQ	99.09	5.6	----	---	---
48	2.7		EX-E9	----	---	2.71	14.3	---
49	2.7		--	----	---	3.31	13.3	---
50	4.8	(P)	EQ	184.16	4.5	----	---	---
51	4.6	(P)	EQ	91.32	5.7	----	---	---
52	2.3	(H)	EX-M7	3.05	17.8	----	---	119.8
53	2.1		EX-TTT	1.47	22.7	0.96	20.1	57.9
54	2.9		EX-V7	13.45	10.8	14.97	8.1	528.2
55	2.8		--	13.91	10.7	16.70	7.8	---
56	1.8		EX-TTT	0.82	27.5	0.52	24.7	32.3
57	2.6		EQ	----	---	1.80	16.3	26.2
58	2.5		EX-E7	17.01	10.0	10.68	9.0	667.9
59	2.7		--	1.87	20.9	4.96	11.7	---
60	3.4		EX-E8	25.73	8.7	17.15	7.7	1010.4
61	2.7		EX-E8	15.02	10.5	7.64	10.1	589.9
62	3.3		EX-E7	30.88	8.2	15.12	8.0	1212.8
63	2.3		EX-TTT	2.59	18.8	2.33	15.0	101.8
64	3.3		EQ	24.52	8.9	71.28	4.8	1036.9
65	2.5		EQ	2.60	18.8	3.75	12.8	54.6
66	1.7		EQ	0.56	31.2	0.35	28.1	5.1
67	2.9		EQ	1.94	20.7	6.48	10.7	94.2
68	2.5		EQ	1.25	23.9	5.31	11.4	77.2
69	3.3		EX-V8	32.06	8.1	12.22	8.6	1259.1
70	3.3		EX-E7	20.06	9.5	----	---	787.9
71	1.9		EX-TTT	0.84	27.3	0.67	22.7	33.0
72	2.9		EX-K2	----	---	24.06	6.9	---
73	1.9		EQ	----	---	0.72	22.1	10.5
74	1.6		EQ	----	---	0.32	29.0	4.7
75	2.3		EQ	1.21	24.2	2.53	14.6	36.8
76	1.9		EQ	0.69	29.2	1.32	18.1	19.2
77	2.6		EX-E7	21.58	9.3	11.85	8.7	847.4

Event	Magnitude		Type	$S_0(Pn)$	$f_c(Pn)$	$S_0(Lg)$	$f_c(Lg)$	M_o (10^{18} dyne-cm)
78	2.6		EX-R1	----	---	3.47	13.1	---
79	3.1		EX-V10	104.89	5.5	33.38	6.2	4118.9
80	2.5		EX-E12	----	---	7.73	10.1	---
81	1.9	(R)	EQ	----	---	20.52	7.3	298.5
82	2.8	(H)	EX-K5	58.58	6.6	----	---	2300.5
83	2.2	(H)	EQ	3.76	16.6	6.01	10.9	87.5
84	2.7		EX-E8	13.93	10.7	10.24	9.2	546.9
85	2.4		EX-TIT	2.17	19.9	3.21	13.5	85.4
86	2.3	(B)	EX-TIT	0.58	30.9	----	---	22.9
87	1.7		EQ	0.33	37.2	----	---	---
88	2.5	(H)	EX-E4	----	---	8.86	9.6	---
89	3.1		EX-E4	----	---	15.94	7.9	---
90	2.6		EX-V10	19.70	9.5	20.01	7.3	773.5
91	3.1		EX-K2	42.77	7.4	48.36	5.5	1679.7
92	1.9		EQ	0.53	31.9	1.06	19.5	15.4
93	3.2		EX-E9	----	---	10.38	9.1	---
94	1.8		EQ	1.11	24.9	0.72	22.2	10.5
95	3.3		EX-E7	19.59	9.6	13.10	8.4	769.4
96	1.9		EQ	0.51	32.3	0.94	20.3	13.7
97	2.1		EQ	0.63	30.0	1.17	18.8	17.1
98	3.2		EX-E7	26.65	8.6	14.07	8.2	1046.6
99	3.2		EX-E7	13.49	10.8	12.46	8.6	529.9
100	2.8		EX-V8	11.44	11.4	----	---	449.3
101	2.9		EX-V5	14.54	10.6	19.27	7.4	570.9
102	2.6		EX-E3	----	---	3.62	12.9	---
103	2.5		EX-E4	4.93	15.2	7.05	10.4	193.6
104	2.0		EQ	0.72	28.8	1.18	18.8	17.1
105	3.5		EX-E8	24.26	8.9	23.36	7.0	952.7
106	1.6		EQ	0.18	45.9	0.37	27.6	5.4
107	1.9		EX-TIT	0.88	26.9	0.56	24.1	34.5
108	4.4	(H)	EQ	1321.80	2.3	----	---	---
109	2.0		EQ	0.64	30.0	0.85	21.0	12.3
110	2.8		--	10.86	11.6	10.99	8.9	---
111	3.0		EX-V1C	16.64	10.1	----	---	653.5
112	1.8	(B)	EX-NYG	----	---	0.26	31.1	---
113	2.1		--	1.41	23.0	1.14	19.0	---
114	2.7		EX-K2	----	---	65.35	4.9	---
115	2.5		EX-V2	27.76	8.5	17.31	7.7	1090.3
116	2.4		--	0.74	28.5	0.90	20.6	---
117	2.6		EQ	----	---	2.54	14.6	37.0

Event	Magnitude	Type	$S_0(Pn)$	$f_c(Pn)$	$S_0(Lg)$	$f_c(Lg)$	M_o (10^{18} dyne-cm)
118	2.2	EX-BLA	1.35	23.3	1.18	18.8	53.1
119	2.3	EQ	----	---	1.05	19.6	15.2
120	3.1	EX-V7	----	---	20.22	7.3	---
121	2.4	EQ	0.67	29.5	3.32	13.3	48.3
122	2.6	--	----	---	17.93	7.6	---
123	2.3	EX-BLA	1.30	23.6	0.65	23.0	51.0
124	2.4	EX-BLA	2.84	18.2	2.01	15.8	111.4
125	2.0	EQ	1.05	25.3	1.12	19.1	16.3
126	2.7	EQ	1.28	23.7	4.37	12.2	63.6
127	3.9	EX-V3	121.90	5.2	102.18	4.3	4786.9
128	1.7	EX-TIT	1.05	25.3	0.80	21.5	41.3
129	3.0	EX-E5	----	---	5.29	11.4	---
130	3.7	EX-V3	50.95	7.0	----	---	2000.7
131	2.6	EX-V1C	25.44	8.8	24.84	6.8	999.0
132	3.1	--	5.46	14.6	10.44	9.1	---
133	3.2	EQ	3.46	17.1	18.10	7.6	263.3
134	1.1	EQ	----	---	0.12	40.6	1.7
135	2.5	EX-BLA	3.19	17.5	1.78	16.4	125.1
136	1.6	EQ	0.74	28.5	0.31	29.3	4.5
137	1.8	EX-TIT	0.99	25.9	0.66	22.9	38.7
138	2.9	EX-V4	18.78	9.7	26.10	6.7	737.6
139	2.1	EQ	0.49	32.6	1.80	16.4	26.1
140	2.4	--	3.15	17.6	2.05	15.6	---
141	2.6	EX-V10	----	---	10.89	9.0	---
142	2.8	EQ	8.63	12.6	7.03	10.4	102.3
143	2.7	EX-V12	20.34	9.4	16.21	7.9	798.8
144	3.2	--	31.01	8.2	19.34	7.4	---
145	2.7	EX-E4	7.97	12.9	9.46	9.4	313.1
146	2.3	EX-BLA	1.85	21.0	1.40	17.8	72.6
147	2.0	EQ	1.45	22.8	1.00	19.9	14.6
148	4.3	EQ	67.41	6.3	----	---	---
149	3.2	EX-V8	29.09	8.4	21.99	7.1	1142.5
150	3.4	EQ	5.63	14.5	13.67	8.3	198.9
151	3.1	EX-K9	76.54	6.1	58.44	5.1	3005.8
152	3.5	EQ	6.27	14.0	----	---	---
153	3.0	EX-E4	9.87	12.0	10.24	9.2	387.6
154	2.3	EX-BLA	2.49	19.0	1.49	17.4	97.6
155	3.1	EX-E8	9.80	12.0	11.91	8.7	384.9
156	3.0	EX-E6	6.29	14.0	6.87	10.5	247.1
157	2.8	EX-V1B	12.67	11.1	7.07	10.4	497.6

Event	Magnitude		Type	$S_0(Pn)$	$f_c(Pn)$	$S_0(Lg)$	$f_c(Lg)$	M_o (10^{18} dyne-cm)
158	2.2		EX-BLA	2.16	20.0	1.17	18.9	84.8
159	2.6	(H)	EX-K4	64.95	6.4	----	---	2550.8
160	2.3		EX-BLA	1.75	21.4	1.04	19.6	68.8
161	3.2		EX-E7	21.46	9.3	9.93	9.2	842.6
162	2.6		EX-E4	----	---	6.07	10.9	---
163	2.8		--	7.06	13.4	8.68	9.7	---
164	2.4		EX-BLA	2.20	19.8	1.39	17.8	86.5
165	3.1		--	5.16	14.9	----	---	---
166	3.0		EX-E2	2.96	18.0	7.53	10.1	116.4
167	2.6		EX-R1	8.64	12.6	4.26	12.3	339.2
168	1.9		EX-TIT	0.67	29.5	0.87	20.8	26.2
169	2.4		EX-BLA	2.13	20.1	1.61	17.0	83.5
170	2.3		EQ	1.04	25.4	1.01	19.8	14.7
171	3.9		EQ	61.10	6.5	171.43	3.6	2493.9
172	2.1		EX-BLA	2.01	20.4	0.77	21.7	78.7
173	3.0		--	----	---	10.73	9.0	---
174	2.4		EX-BLA	2.19	19.9	1.27	18.3	85.9
175	2.5		EQ	1.16	24.5	2.23	15.2	32.5
176	3.3		EQ	2.82	18.2	17.03	7.7	247.8
177	1.9		EQ	0.91	26.6	0.80	21.4	11.7
178	1.9		EX-TIT	0.83	27.4	0.65	22.9	32.7
179	2.0		EX-TIT	1.19	24.4	0.95	20.3	46.6
180	2.1		EQ	1.59	22.1	1.43	17.6	20.8
181	2.4		EQ	2.02	20.4	4.30	12.2	62.6
182	2.6	(B)	EQ	3.92	16.4	7.63	10.1	111.0
183	2.3		EQ	3.57	16.9	3.65	12.9	53.1
184	2.4		EQ	0.95	26.2	1.52	17.3	22.1
185	3.4	(B)	EQ	11.23	11.5	31.07	6.3	452.0
186	1.8		EQ	0.85	27.3	0.49	25.3	7.1

(B) Bergen network magnitude

(H) Helsinki network magnitude

(P) PDE magnitude (M_b)

(R) *RONAPP* uncorrected magnitude
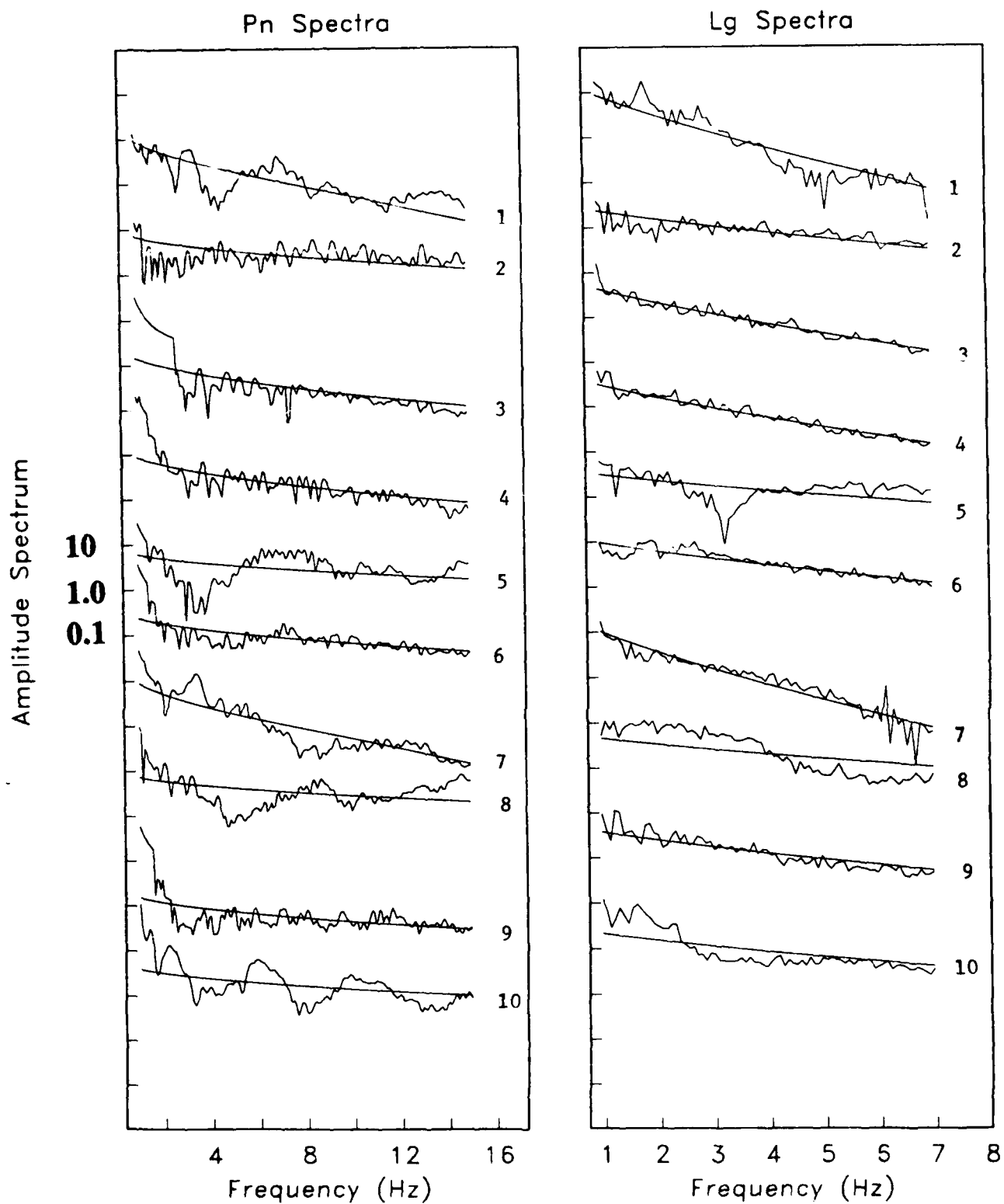
Figure A.1. Theoretical *Pn* and *Lg* spectra compared to observed spectra for the 186 regional events used in the inversion. The theoretical spectra were computed using the inversion parameters described in this appendix and in Table A.1.
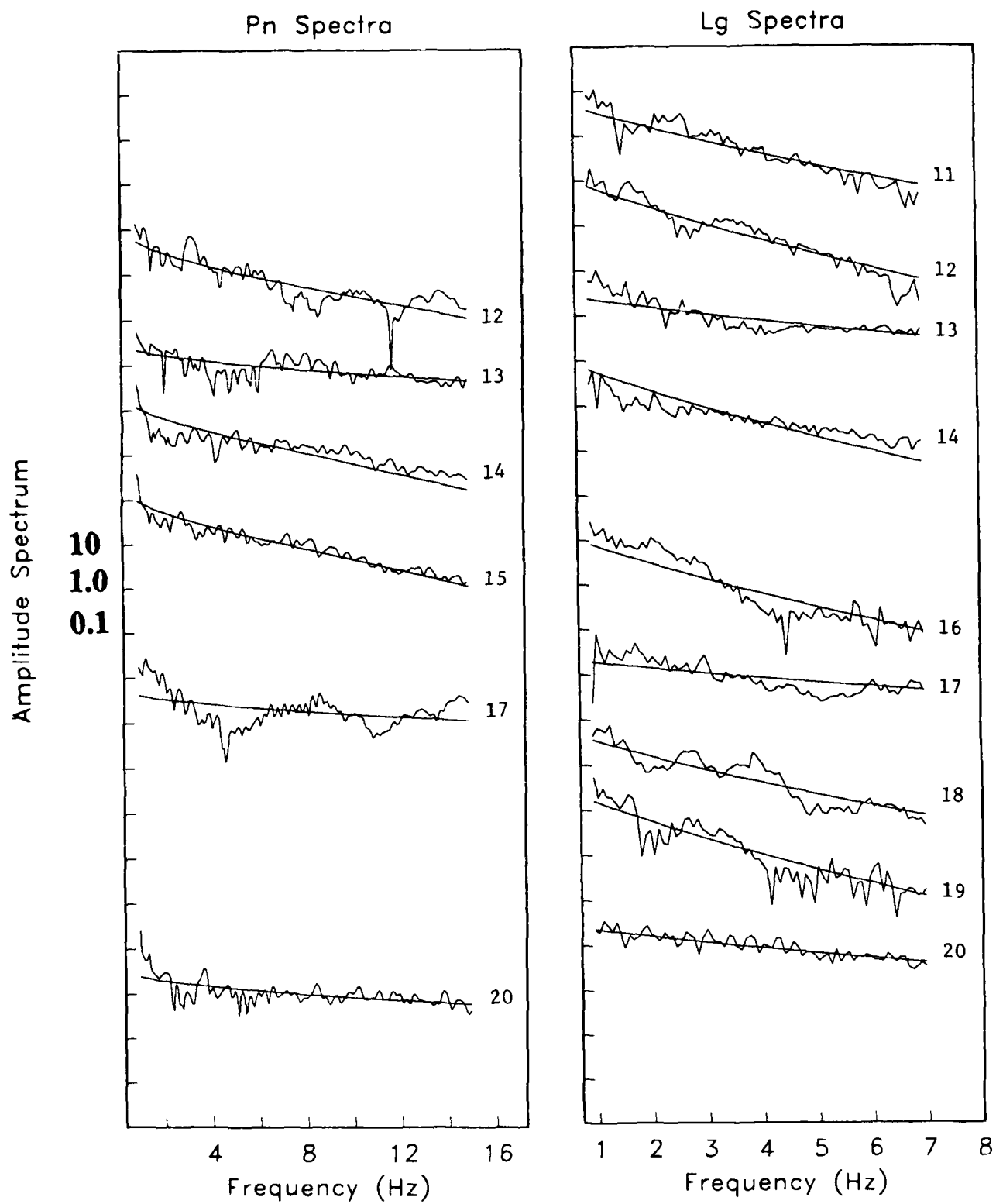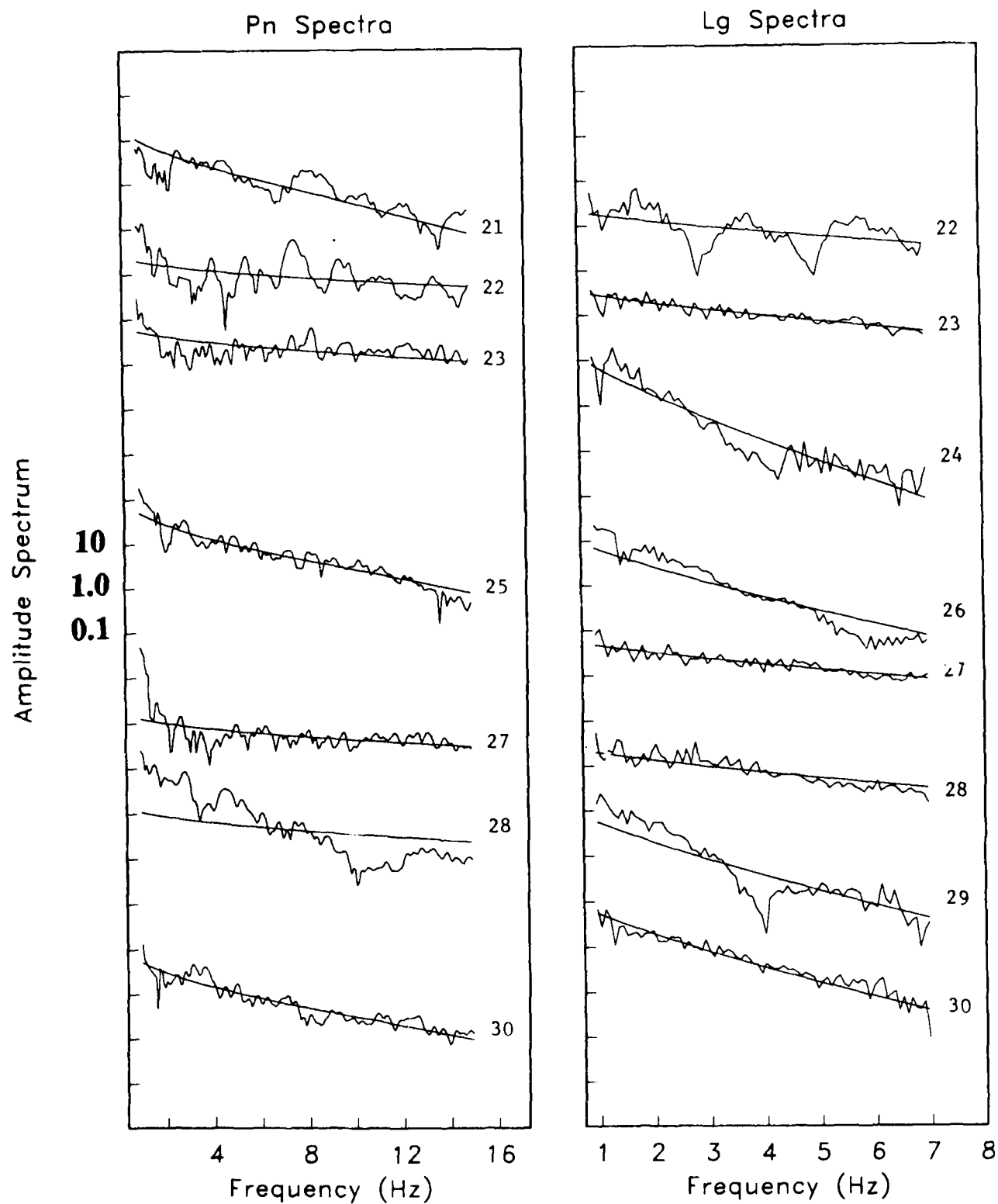
110

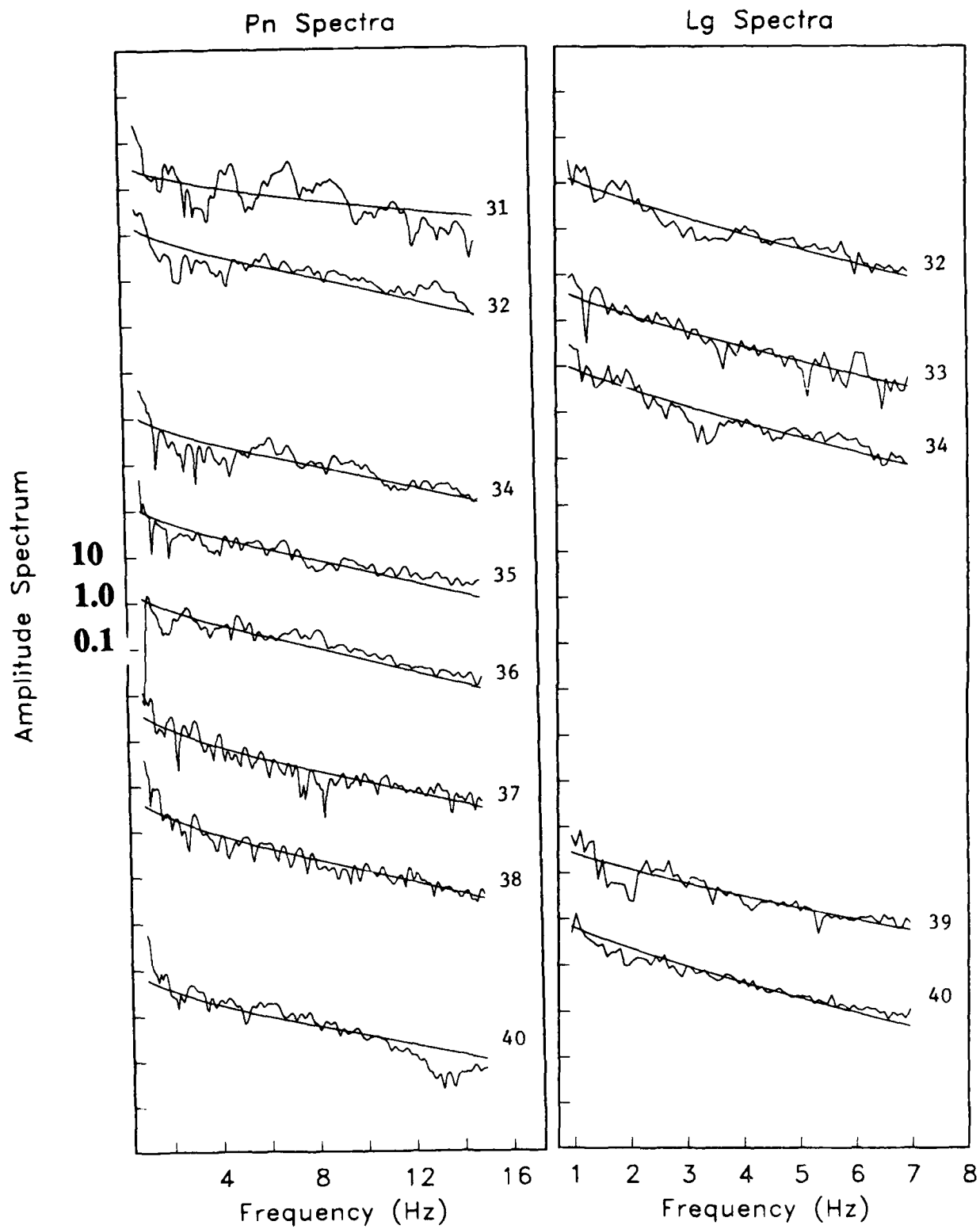Figure A.1. (Continued).

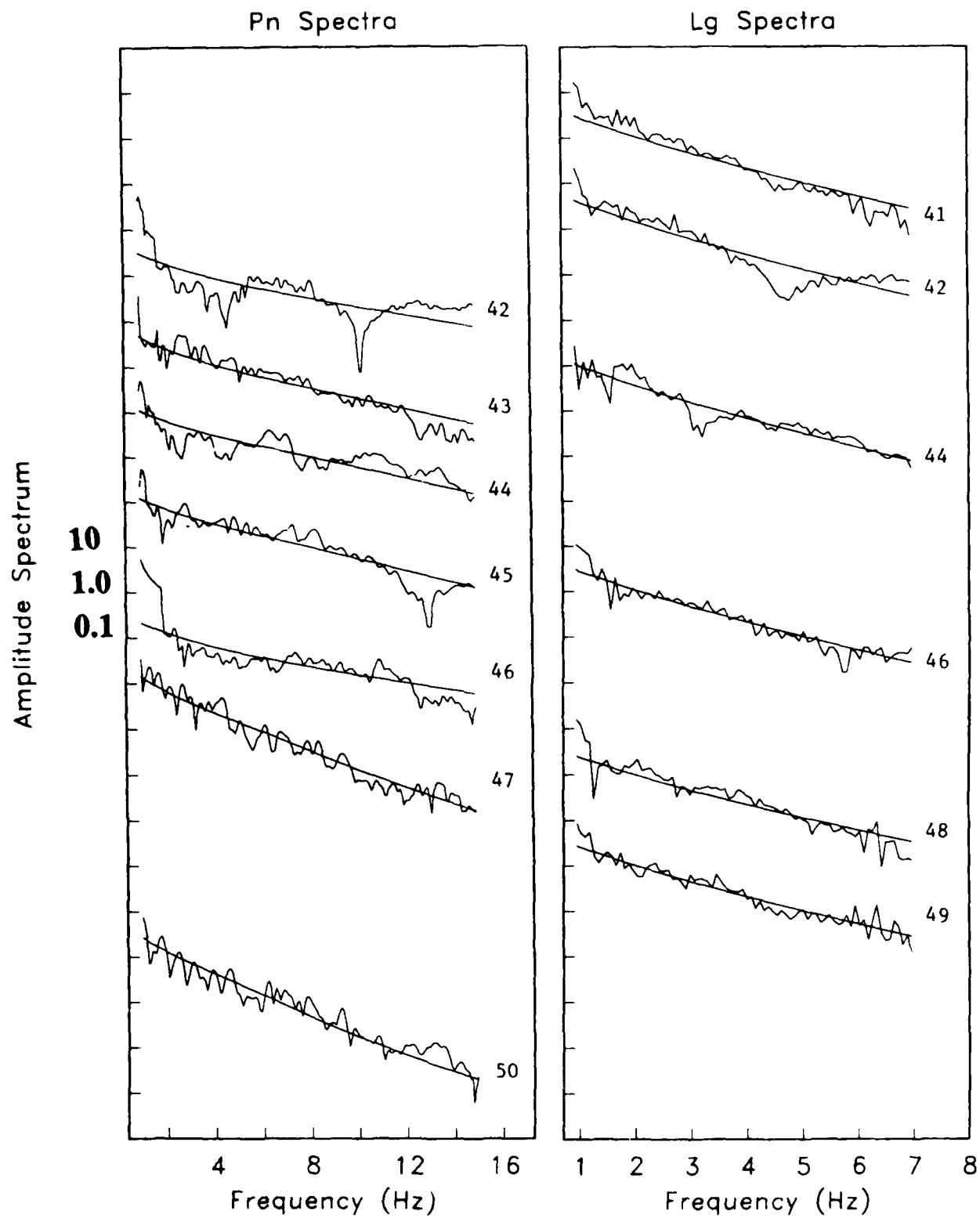Figure A.1. (Continued).

Figure A.1. (Continued).
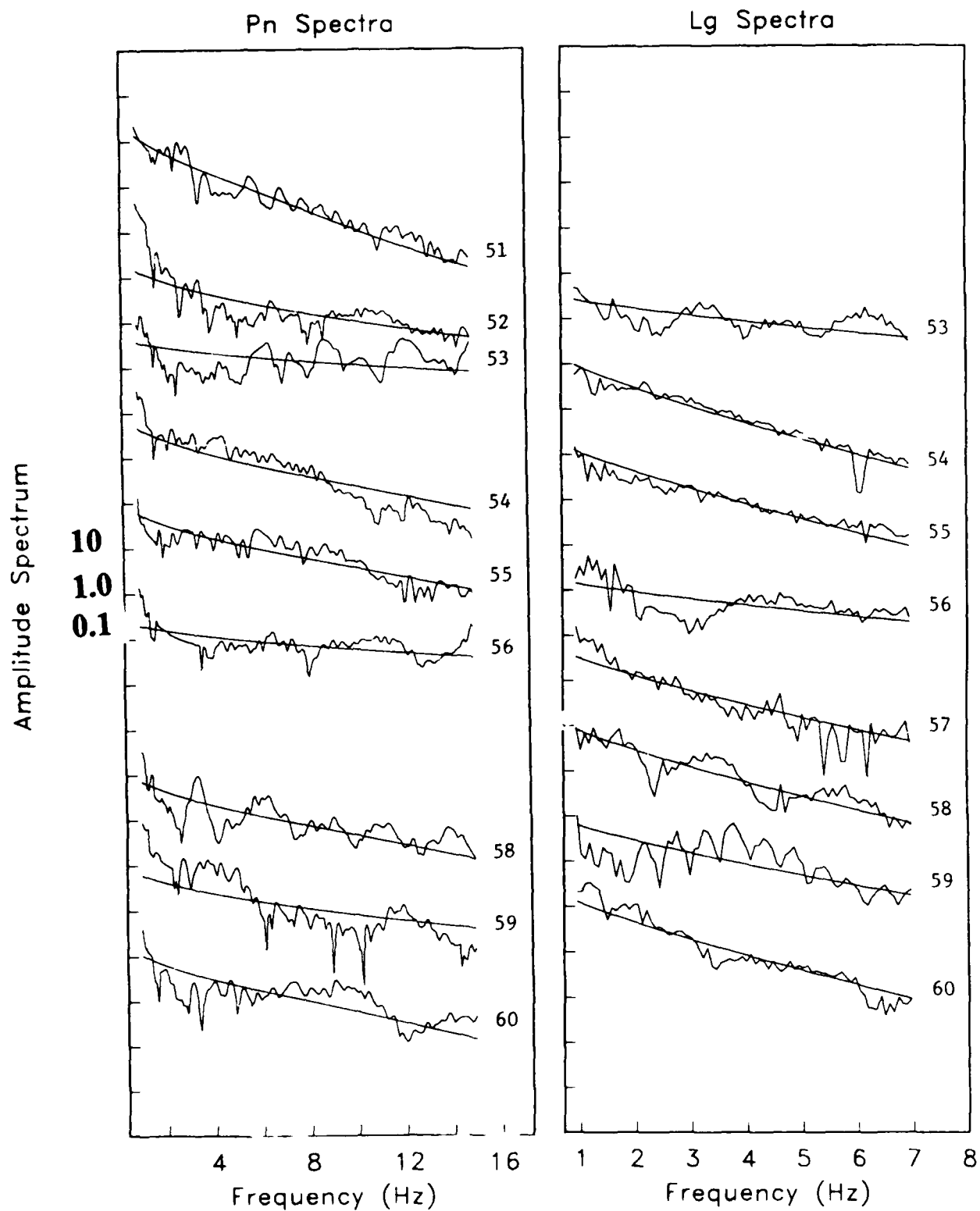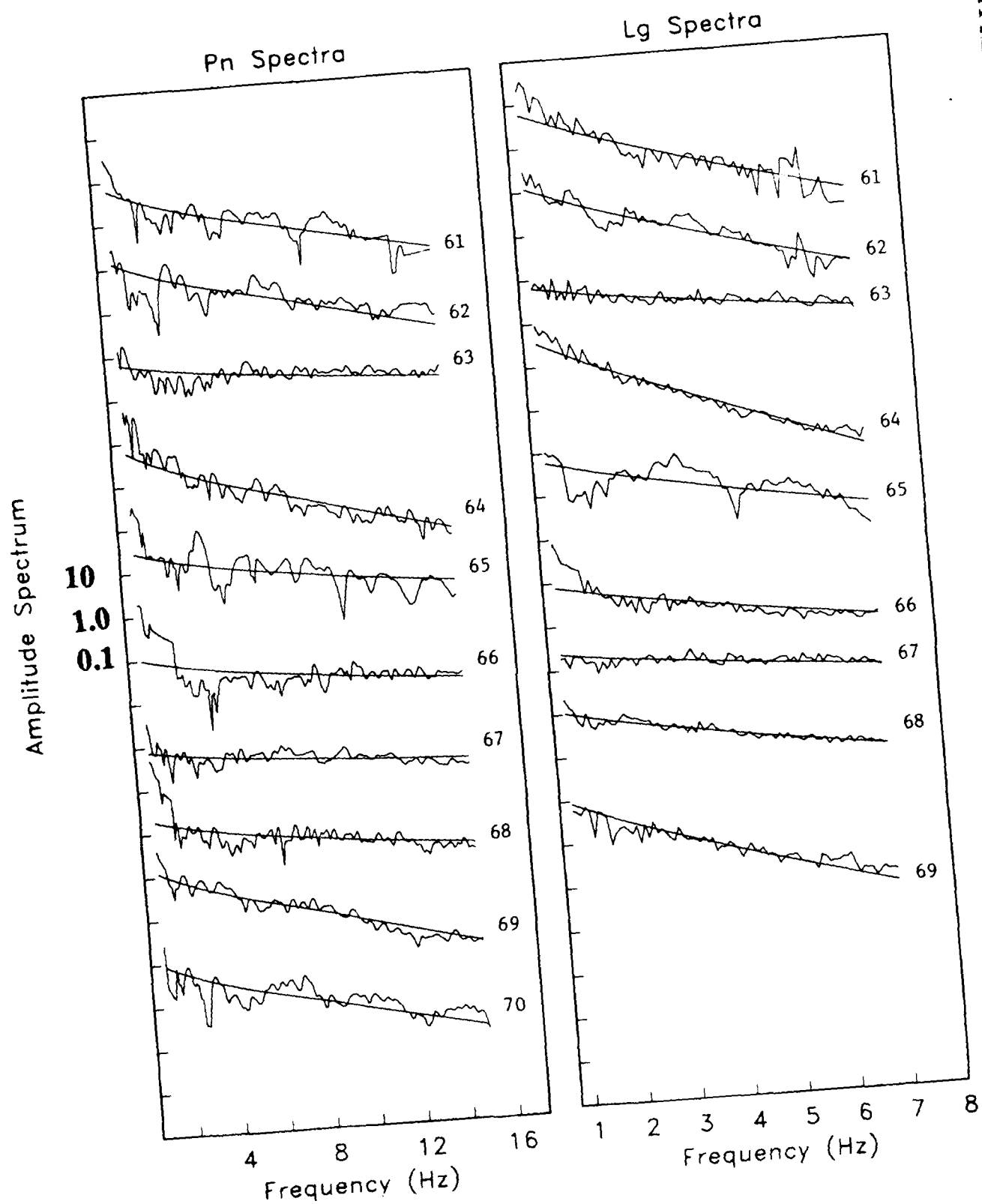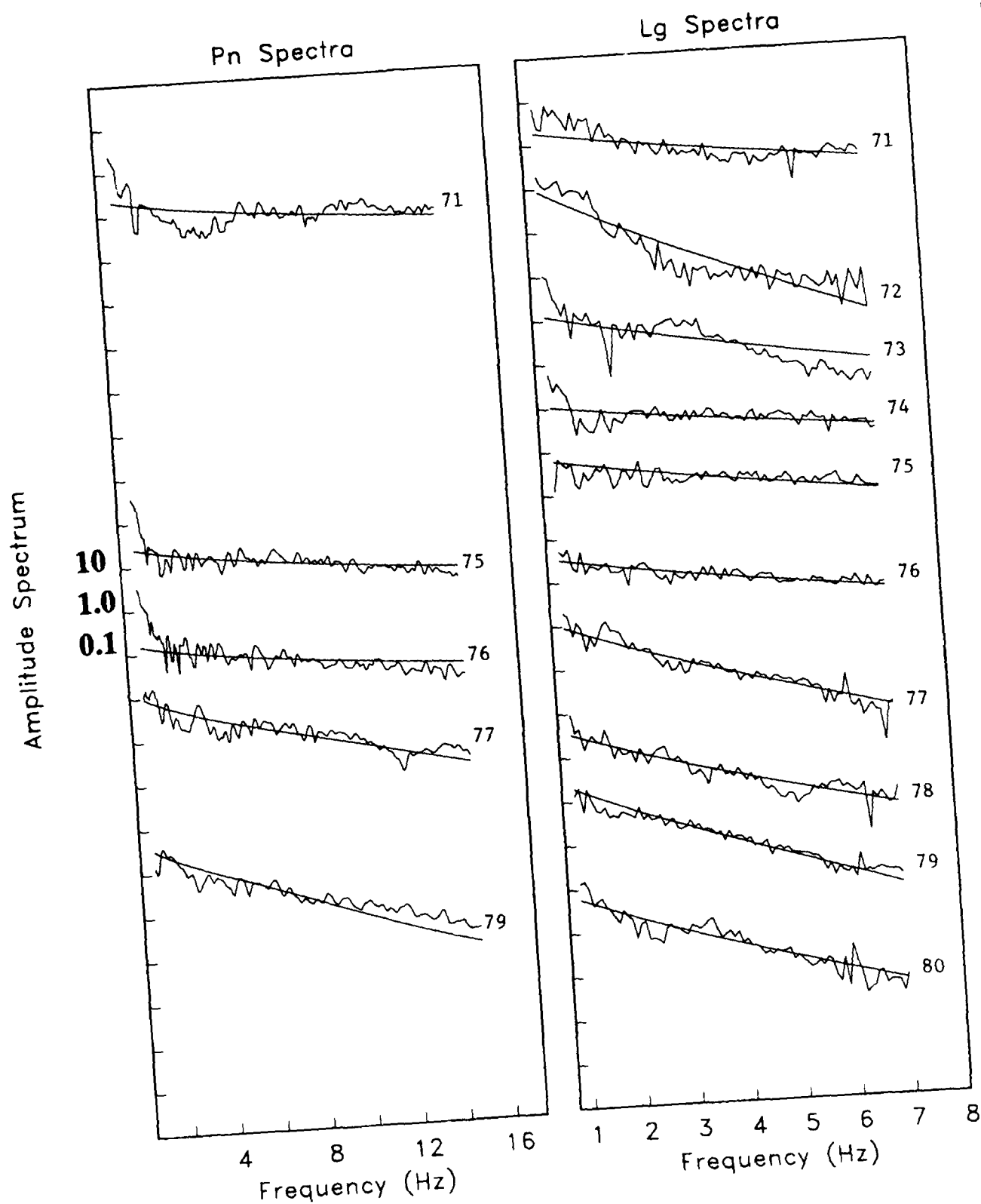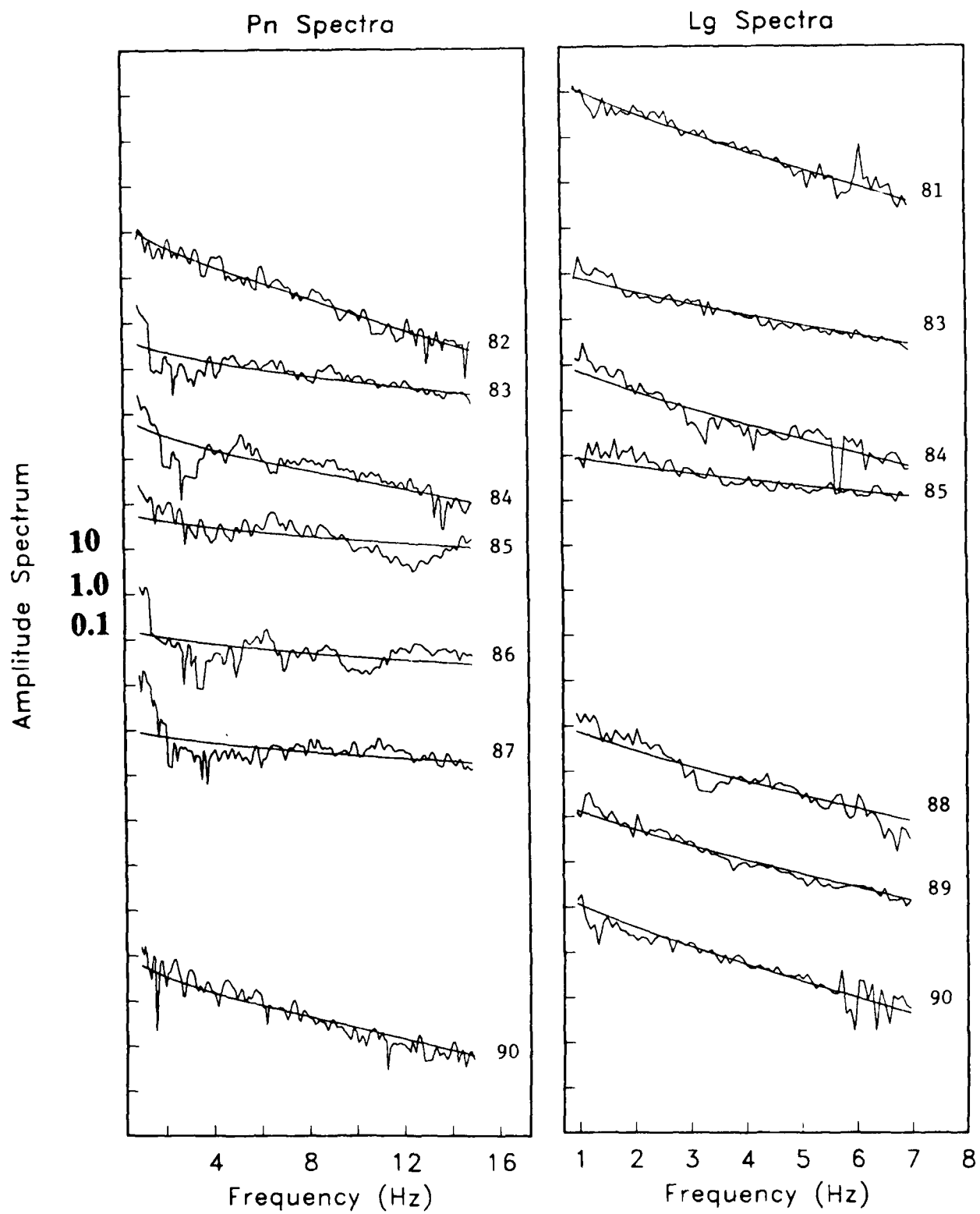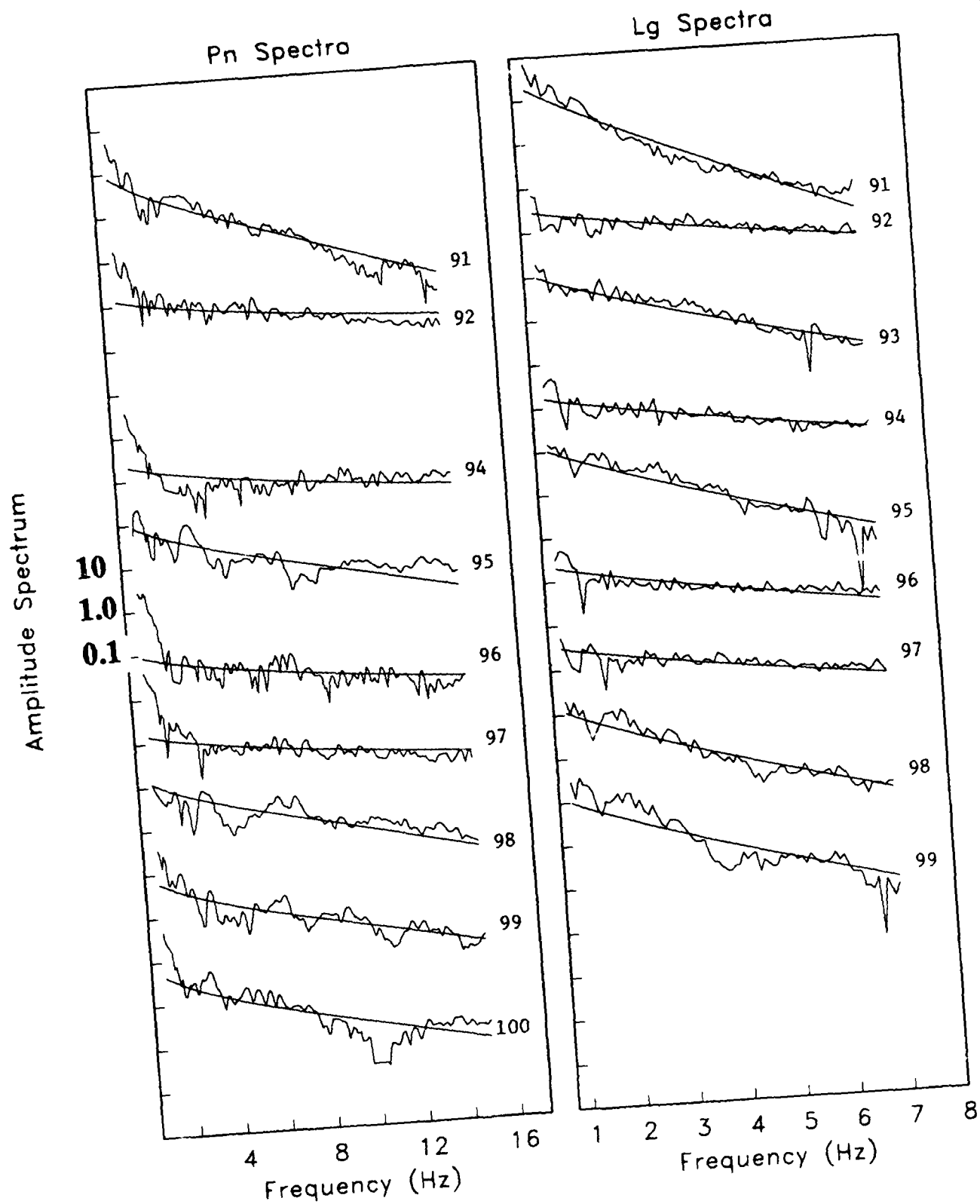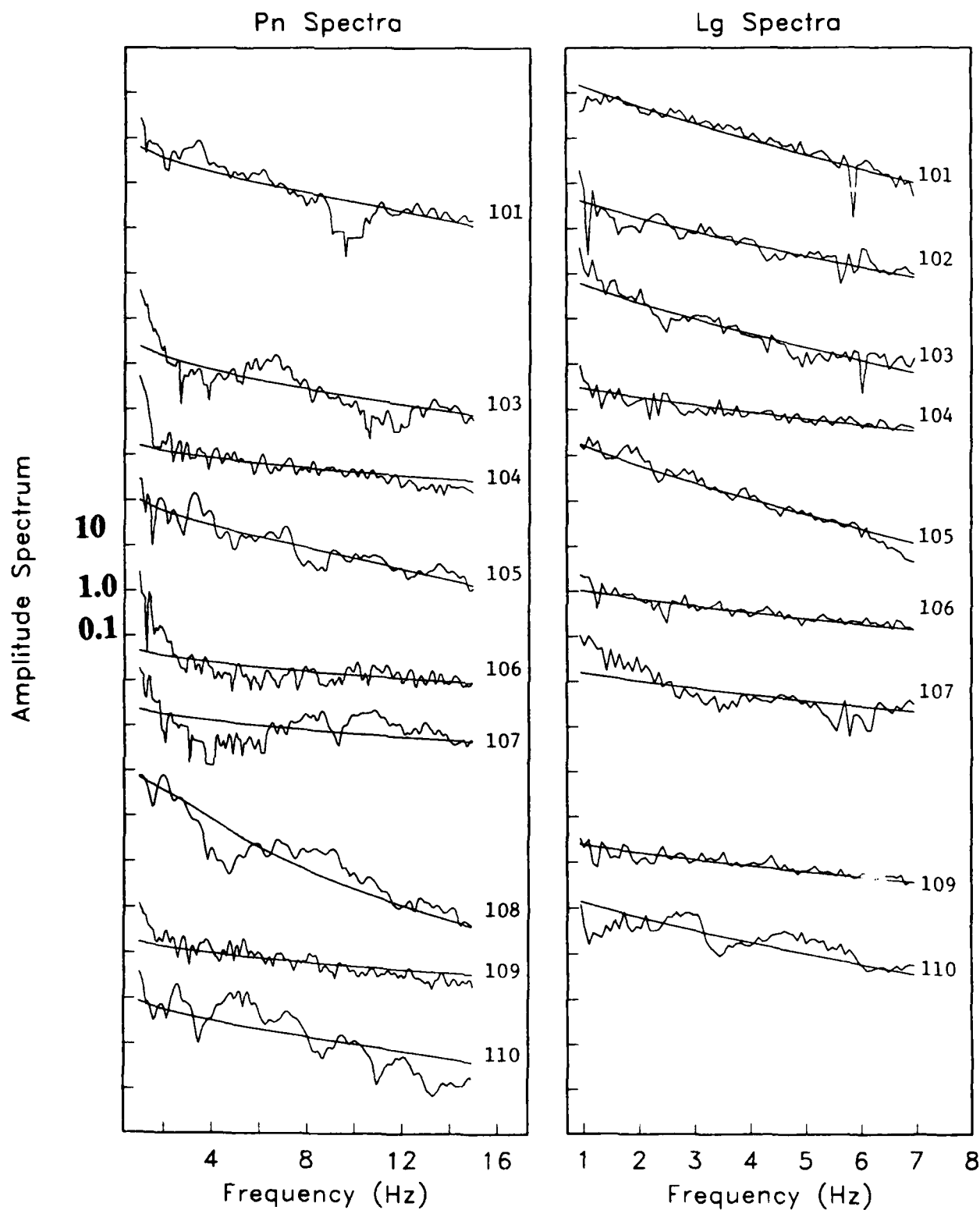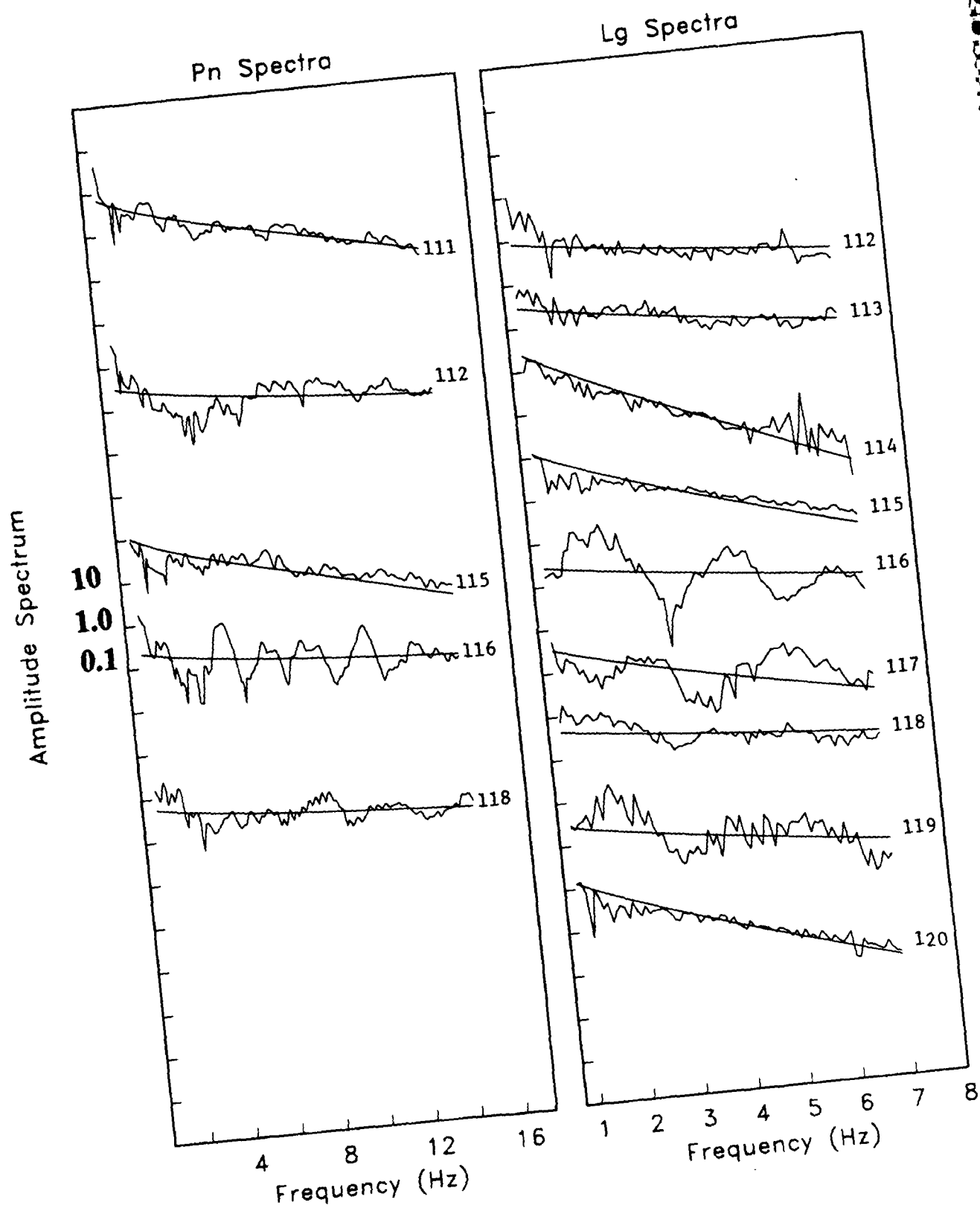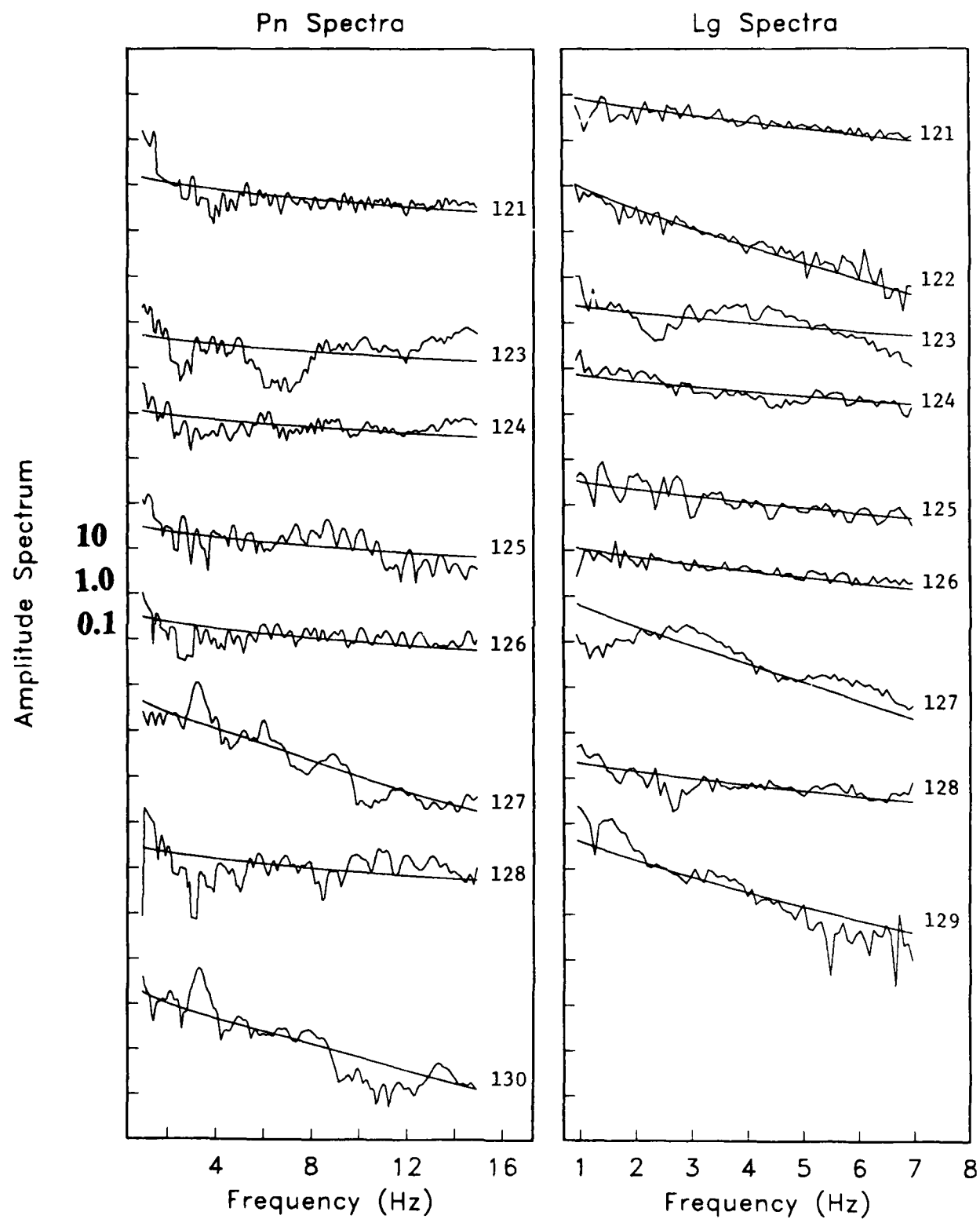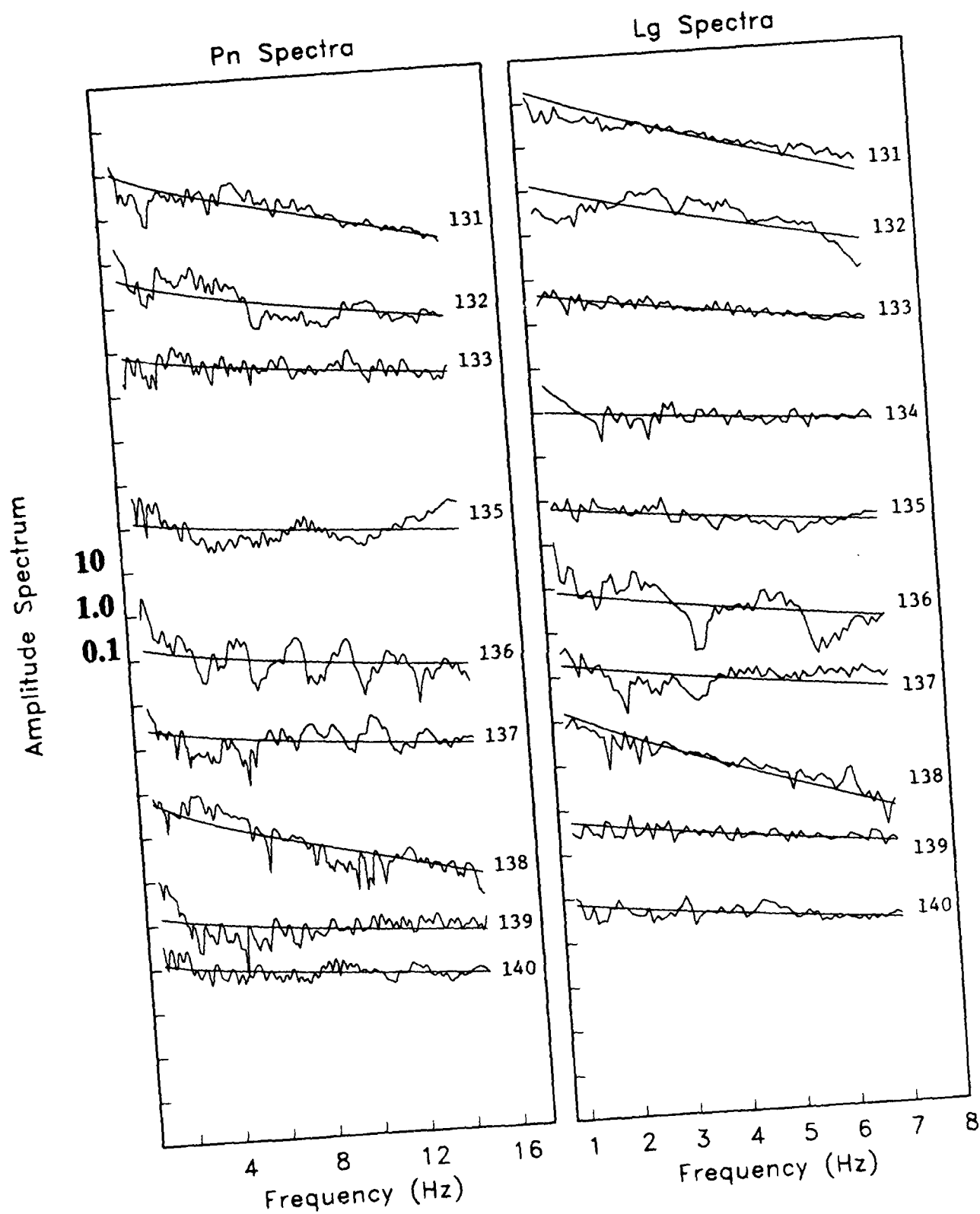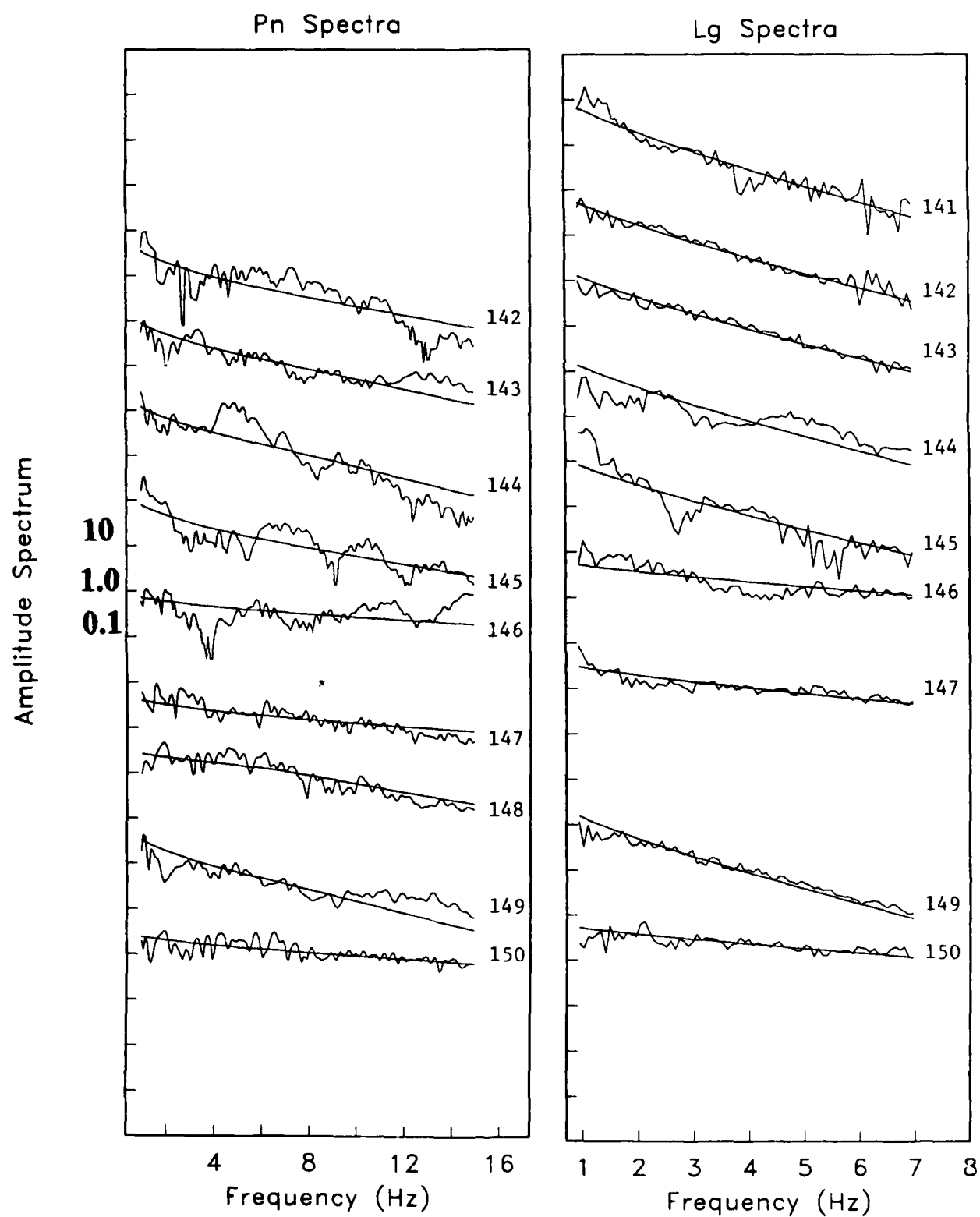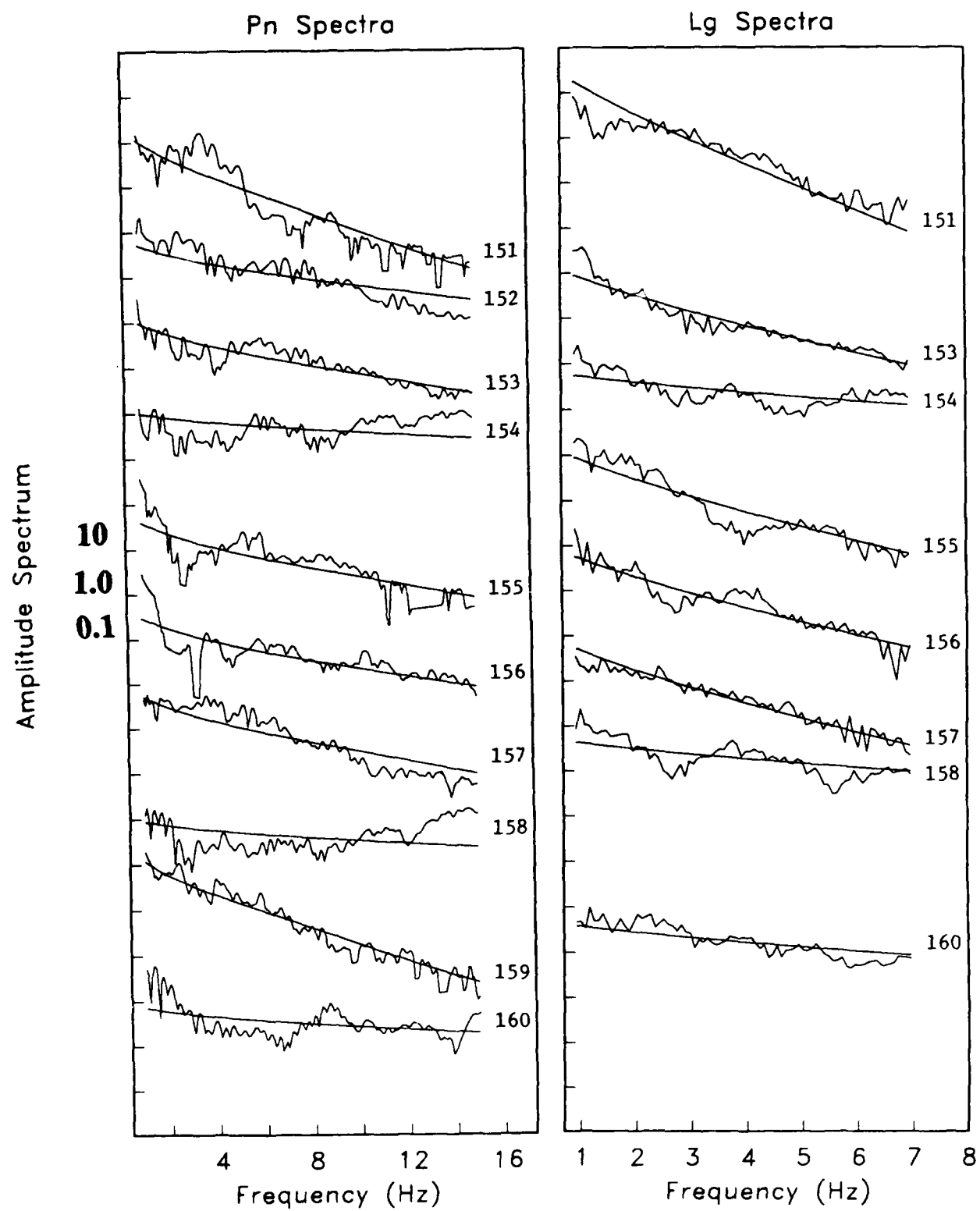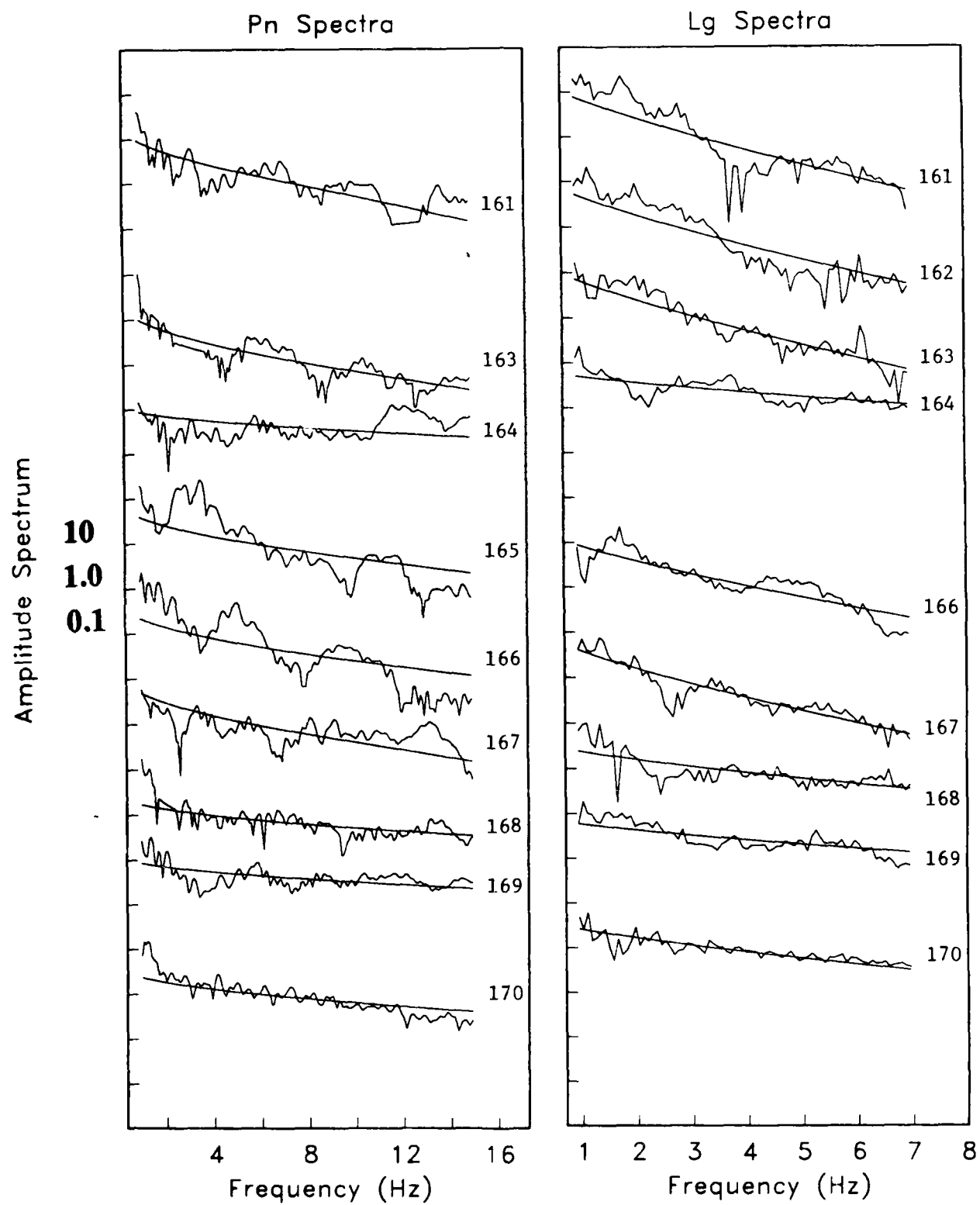
113

Figure A.1. (Continued).

Figure A.1. (Continued).

Figure A.1. (Continued).

116

Figure A.1. (Continued).

117

Figure A.1. (Continued).

118

Figure A.1. (Continued).

119

Figure A.1. (Continued).

120

Figure A.1. (Continued).

121

Figure A.1. (Continued).

Figure A.1. (Continued).

123

Pn Spectra

Lg Spectra

Amplitude Spectrum

10

1.0

0.1

142

143

144

145

146

147

148

149

150

141

142

143

144

145

146

147

149

150

Frequency (Hz)

Frequency (Hz)

4   8   12   16

1 2 3 4 5 6 7 8

Figure A.1. (Continued).

124

Figure A.1. (Continued).
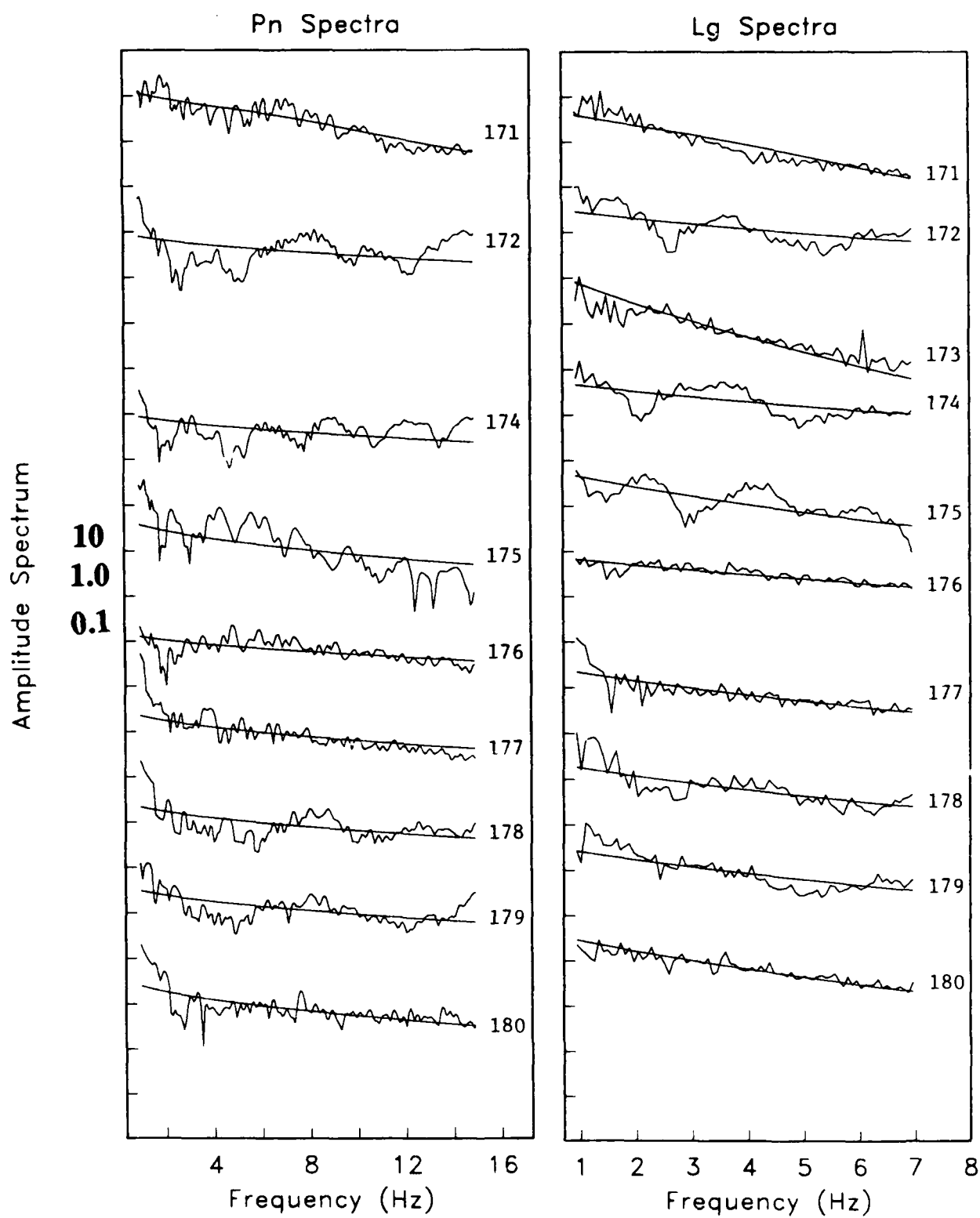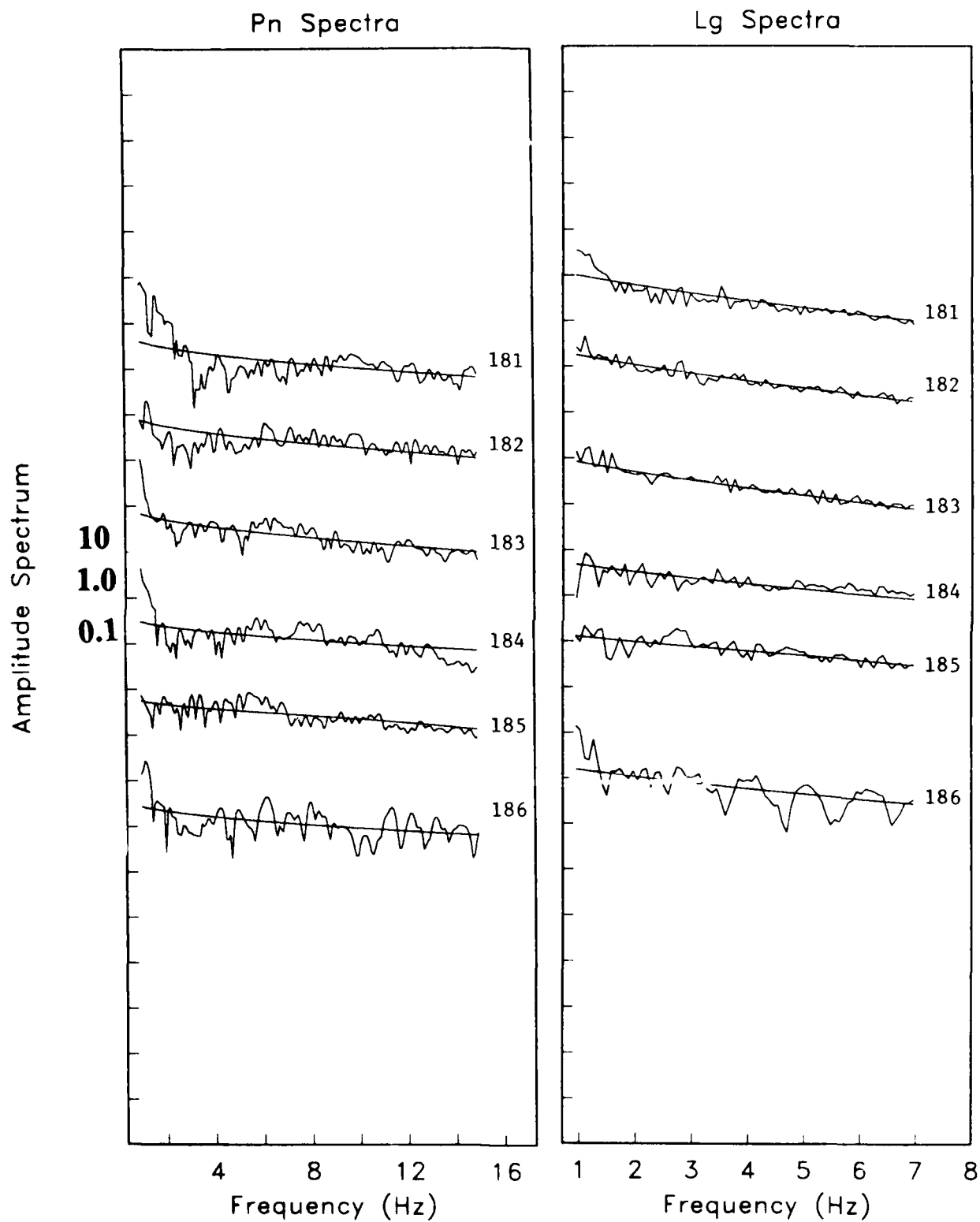
Figure A.1. (Continued).

126

Figure A.1. (Continued).

127

Figure A.1. (Continued).

128

Professor Keiiti Aki
Center for Earth Sciences
University of Southern California
University Park
Los Angeles, CA 90089-0741

Professor Charles B. Archambeau
Cooperative Institute for Resch
  in Environmental Sciences
University of Colorado
Boulder, CO   80309

Dr. Thomas C. Bache Jr.
Science Applications Int'l Corp.
10210 Campus Point Drive
San Diego, CA 92121   (2 copies)

Dr. Douglas R. Baumgardt
Signal Analysis & Systems Div.
ENSCO, Inc.
5400 Port Royal Road
Springfield, VA 22151-2388

Dr. S. Bratt
Science Applications Int'l Corp.
10210 Campus Point Drive
San Diego, CA 92121

Dr. Lawrence J. Burdick
Woodward-Clyde Consultants
P.O. Box 93245
Pasadena, CA 91109-3245 (2 copies)

Professor Robert W. Clayton
Seismological Laboratory/Div. of
  Geological & Planetary Sciences
California Institute of Technology
Pasadena, CA 91125

Dr. Vernon F. Cormier
Department of Geology & Geophysics
U-45, Room 207
The University of Conneticut
Storrs, Connecticut 06268

Dr. Zoltan A. Der
ENSCO, Inc.
5400 Port Royal Road
Springfield, VA 22151-2388

Professor John Ferguson
Center for Lithospheric Studies
The University of Texas at Dallas
P.O. Box 830688
Richardson, TX 75083-0688

Professor Stanley Flatte'
Applied Sciences Building
University of California, Santa Cruz
Santa Cruz, CA 95064

Professor Steven Grand
Department of Geology
245 Natural History Building
1301 West Green Street
Urbana, IL 61801

Professor Roy Greenfield
Geosciences Department
403 Deike Building
The Pennsylvania State University
University Park, PA 16802

Professor David G. Harkrider
Seismological Laboratory
Div of Geological & Planetary Sciences
California Institute of Technology
Pasadena, CA 91125

Professor Donald V. Helmberger
Seismological Laboratory
Div of Geological & Planetary Sciences
California Institute of Technology
Pasadena, CA 91125

Professor Eugene Herrin
Institute for the Study of Earth
 & Man/Geophysical Laboratory
Southern Methodist University
Dallas, TX 75275

Professor Robert B. Herrmann
Department of Earth & Atmospheric
     Sciences
Saint Louis University
Saint Louis, MO 63156

Professor Lane R. Johnson
Seismographic Station
University of California
Berkeley, CA 94720

Professor Thomas H. Jordan
Department of Earth, Atmospheric
 and Planetary Sciences
Mass Institute of Technology
Cambridge, MA 02139

Dr. Alan Kafka
Department of Geology &
  Geophysics
Boston College
Chestnut Hill, MA 02167

Professor Leon Knopoff
University of California
Institute of Geophysics
 & Planetary Physics
Los Angeles, CA 90024

Professor Charles A. Langston
Geosciences Department
403 Deike Building
The Pennsylvania State University
University Park, PA 16802

Professor Thorne Lay
Department of Geological Sciences
1006 C.C. Little Building
University of Michigan
Ann Harbor, MI 48109--1063

Dr. Randolph Martin III
New England Research, Inc.
P.O. Box 857
Norwich, VT 05055

Dr. Gary McCartor
Mission Research Corp.
735 State Street
P.O. Drawer 719
Santa Barbara, CA 93102   (2 copies)

Professor Thomas V. McEvilly
Seismographic Station
University of California
Berkeley, CA 94720

Dr. Keith L. McLaughlin
S-CUBED,
A Division of Maxwell Laboratory
P.O. Box 1620
La Jolla, CA 92038-1620

Professor William Menke
Lamont-Doherty Geological Observatory
 of Columbia University
Palisades, NY 10964

Professor Brian J. Mitchell
Department of Earth & Atmospheric
     Sciences
Saint Louis University
Saint Louis, MO 63156

Mr. Jack Murphy
S-CUBED
A Division of Maxwell Laboratory
11800 Sunrise Valley Drive
Suite 1212
Reston, VA 22091 (2 copies)

Professor J. A. Orcutt
Institute of Geophysics and Planetary
  Physics, A-205
Scripps Institute of Oceanography
Univ. of California, San Diego
La Jolla, CA 92093

Professor Keith Priestley
University of Nevada
Mackay School of Mines
Reno, NV 89557

Wilmer Rivers
Teledyne Geotech
314 Montgomery Street
Alexandria, VA 22314

Professor Charles G. Sammis
Center for Earth Sciences
University of Southern California
University Park
Los Angeles, CA 90089-0741

Dr. Jeffrey L. Stevens
S-CUBED,
A Division of Maxwell Laboratory
P.O. Box 1620
La Jolla, CA 92038-1620

Professor Brian Stump
Institute for the Study of Earth & Man
Geophysical Laboratory
Southern Methodist University
Dallas, TX 75275

Professor Ta-liang Teng
Center for Earth Sciences
University of Southern California
University Park
Los Angeles, CA 90089-0741

Professor M. Nafi Toksoz
Earth Resources Lab
Dept of Earth, Atmospheric and
    Planetary Sciences
Massachusetts Institute of Technology
42 Carleton Street
Cambridge, MA 02142

Professor Terry C. Wallace
Department of Geosciences
Building #11
University of Arizona
Tucson, AZ 85721

Weidlinger Associates
ATTN: Dr. Gregory Wojcik
620 Hansen Way, Suite 100
Palo Alto, CA 94304

Professor Francis T. Wu
Department of Geological Sciences
State University of new York
 At Binghamton
Vestal, NY 13901

OTHERS (United States)

Dr. Monem Abdel-Gawad
Rockwell Internat'l Science Center
1049 Camino Dos Rios
Thousand Oaks, CA 91360

Professor Shelton S. Alexander
Geosciences Department
403 Deike Building
The Pennsylvania State University
University Park, PA 16802

Dr. Ralph Archuleta
Department of Geological
  Sciences
Univ. of California at
  Santa Barbara
Santa Barbara, CA

Dr. Muawia Barazangi
Geological Sciences
Cornell University
Ithaca, NY 14853

J. Barker
Department of Geological Sciences
State University of New York
 at Binghamton
Vestal, NY   13901

Mr. William J. Best
907 Westwood Drive
Vienna, VA 22180

Dr. N. Biswas
Geophysical Institute
University of Alaska
Fairbanks, AK 99701

Dr. G. A. Bollinger
Department of Geological Sciences
Virginia Polytechnical Institute
21044 Derring Hall
Blacksburg, VA   24061

Dr. James Bulau
Rockwell Int'l Science Center
1049 Camino Dos Rios
P.O. Box 1085
Thousand Oaks, CA 91360

Mr. Roy Burger
1221 Serry Rd.
Schenectady, NY   12309

Dr. Robert Burridge
Schlumberger-Doll Resch Ctr.
Old Quarry Road
Ridgefield, CT 06877

Science Horizons, Inc.
ATTN: Dr. Theodore Cherry
710 Encinitas Blvd., Suite 101
Encinitas, CA 92024 (2 copies)

Professor Jon F. Claerbout
Professor Amos Nur
Dept. of Geophysics
Stanford University
Stanford, CA 94305 (2 copies)

Dr. Anton W. Dainty
AFGL/LWH
Hanscom AFB, MA 01731

Professor Adam Dziewonski
Hoffman Laboratory
Harvard University
20 Oxford St.
Cambridge, MA 02138

Professor John Ebel
Dept of Geology & Geophysics
Boston College
Chestnut Hill, MA 02167

Dr. Alexander Florence
SRI International
333 Ravenswood Avenue
Menlo Park, CA 94025-3493

Dr. Donald Forsyth
Dept. of Geological Sciences
Brown University
Providence, RI 02912

Dr. Anthony Gangi
Texas A&M University
Department of Geophysics
College Station, TX 77843

Dr. Freeman Gilbert
Institute of Geophysics &
 Planetary Physics
Univ. of California, San Diego
P.O. Box 109
La Jolla, CA 92037

Mr. Edward Giller
Pacific Seirra Research Corp.
1401 Wilson Boulevard
Arlington, VA 22209

Dr. Jeffrey W. Given
Sierra Geophysics
11255 Kirkland Way
Kirkland, WA 98033

Dr. Henry L. Gray
Associate Dean of Dedman College
Department of Statistical Sciences
Southern Methodist University
Dallas, TX 75275

Rong Song Jih
Teledyne Geotech
314 Montgomery Street
Alexandria, Virginia 22314

Professor F.K. Lamb
University of Illinois at
  Urbana-Champaign
Department of Physics
1110 West Green Street
Urbana, IL 61801

Dr. Arthur Lerner-Lam
Lamont-Doherty Geological Observatory
 of Columbia University
Palisades, NY 10964

Dr. L. Timothy Long
School of Geophysical Sciences
Georgia Institute of Technology
Atlanta, GA 30332

Dr. Peter Malin
University of California at Santa Barbara
Institute for Central Studies
Santa Barbara, CA 93106

Dr. George R. Mellman
Sierra Geophysics
11255 Kirkland Way
Kirkland, WA 98033

Dr. Bernard Minster
Institute of Geophysics and Planetary
  Physics, A-205
Scripps Institute of Oceanography
Univ. of California, San Diego
La Jolla, CA 92093

Dr. Geza Nagy
SRI International
333 Ravenswood Avenue
Menlo Park, CA 94025-3493

Dr. Jack Oliver
Department of Geology
Cornell University
Ithaca, NY 14850

Dr. Robert Phinney/Dr. F.A. Dahlen
Dept of Geological
  Geophysical Sci. University
Princeton University
Princeton, NJ 08540 (2 copies)

RADIX Systems, Inc.
Attn: Dr. Jay Pulli
2 Taft Court, Suite 203
Rockville, Maryland 20850

Professor Paul G. Richards
Lamont-Doherty Geological
 Observatory of Columbia Univ.
Palisades, NY 10964

Dr. Norton Rimer
S-CUBED
A Division of Maxwell Laboratory
P.O. 1620
La Jolla, CA 92038-1620

Professor Larry J. Ruff
Department of Geological Sciences
1006 C.C. Little Building
University of Michigan
Ann Arbor, MI 48109-1063

Dr. Alan S. Ryall, Jr.
Center of Seismic Studies
1300 North 17th Street
Suite 1450
Arlington, VA 22209-2308   (4 copies)

Dr. Richard Sailor
TASC Inc.
55 Walkers Brook Drive
Reading, MA 01867

Dr. David G. Simpson
Lamont-Doherty Geological Observ.
  of Columbia University
Palisades, NY 10964

Dr. Bob Smith
Department of Geophysics
University of Utah
1400 East 2nd South
Salt Lake City, UT 84112

Dr. S. W. Smith
Geophysics Program
University of Washington
Seattle, WA 98195

Rondout Associates
ATTN: Dr. George Sutton,
Dr. Jerry Carter, Dr. Paul Pomeroy
P.O. Box 224
Stone Ridge, NY 12484 (4 copies)

Dr. L. Sykes
Lamont Doherty Geological Observ.
Columbia University
Palisades, NY 10964

Dr. Pradeep Talwani
Department of Geological Sciences
University of South Carolina
Columbia, SC 29208

Dr. R. B. Tittmann
Rockwell International Science Center
1049 Camino Dos Rios
P.O. Box 1085
Thousand Oaks, CA 91360

Professor John H. Woodhouse
Hoffman Laboratory
Harvard University
20 Oxford St.
Cambridge, MA 02138

Dr. Gregory B. Young
ENSCO, Inc.
5400 Port Royal Road
Springfield, VA 22151-2388

Dr. Peter Basham
Earth Physics Branch
Geological Survey of Canada
1 Observatory Crescent
Ottawa, Ontario
CANADA K1A OY3

Dr. Eduard Berg
Institute of Geophysics
University of Hawaii
Honolulu, HI 96822

Dr. Michel Bouchon - Universite
  Scientifique et Medicale de Grenob
Lab de Geophysique - Interne et
  Tectonophysique - I.R.I.G.M-B.P.
38402 St. Martin D'Heres
Cedex FRANCE

Dr. Hilmar Bungum/NTNF/NORSAR
P.O. Box 51
Norwegian Council of Science,
Industry and Research, NORSAR
N-2007 Kjeller, NORWAY

Dr. Michel Campillo
I.R.I.G.M.-B.P. 68
38402 St. Martin D'Heres
Cedex, FRANCE

Dr. Kin-Yip Chun
Geophysics Division
Physics Department
University of Toronto
Ontario, CANADA M5S 1A7

Dr. Alan Douglas
Ministry of Defense
Blacknest, Brimpton,
 Reading RG7-4RS
UNITED KINGDOM

Dr. Manfred Henger
Fed. Inst. For Geosciences & Nat'l Res.
Postfach 510153
D-3000 Hannover 51
FEDERAL REPUBLIC OF GERMANY

Dr. E. Husebye
NTNF/NORSAR
P.O. Box 51
N-2007 Kjeller, NORWAY

Tormod Kvaerna
NTNF/NORSAR
P.O. Box 51
N-2007 Kjeller, NORWAY

Mr. Peter Marshall, Procurement
 Executive, Ministry of Defense
Blacknest, Brimpton,
 Reading FG7-4RS
UNITED KINGDOM (3 copies)

Dr. Ben Menaheim
Weizman Institute of Science
Rehovot, ISRAEL 951729

Dr. Svein Mykkeltveit
NTNF/NORSAR
P.O. Box 51
N-2007 Kjeller, NORWAY (3 copies)

Dr. Robert North
Geophysics Division
Geological Survey of Canada
1 Observatory crescent
Ottawa, Ontario
CANADA, K1A 0Y3

Dr. Frode Ringdal
NTNF/NORSAR
P.O. Box 51
N-2007 Kjeller, NORWAY

Dr. Jorg Schlittenhardt
Federal Inst. for Geosciences & Nat'l Res.
Postfach 510153
D-3000 Hannover 51
FEDERAL REPUBLIC OF GERMANY

University of Hawaii
Institute of Geophysics
ATTN: Dr. Daniel Walker
Honolulu, HI 96822

FOREIGN CONTRACTORS

Dr. Ramon Cabre, S.J.
c/o Mr. Ralph Buck
Economic Consular
American Embassy
APO Miami, Florida   34032

Professor Peter Harjes
Institute for Geophysik
Rhur University/Bochum
P.O. Box 102148 4630 Bochum 1
FEDERAL REPUBLIC OF GERMANY

Professor Brian L.N. Kennett
Research School of Earth Sciences
Institute of Advanced Studies
G.P.O. Box 4
Canberra 2601
AUSTRALIA

Dr. B. Massinon
Societe Radiomana
27, Rue Claude Bernard
7,005, Paris, FRANCE (2 copies)

Dr. Pierre Mechler
Societe Radiomana
27, Rue Claude Bernard
75005. Paris, FRANCE

Dr. Ralph Alewine III
DARPA/NMRO
1400 Wilson Boulevard
Arlington, VA 22209-2308

Dr. Peter Basham
Geological Survey of Canada
1 Observatory Creseut
Ottowa, Ontario
CANADA K1A 0Y3

Dr. Robert Blandford
DARPA/NMRO
1400 Wilson Boulevard
Arlington, VA 22209-2308

Sandia National Laboratory
ATTN: Dr. H. B. Durham
Albuquerque, NM 87185

Dr. Jack Evernden
USGS-Earthquake Studies
345 Middlefield Road
Menlo Park, CA 94025

U.S. Geological Survey
ATTN: Dr. T. Hanks
Nat'l Earthquake Resch Center
345 Middlefield Road
Menlo Park, CA 94025

Dr. James Hannon
Lawrence Livermore Nat'l Lab.
P.O. Box 808
Livermore, CA 94550

U.S. Arms Control & Disarm. Agency
ATTN: Dick Morrow
Washington, D.C. 20451

Paul Johnson
ESS-4, Mail Stop J979
Los Alamos National Laboratory
Los Alamos, NM 87545

Ms. Ann Kerr
DARPA/NMRO
1400 Wilson Boulevard
Arlington, VA 22209-2308

Dr. Max Koontz
US Dept of Energy/DP 331
Forrestal Building
1000 Independence Ave.
Washington, D.C. 20585

Dr. W. H. K. Lee
USGS
Office of Earthquakes, Volcanoes,
 & Engineering
Branch of Seismology
345 Middlefield Rd
Menlo Park, CA 94025

Dr. William Leith
USGS
Mail Stop 928
Reston, VA 22092

Dr. Robert Masse'
Box 25046, Mail Stop 967
Denver Federal Center
Denver, Colorado 80225

R. Morrow
ACDA/VI
Room 5741
320 21st Street N.W
Washington, D.C. 20451

Dr. Keith K. Nakanishi
Lawrence Livermore National Laboratory
P.O. Box 808, L-205
Livermore, CA 94550 (2 copies)

Dr. Carl Newton
Los Alamos National Lab.
P.O. Box 1663
Mail Stop C335, Group E553
Los Alamos, NM 87545

Dr. Kenneth H. Olsen
Los Alamos Scientific Lab.
Post Office Box 1663
Los Alamos, NM 87545

Howard J. Patton
Lawrence Livermore National Laboratory
P.O. Box 808, L-205
Livermore, CA 94550

AFOSR/NP
ATTN: Colonel Jerry J. Perrizo
Bldg 410
Bolling AFB, Wash D.C. 20332-6448

HQ AFTAC/TT
Attn: Dr. Frank F. Pilotte
Patrick AFB, Florida 32925-6001

Mr. Jack Rachlin
USGS - Geology, Rm 3 C136
Mail Stop 928 National Center
Reston, VA 22092

Robert Reinke
AFWL/NTESG
Kirtland AFB, NM 87117-6008

HQ AFTAC/TGR
Attn Dr. George H. Rothe
Patrick AFB, Florida 32925-6001

Donald L. Springer
Lawrence Livermore National Laboratory
P.O. Box 808, L-205
Livermore, CA 94550

Dr. Lawrence Turnbull
OSWR/NED
Central Intelligence Agency
CIA, Room 5G48
Washington, D.C. 20505

Dr. Thomas Weaver
Los Alamos Scientific Laboratory
Los Almos, NM 97544

AFGL/SULL
Research Library
Hanscom AFB, MA 01731-5000 (2 copies)

Secretary of the Air Force (SAFRD)
Washington, DC 20330
Office of the Secretary Defense
DDR & E
Washington, DC 20330

HQ DNA
ATTN: Technical Library
Washington, DC 20305

Director, Technical Information
DARPA
1400 Wilson Blvd.
Arlington, VA 22209

AFGL/XO
Hanscom AFB, MA 01731-5000

AFGL/LW
Hanscom AFB, MA 01731-5000

DARPA/PM
1400 Wilson Boulevard
Arlington, VA 22209

Defense Technical
 Information Center
Cameron Station
Alexandria, VA 22314
(12 copies)

Defense Intelligence Agency
Directorate for Scientific &
  Technical Intelligence
Washington, D.C. 20301

Defense Nuclear Agency/SPSS
ATTN: Dr. Michael Shore
6801 Telegraph Road
Alexandria, VA 22310

AFTAC/CA (STINFO)
Patrick AFB, FL 32925-6001